University of Nottingham

UK | CHINA | MALAYSIA

MRI Changes in Visceral Fat in Crohn's Disease

By

Iyad A. Naim

Thesis submitted to
The University of Nottingham
for the degree of
Doctor of Philosophy

January 2023

Abstract

Crohn's Disease (CD) is a chronic inflammatory disease of the gastrointestinal tract affecting 115,000 people in the UK alone. As a chronic illness, CD management requires a stepwise escalation of treatment measures tethered with constant monitoring of the disease activity levels and progression. Hence, non-invasive disease activity assessment methods form an essential part of the treatment process. Endoscopy is considered to be the traditional method for CD diagnosis and disease activity assessment which is invasive and may be uncomfortable for patients. As traditional MRI-based disease assessment methods rely on intravenous gadolinium for contrast enhancement, CD patients typically undergo repeated exposure to gadolinium administration which adds cost and carries the risk of nephrogenic systemic fibrosis, allergic reaction, and long-term brain deposition following repeated use. Hence, the development of contrast-free MRI-based disease activity metrics eliminates the risks associated with gadolinium and allows for a more frequent assessment of the disease progression. However, all developed cross-sectional CD activity metrics so far rely on a visual assessment by radiologists which can be subjective and time-consuming.
The aim of this thesis is to examine established radiological hallmarks of CD and employ MRI imaging sequences along with image processing techniques to generate objective and quantitative disease activity measurements.

The first part of this thesis investigates visceral fat hypertrophy also known as fat wrapping which refers to an abnormal growth of the mesenteric fat to partially cover the small or large intestine. While fat wrapping has been established as a characteristic of CD, the complex nature of visceral fat hinders detailed analysis of the effect of fat wrapping. Hence, an automated abdominal fat segmentation algorithm was developed to generate an objective measure of abdominal fat volumes which was used to study the differences in visceral fat revealing significant differences between CD patients and healthy volunteers.

The second part of the thesis examines mesenteric blood flow in CD patients. CD is known to be associated with hypervascularity of the mesentery, including vascular

dilation and wide spacing of the vasa recta. The arteries supply the small bowel branch to a series of intestinal arteries within the mesentery. A second algorithm was developed to automatically trace abdominal vessels on a time-of-flight MRA scans and measure the number of vessels' branching points which also revealed significant differences between CD patients and HVs.

This research has demonstrated the potential for MRI and image processing techniques to provide objective and quantitative measurements of disease activity in CD. The development of automated algorithms for abdominal fat segmentation and vessel tracing allows for a more accurate and efficient assessment of key radiological hallmarks of CD which are often overlooked. These techniques have the potential to improve the management of CD by providing non-invasive and more frequent assessments of disease activity and progression, without the risks associated with traditional contrast-enhanced methods.

Acknowledgements

I would like to express my heartfelt gratitude to my supervisor, Professor Gordon Moran, for his unwavering support, guidance, and encouragement throughout my PhD journey. His invaluable insights, constructive feedback, and patience have been instrumental in shaping my research and my overall development as a researcher. I am deeply grateful for his mentorship and for the opportunity to work with him. I would also like to extend my sincere thanks to Professor Penny Gowland and Dr Caroline Hoad for their mentorship and support. Their guidance, encouragement, and patience have been invaluable to me and have truly demonstrated what it means to be a mentor. Their expertise and willingness to share their knowledge have had a profound impact on my research and my growth as a researcher.

I am grateful to my family for their unconditional support and belief in me. Their encouragement and love have been a constant source of strength and motivation during my PhD journey. I would especially like to thank my parents for always believing in me, no matter what challenges I face.

I would like to thank my wife Yasmine for her love, support, and understanding throughout this journey. Her encouragement and patience have been invaluable, and I am deeply grateful for her presence in my life. She has been my rock and has always been there for me, no matter what challenges arise. I am truly blessed to have such a supportive and loving partner by my side.

I would also like to express my gratitude to the staff and colleagues at the SPMIC for their support and assistance throughout my PhD journey. I am grateful to have had the opportunity to work with such talented and dedicated individuals.

Lastly, I would like to thank the funding bodies the BRC and the Haydn Green Institute for their financial support, which has been crucial in enabling me to pursue my research. Without their support, this journey would not have been possible**.**

Abbreviations

ADC	Apparent Diffusion Coefficient
BRC	Biomedical Research Centre
CD	Crohn's Disease
CDEIS	Crohn's Disease Endoscopic Index of Severity
CDAI	Crohn's Disease Activity Index
CT	Computed Tomography
CRP	C - Reactive Protein
DWI	Diffusion Weighted Imaging
ETL	Echo Train Length
FSE	Fast Spin Echo
FA	Flip Angle
GI	Gastrointestinal
GRE	Gradient Echo
IBD	Inflammatory Bowel Disease
IDEAL	the Iterative Decomposition of Water and Fat With Echo Asymmetry and Least-Squares Estimation
IV	Intravenous
MRA	Magnetic Resonance Angiography
MaRIA	Magnetic Resonance Imaging Index of Activity
MRE	Magnetic Resonance Enterography
MRI	Magnetic Resonance Imaging
MIP	Maximum Intensity Projection
NHS	National Health Service
RF	Radio Frequency
RCE	Relative Contrast Enhancement
SAT	Subcutaneous Adipose Tissue
SPMIC	Sir Peter Mansfield Imaging Centre
SNR	Signal to Noise Ratio
SES-CD	Simplified Endoscopic Activity Score for CD
SE	Spin Echo
TAT	Total Adipose Tissue
TE	Echo Time
TOF	Time Of Flight
TSE	Turbo Spin Echo
TR	Repetition Time
US	Ultrasound
VAT	Visceral Adipose Tissue
WAT	White Adipose Tissue
WSI	Wall Signal Intensity

1 Introduction

Crohn's Disease (CD) is a chronic, relapsing and remitting inflammatory disease affecting the gastrointestinal tract. Recently, the prevalence of CD has been increasing, reaching up to 157 per 100,000 people, which means that there are currently at least 115,000 CD patients in UK alone. Up to a third of CD patients are diagnosed before the age of 21 (NICE, 2019). In Scotland and Lothian, inflammatory bowel disease (IBD) prevalence is 1 in 125 (0.8%) (Jones et al., 2019). As disease activity assessment form a crucial part of CD management, patients require repeated disease progression evaluation. The current endoscopic standard clinical methods for diagnosing and evaluating CD progression are invasive, uncomfortable and unable to assess the small bowel.

Advances in MRI research produced non-invasive disease activity metrics which provided a more accurate measure of disease progression and localization. However, as MRI-based disease activity metrics rely on subjective visual identification of disease characteristics by radiologists and in most cases require the use of a contrast agent. Repeated exposure to such contrast agents can be harmful to patients.

This research thesis investigates radiological characteristics of CD which are often overlooked when formulating a disease activity metric while avoiding the use of contrast agents. These characteristics include visceral fat hypertrophy and mesenteric blood flow. This is made possible with the help of MRI imaging sequences and image processing techniques that allows for subjective and quantitative assessment of disease progression.

1.1 Thesis Overview

Chapter 2 introduces the principles underlying the formation of NMR signal and MRI image acquisition techniques. Fat and water separation techniques explained in this chapter will also be used to analyse abdominal fat in later chapters. The chapter also explains the basic principles of image analysis techniques that are used throughout this thesis.

In Chapter 3, the basic pathophysiological mechanisms of CD are introduced and explained. This chapter also covers the various standard clinical practices and procedures used in the diagnosis and management of CD. Additionally, the chapter discusses the various techniques used to measure disease activity. Finally, the chapter covers the various treatment options available for CD.

Chapter 4 discusses the concept of visceral fat hypertrophy as a characteristic feature of CD. The chapter reviews recent research exploring the potential use of visceral fat hypertrophy as a biomarker for assessing disease activity using MRI. It also explains the development of an abdominal fat segmentation algorithm, which is a tool for automatically measuring and analysing the volumes of abdominal visceral and subcutaneous fat on MRI images.

Chapter 5 describes the application of the abdominal fat segmentation algorithm introduced in chapter 4 by using it to compare the volumes of abdominal fat in CD patients with healthy volunteers. The chapter discusses the results of this analysis and any significant differences that were found between the two groups. It also discusses the potential implications of these findings in terms of understanding the role of visceral fat hypertrophy in the development and progression of CD and its potential as a biomarker for disease activity.

Chapter 6 discusses the increased mesenteric vascularization which is often observed in patients with CD as a characteristic feature of the condition. It highlights the challenges of quantifying this vascularization on cross-sectional imaging and the need for more accurate and reliable methods of assessment. To address this, the chapter introduces a second algorithm that was developed to automatically trace and analyse abdominal vessels on time-of-flight MRA scans. This algorithm allows for the measurement of the number of vessels' branching points, which may be used as a quantitative measure of vascularization in CD patients. The chapter also discusses the development and validation of this algorithm and its potential applications for assessing disease activity in CD.

1.2 Publications and Conference Papers

- **ISMRM 2020 Poster presentation:** MRI Changes in Visceral Fat in Crohn's Disease . (Naim et al., 2020).
- **ISMRM 2022 poster presentation:** Quantification of The Comb Sign in Crohn's Disease Using Time of Flight Magnetic Resonance Angiography (Naim et al., 2022).
- **Journal of Crohn's and Colitis (2022), presentation and abstract publication:** The Arborisation index: An MRI-based measure of mesenteric hyperaemia in Crohn's Disease (Naim et al., 2022).
- **Frontline Gastroenterology (2022**): Imaging in inflammatory bowel disease: current and future perspectives (Shaban et al., 2022).

References

Jones, G. R., Lyons, M., Plevris, N., Jenkinson, P. W., Bisset, C., Burgess, C., Din, S., Fulforth, J., Henderson, P., Ho, G. T., Kirkwood, K., Noble, C., Shand, A. G., Wilson, D. C., Arnott, I. D. R., & Lees, C. W. (2019). IBD prevalence in Lothian, Scotland, derived by capture-recapture methodology. *Gut*, *68*(11), 1953–1960. https://doi.org/10.1136/gutjnl-2019-318936

Crohn's disease: management. NICE guideline NG129. National Institute for Health and Care Excellence. 2019.https://www.nice.org.uk/guidance/ng129 (accessed Mar 2023).

Naim, I., Hoad, C., Gowland, P., & Moran, G. W. (2022). *Quantification of The Comb Sign in Crohn's Disease Using Time of Flight Magnetic Resonance Angiography*. ISMRM. https://archive.ismrm.org/2022/2038.html

Naim, I., Gowland, P., Hoad, C., E Simpson, McGing, J., & Moran, G. W. (2020). *MRI Changes in Visceral Fat in Crohn's Disease*. ISMRM. https://cds.ismrm.org/protected/20MProceedings/PDFfiles/2579.html

Naim, I., Darie, A. M., Hoad, C., Gowland, P., & Moran, G. W. (2022). DOP13 The Arborisation index: An MRI-based measure of mesenteric hyperaemia in Crohn's Disease. *Journal of Crohn's and Colitis*, *16*(Supplement_1), i062–i063. https://doi.org/10.1093/ECCO-JCC/JJAB232.052

Shaban, N., Hoad, C. L., Naim, I., Alshammari, M., Radford, S. J., Clarke, C., Marciani, L., & Moran, G. (2022). Imaging in inflammatory bowel disease: current and future perspectives. *Frontline Gastroenterology*, *13*(e1), e28–e34. https://doi.org/10.1136/FLGASTRO-2022-102117

2 MRI Theory and Image Processing

2.1 Nuclear Magnetic Resonance (NMR)

The concept of Nuclear Magnetic Resonance (NMR) was first proposed in the 1940s by Bloch and Purcell (Purcell et al., 1946) (Bloch, 1946), who demonstrated that the absorption and emission of electromagnetic energy by the nuclei of atoms could be used to study their properties and structure. NMR is based on the principle that any spinning charged particle, such as the nucleus of an atom, creates an electromagnetic field. By placing a sample in a strong magnetic field and applying an electromagnetic pulse with a specific frequency, the nuclei of the atoms in the sample can be stimulated to emit a signal that reveals information about their internal structure and quantum properties.

Over time, NMR was developed and refined into a powerful tool for studying the internal structure and function of biological tissues. The application of NMR to imaging the body led to the development of Magnetic Resonance Imaging (MRI), which is now widely used in medicine and other fields for non-invasive imaging of the body. MRI has become an important tool for diagnosis, research, and treatment, and has contributed significantly to our understanding of the human body and various diseases and conditions.

2.1.1 Nuclear Spin

One of the main fundamental properties of atomic particles is spin. Atomic particles such as protons are said to have an angular momentum known as “nuclear spin” so that they effectively spin on their axes. The angular momentum of a nucleus is given by:

$$J = \frac{hI}{2\pi} \qquad (2.1)$$

where h is Planck’s constant, I is a quantum number that varies by nuclear species, which can only have whole or half-integer values between 0 and 8.

Traditionally, the term $\hbar$ is used to represent $h/2\pi$. Each proton contributes to I with a value of ½. The ^{1}H nucleus is a single proton with I = ½, the lowest possible non-zero value allowed for spin. Since nucleons within a nucleus cancel each other out, only a nucleus with an odd number of nucleons has a spin.

Since protons are positively charged, spin angular momentum causes a nucleus with spin to produce a magnetic moment μ which can be calculated by:

$$\mu = \gamma J \qquad (2.2)$$

where γ is the gyromagnetic ratio, a characteristic constant of the nuclei where each nucleus possesses an intrinsic gyromagnetic ratio that depends on its mass and charge. The unit used for the gyromagnetic ratio is radian per second per Tesla (rad·s^{-1}·T^{-1}) or megahertz per Tesla (MHz/T), which is the unit that will be used in this thesis.
Due to its nuclear structure and high abundance in the human body, hydrogen is typically used to generate most magnetic resonance images. With a value of 42.58 MHz/T, hydrogen is considered to have the highest gyromagnetic ratio of any nucleus. While other nuclei can be used to generate an MR signal, such as phosphorus (γ=17.2 MHz/T), carbon 13 (γ= 10.705 MHz/T) and sodium (γ=11.27 MHz/T), in this thesis, all the work has been done using ^{1}H protons.

2.1.2 Magnetic Moment Under The influence of an External Magnetic Field

When multiple nuclei are present in a sample, the net magnitude and direction of the magnetic moment are obtained by summing up all individual moments. In the absence of an external magnetic field, the nuclear magnetic moment of each nucleus is free to re-orient and fluctuate its spin axis in random directions causing the sample to have zero net magnetic moment.

When the sample is subjected to an external magnetic field (B_o), a torque will be applied to the magnetic moment of each nucleus in the sample causing it to precess around the direction of the applied field. This causes the nucleus to precess in the same way as a gyroscope does in the earth's gravitational field (Figure 2.1).

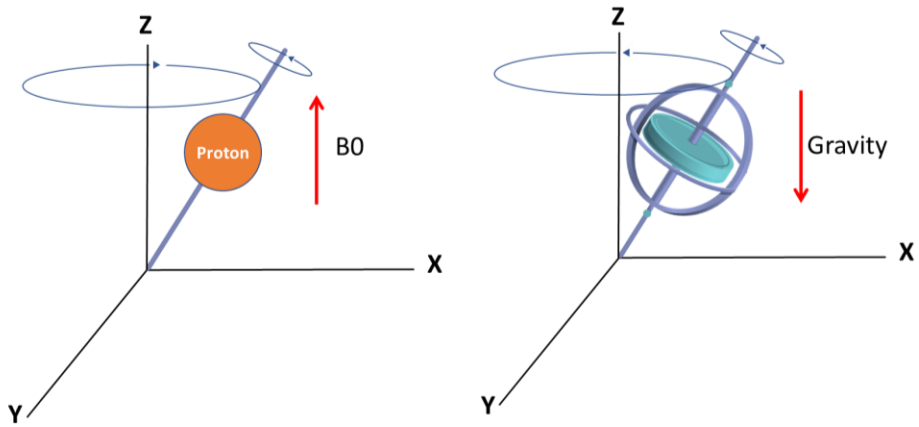

Figure 2.1: The motion of hydrogen nucleus under the effect of an external magnetic field resembles the motion of gyroscope.

The torque applied on the nucleus due to B_o can be calculated as:

$$\tau = \mu B_o \qquad (2.3)$$

However, due to their quantum properties, spin can only precess at defined angles to the magnetic field. The number of allowed orientations at which a nucleus with spin I can precess is $2I$ +1. For hydrogen with spin ½ the number of orientations is therefore equal to 2. These orientations are parallel (precessing around with the field) and anti-parallel (precessing around the negative of the field) which are referred to as energy levels (+½) and (-½) respectively. Spins aligned with the magnetic field tend to have lower energy level than spins aligned against the magnetic field. Hence, number of protons that align with the magnetic field is slightly larger than the number of protons aligned opposite to the magnetic field. In a 1.5 T scanner, the difference between protons at opposite orientations is around 45 protons out of 10 million, and only these 45 protons contribute to the detected NMR signal.

We can calculate energy interaction between the energy levels:

$$E = -\gamma \hbar \, m_I B_o \qquad (2.4)$$

where m_I represents the spin orientation and $B_o$is the strength of the external magnetic field the direction of which defines the z direction.

Therefore, the energy difference between the two energy levels can be calculated to be:

$$\Delta E = \gamma \hbar \, B_o \qquad (2.5)$$

NMR involves a photon of this energy which can cause a spin to flip between these two states. Planck's quantum theory of radiation suggests that the frequency of a photon required to cause a transition is given by:

$$\Delta E = hv \qquad (2.6)$$

where v is the frequency of the particle's precession in Hz, h is Plancks constant= $6.62607004 \times 10^{-34}$ m^2 kg / s.

In NMR, the frequency at which the nucleus absorbs energy is known as the Larmor frequency which is generally expressed in radians $\omega_o = (2\pi v)$.
From equation no. (2.5) we can state that for spin ½ nuclei:

$$\Delta E = \gamma \hbar B_o = \hbar \omega_o \qquad (2.7)$$

Therefore:

$$\omega_0 = \gamma B_o \qquad (2.8)$$

This is known as the Lamour equation which is used to calculate the precession frequency of a nuclei under the application of an external magnetic field B_o. This equation shows that the Larmor frequency of a nuclei is directly proportional to B_o.
The gyromagnetic ratio varies between nuclei and is 42.57e-6 MHz/T for hydrogen nuclei suggesting that an RF magnetic field will cause spins to flip between states for hydrogen.

2.1.3 Net Magnetization

In order to calculate the net magnetic moment of a collection of spins, the difference in the number of spins in each energy level needs to be calculated.
This can be done using the Boltzmann Distribution Law which states:

$$\frac{N_\uparrow}{N_\downarrow} = e^{-\mu B/kT} \approx 1 + \frac{2\mu B_0}{kT} \qquad (2.9)$$

where $N_\uparrow$ and $N_\downarrow$are the population of the spins parallel and anti-parallel to z, T is the temperature in Kelvin and k is Boltzmann constant=1.3805 x $10^{-23}$$JK^{-1}$. Hence, the ratio of $N_\uparrow/N_\downarrow$is affected by changes in temperature, as the temperature increases, the ratio approaches to 1. From eq (2.9), the difference between the two spin states can be calculated as:

$$N_{\uparrow} - N_{\downarrow} = \frac{2\mu B_0}{kT}\ N_{\downarrow} \approx \frac{\mu B_0}{kT} N \qquad (2.10)$$

Hence, the applied magnetic field only effects the magnetic moment of nuclei in the z direction (M_z) and has no effect on the x and y components.

The difference in populations between the two spin states creates a net magnetization, the size of which can be calculated by summing all the magnetic fields generated by each spin.

$$M_o = (N_{\uparrow} - N_{\downarrow})\ \mu_z \qquad (2.11)$$

2.1.4 Excitation

Once the external magnetic field $B_o$has been applied in the z direction, the protons distribute themselves either parallel or anti-parallel to $B_o$to produce a stable value of M_z. As described above, if energy is introduced to the system, in the form of a field oscillating at the Larmor frequency (RF radiation, generally known as the B_1 field), it will cause spins to be flipped between the two possible states, and it will also tend to bring the spins into phase. The result is that the net magnetization is tipped away from the z direction towards the xy plane creating a transverse magnetization. Varying the RF duration and amplitude can determine how far the spins are tipped away from the z direction. The locally induced variation in magnetic field due to RF frequency in known as B_1.

2.1.5 T1 Longitudinal Relaxation

An RF pulse can be designed to induce a 90^o flip of the net magnetization into the *xy* plane is known as 90^o pulse. Once the spins have been excited into the *xy* plane, the protons start to gradually return into their equilibrium distribution and the net magnetization realigns with z. The time it takes for a spin to return to its stable state can be used to measure physical properties in biological tissues (Figure 2.2). Bloch described this process as a simple exponential function using *T1* as a first order time constant (Bloch, 1946).

$$M_z\ = M_0\ (1 - e^{-t/T1}) \qquad (2.13)$$

Hence, *T1* can be thought of as the time it takes for the M_z to reach around 63% of its maximum value (M_0). The spins system returns to its stable state by interacting with its surroundings. Hence, molecular motion and the level of molecular interaction can affect *T1* times for a sample. In terms of net magnetization, before the application of the RF pulse, M_z= M_0, M_{xy}=0. Once a 90° RF pulse has been applied, M_z=0, M_{xy}= M_0.

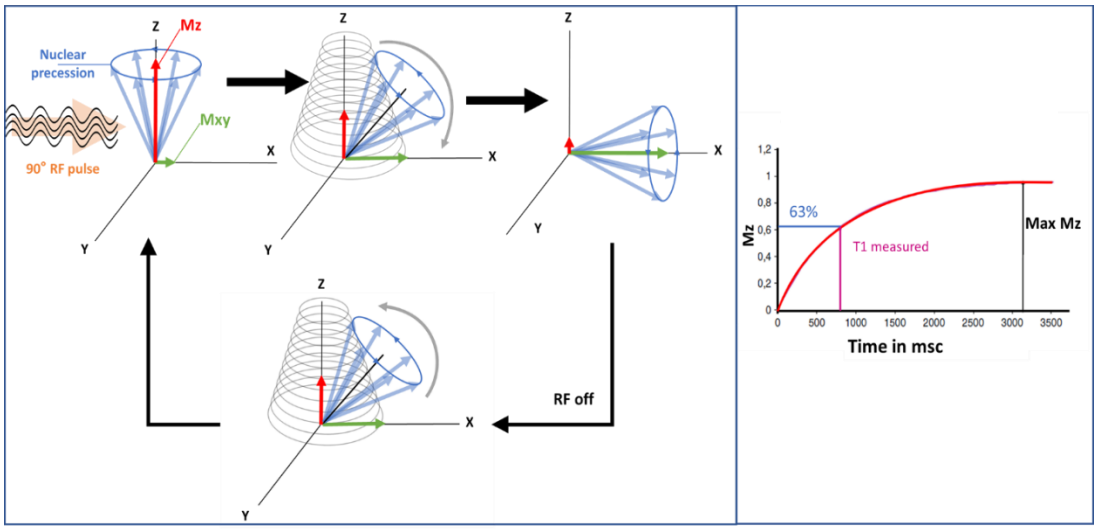

Figure 2.2: Evolution of the magnetization vector upon the application of 90° RF pulse is applied (left) and the resulting longitudinal magnetization plot (right).

2.1.6 T2 Transverse Relaxation

As mentioned previously, net magnetisation in a sample is measured as the sum of all magnetic moments generated by nuclear precession. When the spins are excited, they are brought into phase which creates transverse magnetization. This coherence is lost as the spins flip back along the *z* direction but also because of slight variations in the rate of precession due to molecular interactions. These processes cause a decrease in the net magnetisation in the *xy* plane. This is known as dephasing, where differences between spins rotation speeds cause them to be out of phase, resulting in a gradual reduction in the net transverse magnetisation Figure 2.3. Bloch also described the resulting change in transverse magnetization as an exponential decay using *T2* as a first order time constant.

$$M_{xy} = M_0\, e^{-t/T2} \qquad (2.14)$$

Hence, *T2* can be defined as the time required for the M_{xy} to drop to approximately 37% of its initial value.

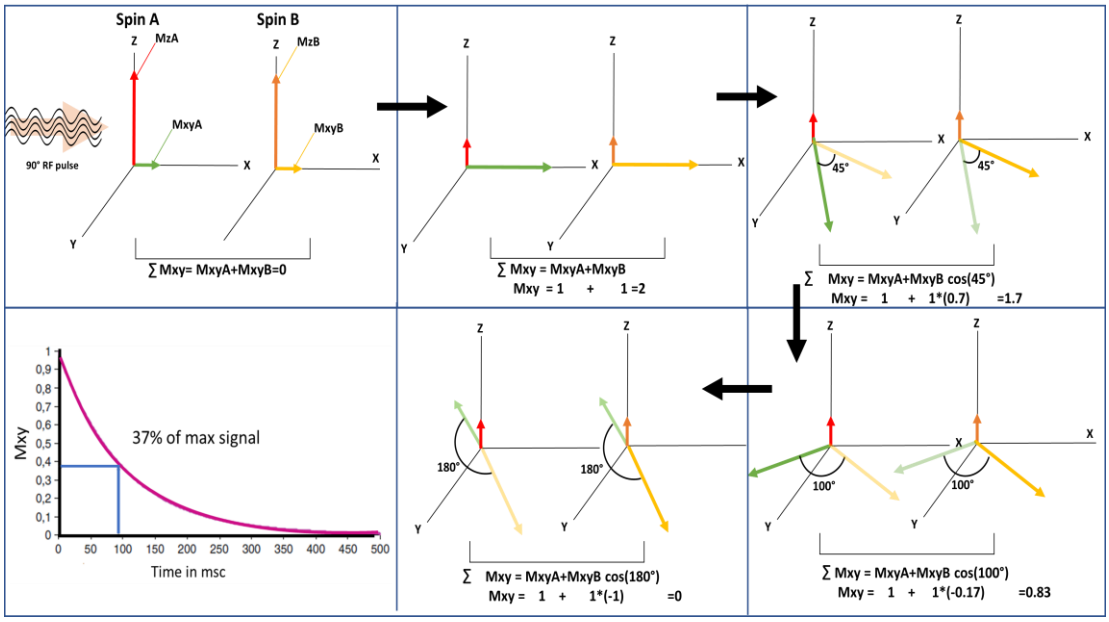

Figure 2.3: The dephasing of the transverse magnetization following the 90° excitation RF pulse and the corresponding transverse magnetization decay plot.

2.1.7 Free Induction Decay

The net transverse magnetization generated by the spins' coherent precession can be modelled as a rotating bar magnet, which would induce an oscillating voltage generated by the motion can be detected as an oscillating signal in a neighbouring coil as shown in Figure 2.4. In MRI, the receiver coil needs to be tuned to the Larmor frequency to detect the generated FID signal. The effects of *T1* and *T2* decay cause the generated signal to dissipate over time. Another factor that contributes to the rapid drop in the measured signal is $B_o$inhomogeneity. The slight variations across B_o causes spins to precess at different frequencies which contributes to the transverse signal dephasing. The combination of *T2* and signal decay due to B_0 inhomogeneity is known as *T2**, which is given by:

$$\frac{1}{T2^*} = \frac{1}{T2} + \frac{1}{T2_i} \qquad (2.15)$$

where $T2_i$ is the time constant for signal decay caused by B_o inhomogeneity.

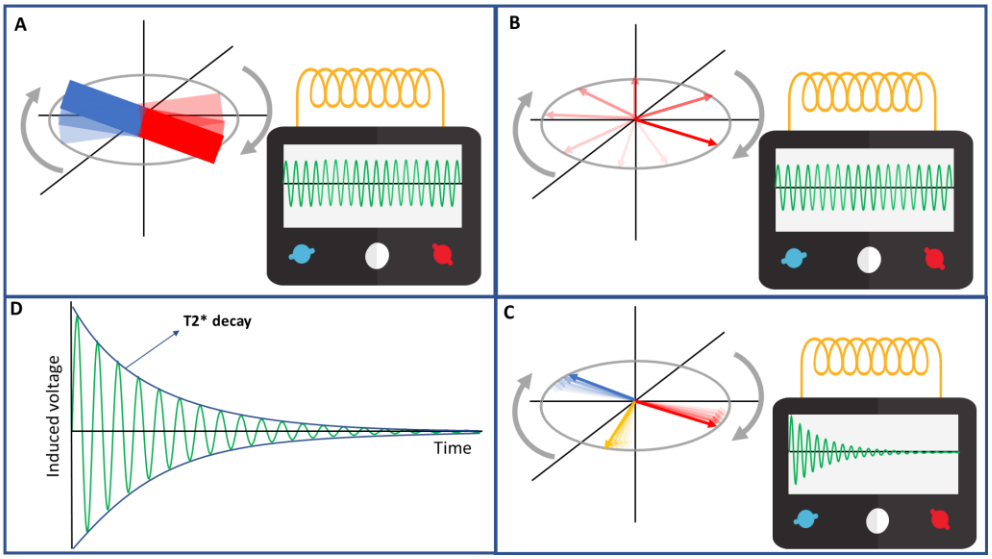

Figure 2.4: The motion of a bar magnet near a coil can generate a detectible signal (A) is similar to the motion of the net magnetization in the transverse plane (B). Magnetization dephasing (C) causing the signal decay (D).

To obtain an accurate assessment of *T1* and *T2*, further flip angle manipulations using RF pulses can be used. A 180° RF pulse followed by another 90° pulse is used to measure *T1*. This pulse sequence is known as inversion recovery pulse sequence. The 180° pulse reorients the spins to the *-z* axis. After waiting a specified amount of time known as TI, another 90° pulse is applied to flip the spins into the transverse plane creating a detectable signal as the spins phase is restored (Figure 2.5).

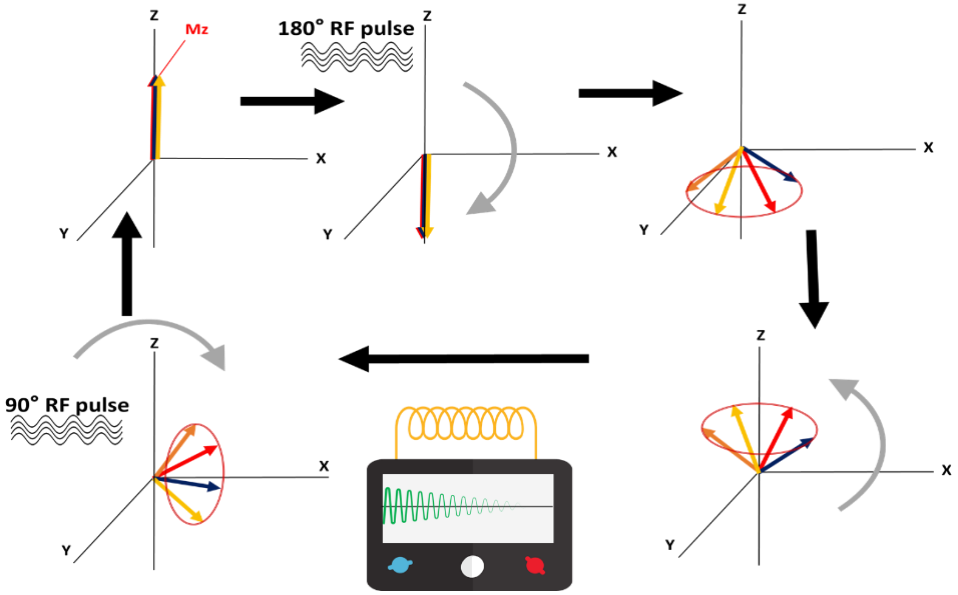

Figure 2.5: The magnetization evolution upon the application of inversion recovery method.

In order to measure *T2* without the effects of B_o inhomogeneity, a 90° pulse followed by 180° pulse is used. This pulse sequence is known as a spin-echo sequence (Hahn, 1950). The 180° pulse flips the spins in the *xy* plane so that the frequency difference between each spin that caused them dephase, now reverse its effect causing the spins to go back in phase generating a signal known as echo. After that, the spins continue to move causing further dephasing in the opposite direction (Figure 2.6). The time between the 90° pulse and peak of the echo is known as the echo time (TE). The time between the 90° pulse and 180° pulse equals TE/2. Since the 180° pulse reverses the dephasing of the spins into the opposite direction, the time between the 180° pulse and the is also TE/2.

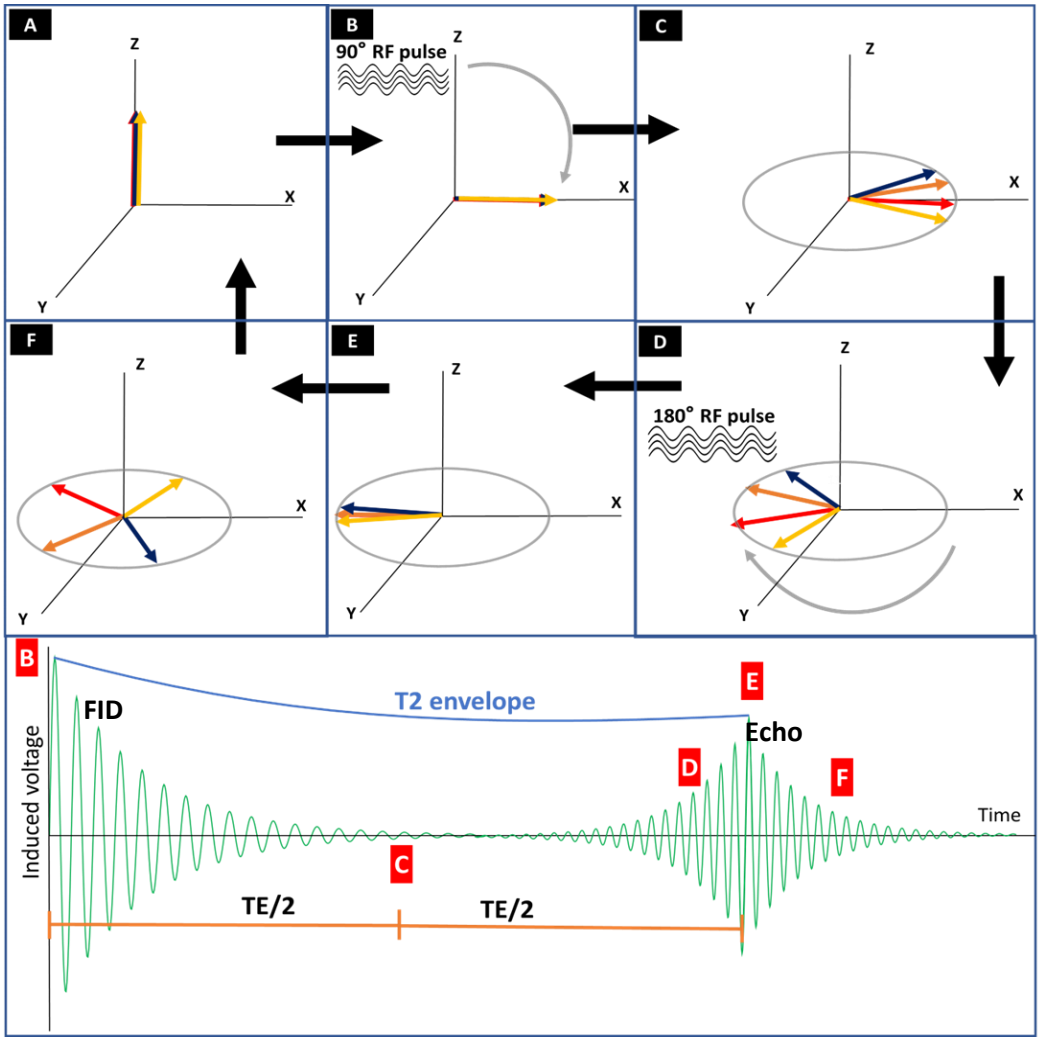

Figure 2.6: The steps of applying a spin echo sequence on the direction of net magnetization showing the application of a 90° pulse (A), the initial tipping of the magnetization into the xy plane starting the magnetization dephasing (B), the application of the 180° pulse (C) which causes the refocusing of magnetization (D, E). The bottom Figure shows the corresponding produced signal.

2.1.8 Chemical Shift

Ideally, all nuclei under an external magnetic field experience the same magnetic field strength. However, field inhomogeneity and nuclear interactions cause slight field variations. The magnetic field experienced by each nucleus is known as B_{local}. So far, we've considered the effects of nearby nuclear motion and interactions. However, electrons are also charged particles and they affect the local magnetic fields B_{local}. Since the Larmor frequency is dependent on B_{local}, molecular structure of the hydrogen atom can also affect the nuclear spin frequency. The hydrogen protons of a fat molecule are located within long-chain triglycerides and surrounded by electrons from neighboring atoms. These electrons apply a partial shielding effect on the protons preventing them from experiencing the full effect on the external magnetic field. In a water molecule however, hydrogen protons are less shielded as the electronegative oxygen atoms pull the electrons away from the hydrogen nucleus. The difference in shielding by electrons corresponds to a frequency difference between fat and water molecules of 215 Hz at 1.5T and 430 Hz at 3T.

2.2 Magnetic Resonance Imaging (MRI)

As previously mentioned, the time it takes for M_z to return to its maximum value (M_0) is depicted by *T1*. Compared to tissues with longer *T1*, those with a shorter *T1* recover faster resulting to a higher M_z values at the time of the acquisition leading to a brighter region on the MRI scan. Alternatively, *T2* reflects the time it takes for the net magnetization to decay in the transverse plane. Therefore, on an MRI image, tissues with short *T2* values appear darker than those with longer *T2*.

To utilize the formation of the NMR signal for medical imaging, a method for locating the source of the signal is needed. This requires manipulating the FID signal to have characteristics regarding the location of its origin. Similar to how a radio signal is used in communication, an NMR FID signal can be modulated to carry locational data. This process is known as spatial encoding. A signal can be modulated to carry information

by changing either its amplitude, frequency, or phase. However, since we are primarily measuring the signal amplitude, any imposed modulations could lead to false data. Hence, the signal's location is generally encoded using frequency and phase modulation.

2.2.1 Slice Selection and Spatial Encoding

As previously mentioned, since each proton is precessing at the Larmor frequency, the FID signal oscillates at the Larmor frequency. Hence, encoding the FID signal with the location of each spin entails changing the rate of precession. From eq (2.8) we know that the rate of precession is proportional to B_o. Therefore, applying an additional linearly varying magnetic field will result in different nuclear precessions for the spins along the magnetic field gradient B_o as shown in Figure 2.7.

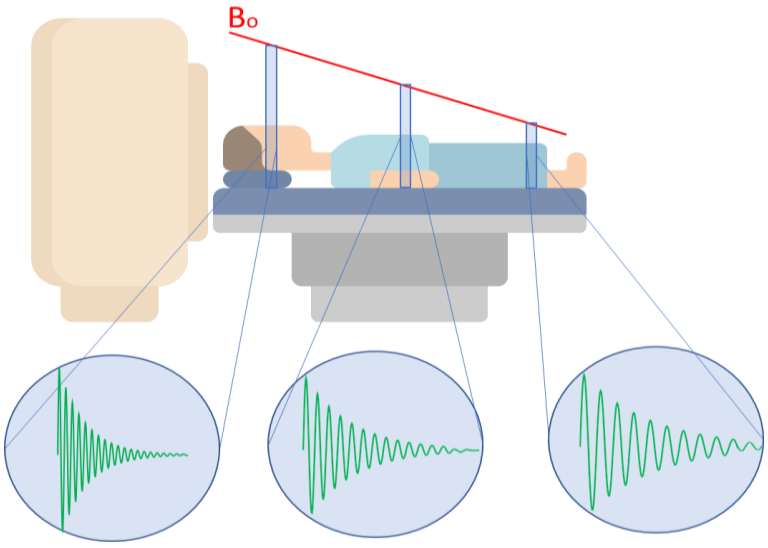

Figure 2.7: The application of a magnetic field gradient causes the spins to precess with different frequencies based on their location along the gradient.

Since the frequency of the RF pulses used for excitation need be at Larmor frequency of the affected spins, applying $B_o$as a gradient, allows the RF pulses to be used to target a specific region in the body while ignoring all other spins outside that region. In this case the B_o gradient is known as slice selection gradient (Gs).

2.2.2 The Design of RF Pulses

The structure of the RF radiation plays a vital role in the generation of MRI images. In its simplest form, B_1 is a sine wave at the required frequency to cause excitation. As the B_o gradient effects the spins across a finite slice, the pulse must contain all the frequencies required to excite the spins in the slice as shown in Figure 2.8.

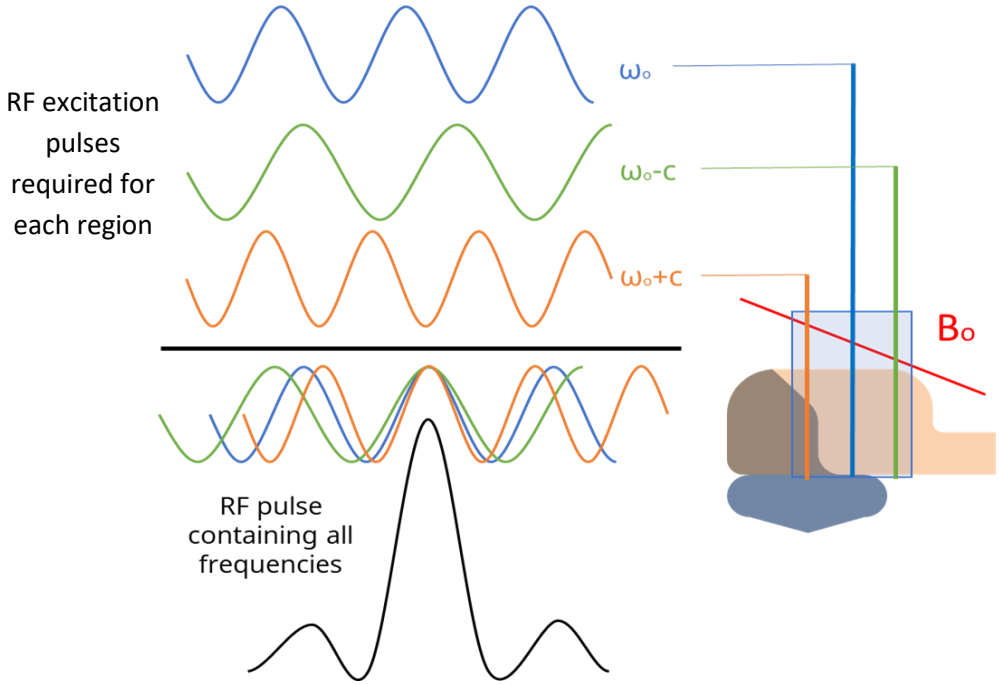

Figure 2.8: The individual RF pulse frequencies required to excite a single slice under the influence of the slice selection gradient.

Therefore, the slice thickness can vary based on the number of frequencies included in the RF pulse. A larger number of frequencies in each RF pulse will result in exciting a thicker slice. Using Fourier transform, the spectrum of frequencies included in each RF excitation pulse can be defined (Figure 2.9).

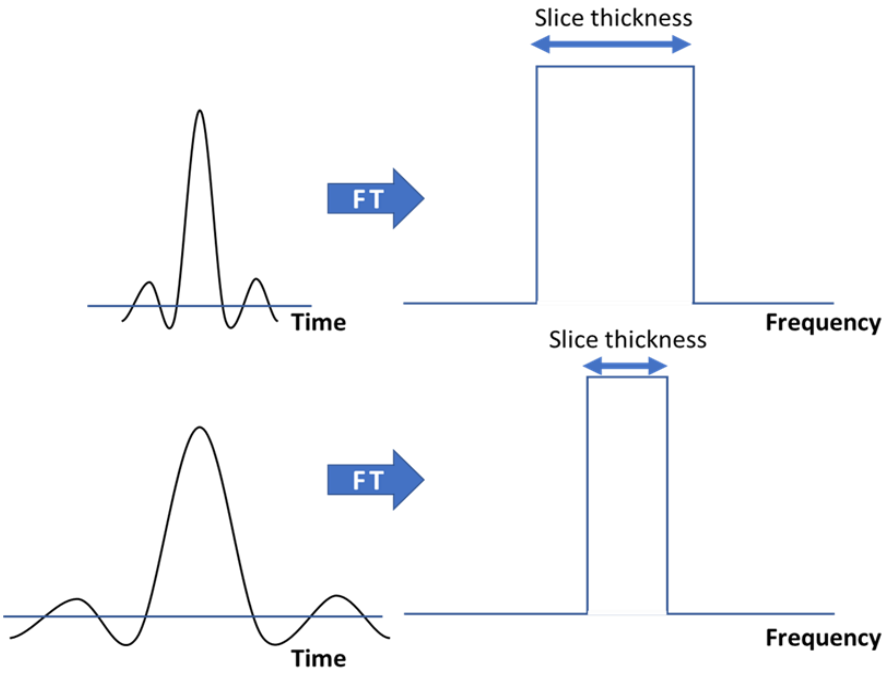

Figure 2.9: Changing slice thickness by using an excitation pulse that includes a larger number of frequencies.

Another method for controlling the slice thickness is changing the slope of B_0. Using the same RF pulse, a larger B_0 gradient will result in a smaller slice thickness as shown in Figure 2.10.

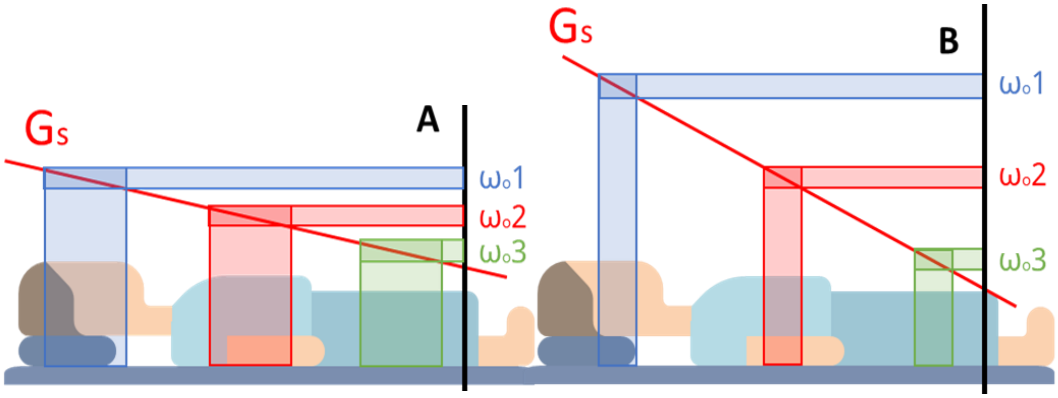

Figure 2.10: The effect of application of steeper frequency encoding gradient on the slice thickness.

2.2.3 Frequency Encoding

Once a slice has been selected, Gs is switched off and a second magnetic field gradient known as frequency encoding gradient (Gf) is used to encode the spins along a perpendicular axis to Gs (Figure 2.11).

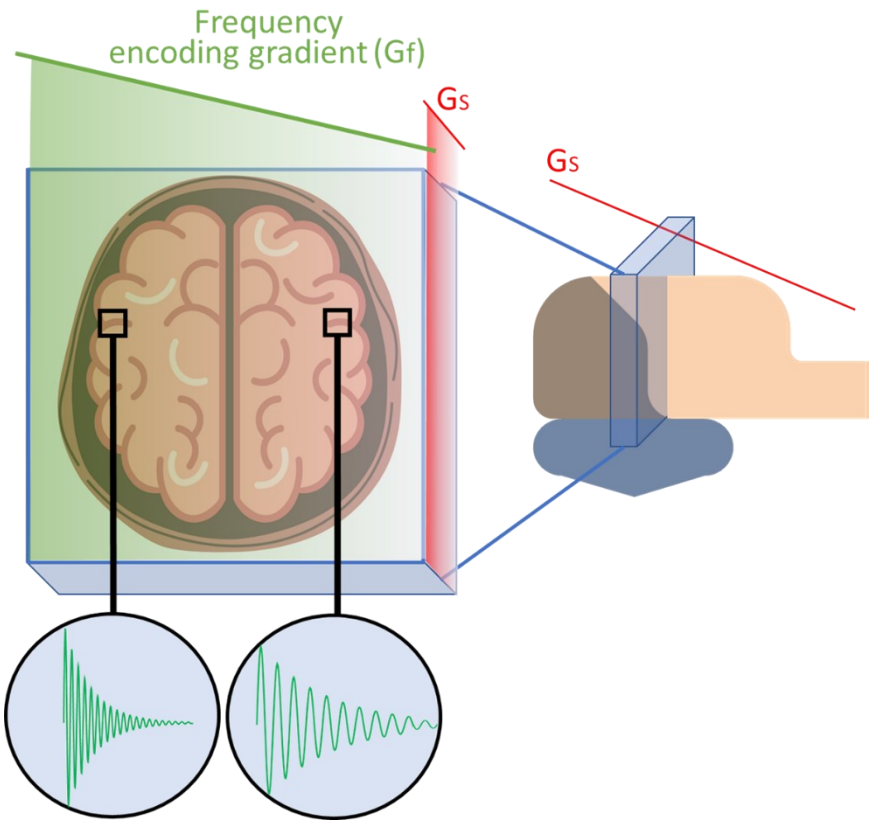

Figure 2.11: The effect of frequency encoding gradient in changing the spins frequency based on their location along the x-axis.

Similar to Gs, the precession frequency of the spins will change due to Gf. Unlike Gs however, the frequency change induced by Gf is used to differentiate the source of the induced signal along the Gf gradient. Signal received with high frequency can be traced back to the higher gradient side of Gf and low frequency signal is identified as coming from the lower side of Gf. Since the generated signal is read out (acquired) whilst a frequency encoding gradient is applied means this is also known as the read gradient. Using the Gf gradient, the received signal can be used to identify the source of each signal using the gradually decreasing frequency. By taking the Fourier transform of the received signal, individual frequency components can reveal the general outline of the image from that direction as shown in Figure 2.12.

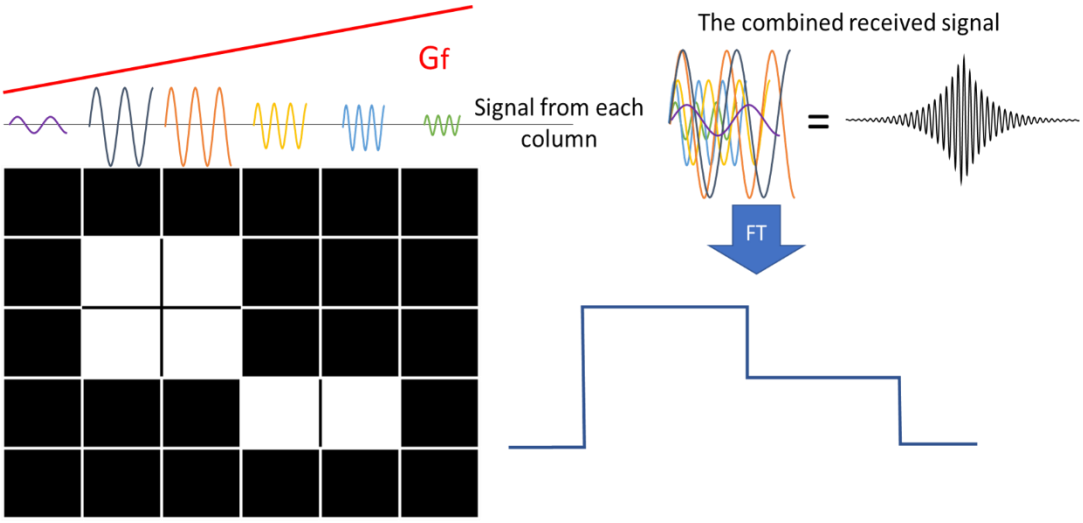

Figure 2.12: A simplified view of a 5X6 imaging target (left) and the corresponding generated signal (right). Under the effect of the frequency encoding gradient (Gf), the Fourier transform of the signal can generate a 1D outline of the image.

2.2.4 Phase Encoding Gradient

So far, the received signal contains spin density information in the form of signal amplitude, and their positional information alone the Gf gradient in form of frequency change. In order to generate depth information from the received signal, a third gradient along the y-axis is required. For this purpose, the signal's phase can be used as a second layer of encoding. The phase encoding gradient (Gp) works similar to the frequency encoding gradient as by changing magnetic field along the y-axis, the spin rotational speed changes with the newly applied field gradient. Once that gradient has been switched off, the spins will go back to rotate at their original frequency however, the temporary exposure to the y-axis gradient effected their phase of rotation. Gp is applied multiple times with gradients gradually changing from negative to positive. As shown in Figure 2.13, the phase gradient is applied effecting the spins' phase, switched off, and the Gf gradient is switched on, and the signal is acquired. This process is repeated multiple times with increasing Gp strength with each acquisition. By taking a second Fourier transform, the resulting signal will contain spin density in form of signal amplitude, and positional information along both x and y axis in the form of frequency and phase shift.

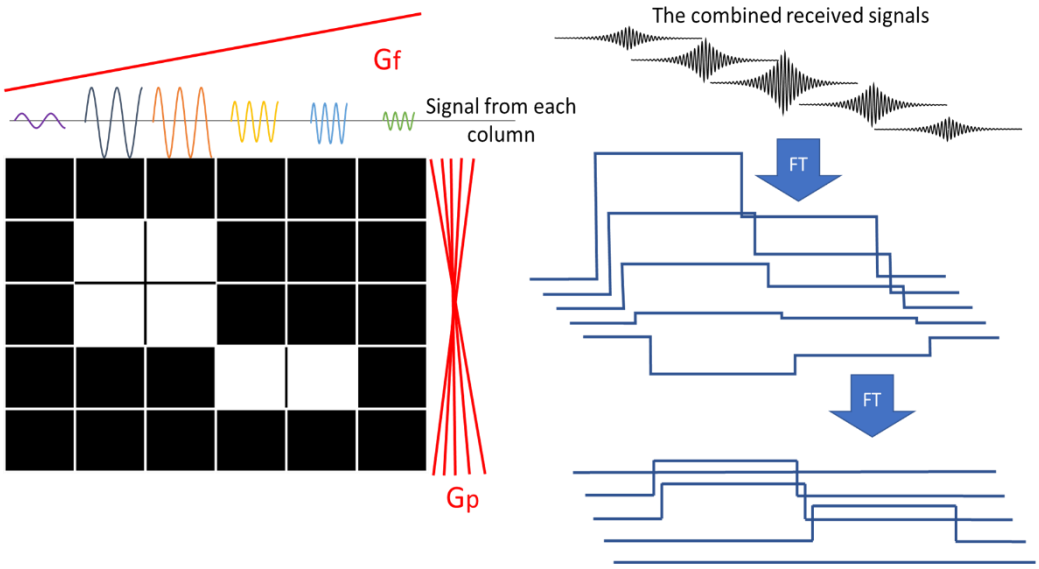

Figure 2.13: Multiple signals generated from the 5X6 imaging target with each signal acquired under the influence of a different phase encoding gradient (Gp).

2.2.5 k-space

To simplify the processing steps required to produce an MR image, the sampled echo signal points are stored in a 2D grid known as k-space. The spins' positional information is recorded in the form frequency and phase shift. Therefore, the k-space is used to generate the image using 2D Fourier transform. The number of rows in the k-space corresponds to the number signal samples that were taken from each echo and the number of columns corresponds to the number of phase encoding gradients. As the signal in the middle of k-space experience the least amount of phase and frequency encoding gradients, it contains the highest signal amplitudes which represents the general image contrast and shape. The signals sampled on the edges of k-space contain the most phase and frequency encoding components which corresponds to the image's lines, edges, and finer details. Filling the k-space entails identifying the location of each data point with respect to its frequency and phase shift. At the beginning of the process, the system is not affected by frequency or phase encoding gradients therefore, the process of filling the k-space starts at the centre. Once the image slice has been chosen using the slice selection gradient and the RF pulse, the application of the first phase

encoding gradient moves the point of data collection to the bottom of k-space (-Ky). After that, the frequency encoding gradient shifts the point of data collection towards the left of the k-space (-Kx). As a result of phase and frequency encoding gradients, a signal is generated which is sampled along the x-axis (Figure 2.14). The process is then repeated with each step of phase encoding gradient moving the point of data collection to the next line in the y-axis. This simple linear process of filling the k-space is known as spin warp imaging. Various procedures of filling k-space have been developed to achieve faster and more efficient data acquisition. Using these various methods entails structuring the gradient sequences to move the data point of collection along the k-space to the chosen positions.

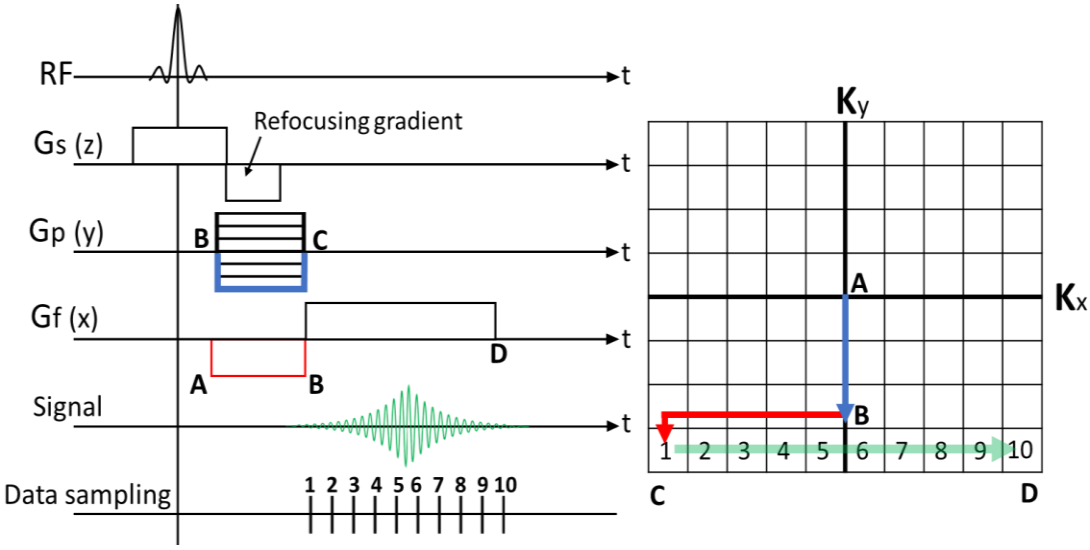

Figure 2.14: The process of filling the K-space showing the pulse sequence on the left and the corresponding k-space trajectory on the right.

2.2.6 MRI Pulse Sequences

One of the advantages of MRI that sets it apart from other medical imaging modalities is its ability to generate a variety of scans each examining certain types of tissue. This is done by changing different parameters such as the order, magnitude and timing of the magnetic gradients and RF pulses. This feature allows for extensive development and rapid testing of new ways to employ the MRI scanner without the need for new parts in most cases. The order, timing and magnitude of the gradients and RF pulses is known as a pulse sequence.

Broadly, pulse sequences can be characterised as spin echo-based and gradient echo-based sequences. Additionally, they can be further characterised based on speed of acquisition into routine, and fast sequences.

2.2.7 Spin Echo (SE) and Fast Spin Echo (FSE) Pulse Sequences

As previously explained, a standard spin echo sequence requires the application of a 90° RF pulse followed by a 180° pulse. The 90° pulse allows for excitation and slice selection while 180° pulse refocuses the magnetisation along the transverse plane at the Echo Time (TE). The resulting echo is then sampled into one line of k-space. After that, the system waits for a period of time known as Repetition Time (TR) to allow the spins to relax back into the z axis. The same process is then repeated with a different phase encoding gradient. Each line of k-space requires the application of both 90° and 180° pulses and a new phase encoding gradient.

A Fast Spin Echo (FSE) also known as Turbo Spin Echo (TSE), applies multiple 180° RF pulses after a single 90° excitation pulse. Each 180° pulse reverses the effect of dephasing in the transverse plane (Hennig et al., 1986). With each 180° RF pulse, a new phase encoding gradient is applied, enabling the system to fill multiple lines of k-space with a single excitation pulse. As a result, FSE can produce an image in a much shorter amount of time compared to traditional SE. Figure 2.15 shows the differences between SE and FSE imaging sequences. The number of 180° pulses is known as echo train length of (ETL). This readout from a 90° pulse can last long as there is enough detectible magnetisation in the transverse plane (ultimately limited by *T2*) however, the length of ETL can affect the resulting image's contrast, signal to noise ratio and spatial resolution.

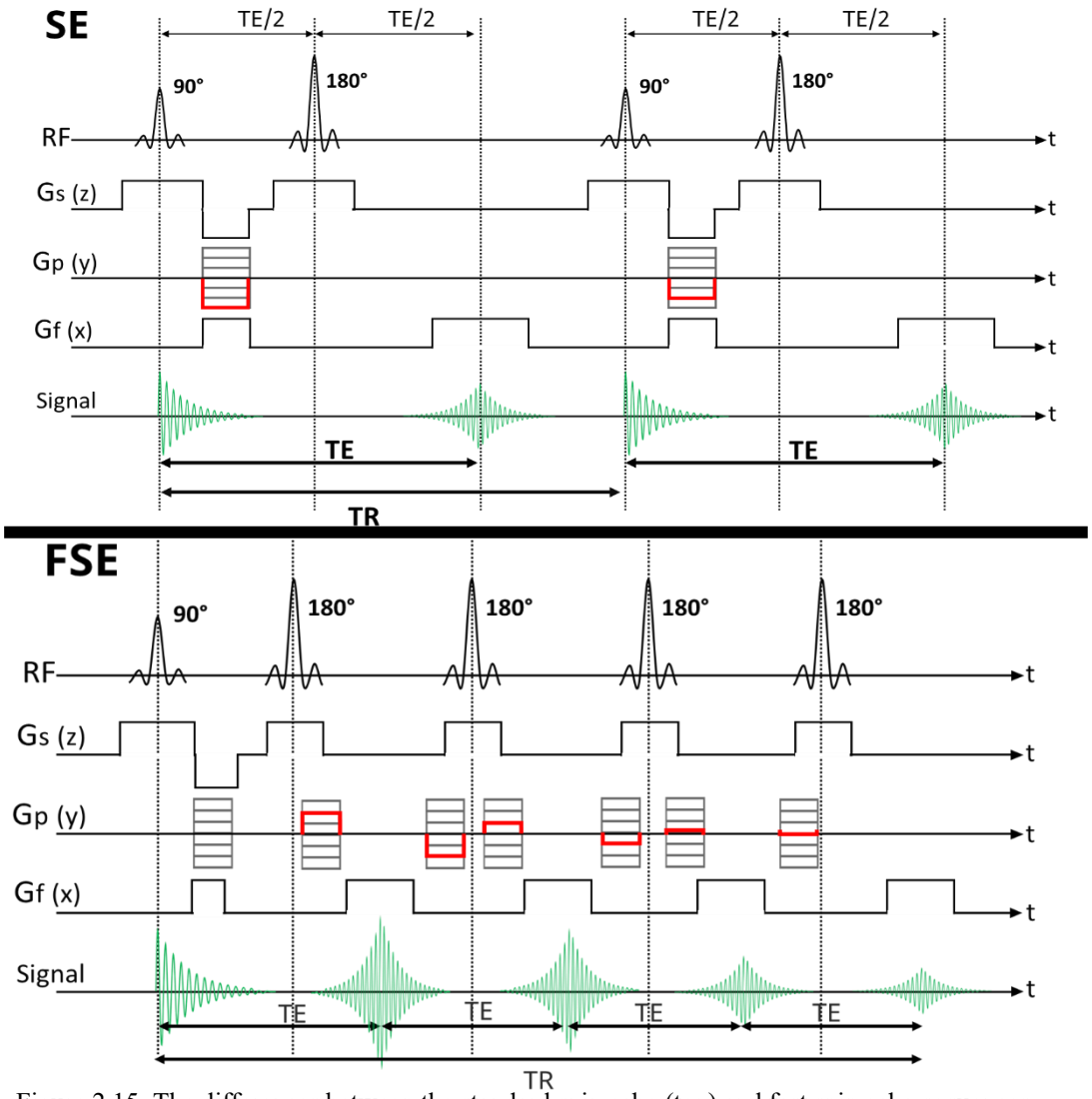

Figure 2.15: The differences between the standard spin echo (top) and fast spin echo sequences.

2.2.8 Gradient Echo Sequence (GRE)

The sequence structure of the Gradient Echo Sequence (GRE) is very similar to SE with minor differences that change the nature of spin manipulations (Hennig et al., 1986). GRE also starts with an excitation RF pulse that is less than or equal to 90° along with the slice selection gradient. However, unlike SE, GRE does not have the echo inducing 180° RF pulse. Instead, a negative frequency encoding gradient is applied with a certain length and magnitude further dephasing the transverse magnetization. Following the application of the phase encoding gradient, the induced

dephasing is reversed by applying a second gradient equal to the first one but with opposite polarity reversing the effect of the first applied gradient. The reversal of the transverse magnetisation dephasing generates a gradient echo (Figure 2.16). In general, in GRE, the flip angle is smaller than 90°. While the smaller flip angle leads to a smaller magnetisation in the transverse plane causing a smaller signal, the partial tilting of the magnetisation leads to a faster recovery resulting to faster image acquisition. After choosing a low flip angle and a short TR, the system reaches a steady state after a certain number of excitation pulses, allowing for faster image acquisition. The sequences utilising the fast steady-state acquisition are known as fast and ultra-fast gradient echo sequences. Fast gradient echo sequences allow the use of fast preparation pulses that alter the image contrast, such as chemically selective saturation (CHESS) (Haase et al., 1985) and inversion recovery fat suppression. As a result, Fast gradient echo sequences are frequently used in tissue that requires fast acquisition such as MR angiography and imaging the abdomen. GRE is more sensitive to field homogeneity and susceptibility effects compared to SE sequence.

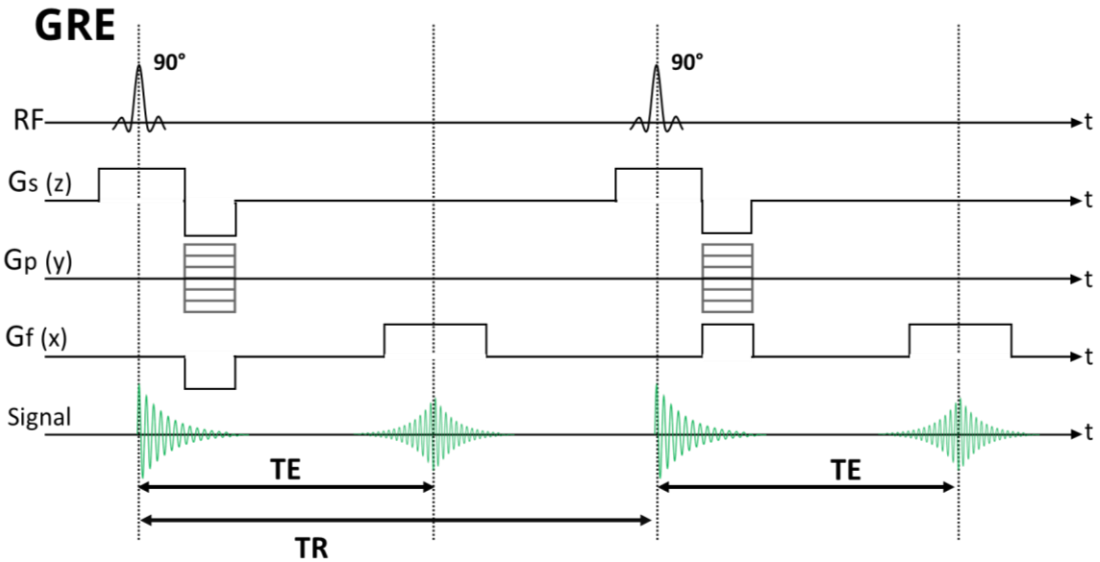

Figure 2.16: Gradient Echo pulse sequence schematic.

2.2.9 Fat and Water Separation

Fat suppression techniques in MRI play a vital role in various medical applications, such as improving the visibility of bone-marrow lesions, evaluating fat in soft-tissue masses, better definitions of lesions after administration of contrast material and avoiding chemical shift artefacts (Del Grande et al., 2014). Hence, multiple water and fat suppression techniques have been developed for a better fat and water separation in MRI.

To acquire an MR image in which water contributions to the signal is maximized and the fat signal is minimized or vice versa, two key differences between water and fat tissues are exploited, *T1* relaxation time and chemical shift. Fat tissue has a shorter *T1* relaxation time than water. Inversion recovery fat suppression techniques rely on this difference by using a TI time that nulls the fat signal. This causes all the fat tissue to have dark contrast compared to the bright water voxels. While *T1* fat suppression techniques are less prone to signal inhomogeneity compared to other methods, most *T1* based fat suppression sequences have low signal to noise ratio and in some cases result in a non-specific fat suppression (Delfaut et al., 1999).

Chemical shift fat suppression techniques use the frequency difference between water and fat tissue to acquire an image at a time when fat and water are partially or completely out of phase. Multiple fat suppression techniques take advantage of chemical shift such as chemical shift–selective fat suppression (CHESS) (Haase et al., 1985), spatial-spectral sequences (Del Grande et al., 2014), and Dixon fat-water separation techniques (Ma, 2008). Due to their dependence on homogenous B_0 fields, which are more difficult to attain at higher field strengths over larger fields of view, these approaches also suffer from non-specific fat suppression.

2.2.9.1 Dixon Fat and Water Separation Method

The original chemical shift based fat-water separation method was first described by Dixon in 1984 as a two-point method (Dixon, 1984). Since then, multiple variations have been developed which relies on the same principle such as the Iterative

Decomposition of Water and Fat With Echo Asymmetry and Least-Squares Estimation (IDEAL) by GE (Reeder et al., 2005), the 2- and 3-point techniques under the generic name DIXON developed by Siemens, the 2-point sequences "FatSep" by Hitachi , "WFOP" (Water-Fat Opposed Phase) by Canon and the multi-point modified Dixon ("mDixon") (Glover & Schneider, 1991) and Dual-Echo Dixon Imaging with Flexible Choice of Echo Times both developed by Philips (Eggers et al., 2011).

The basic idea of Dixon imaging is taken from concepts of magnetic spectroscopy. While fat shows a complex spectrum with multiple peaks with different amplitudes and frequencies on an NMR spectrum, fat is usually treated as a single frequency peak denoted by its largest peak for simplicity. Other complex sequences of fat suppression techniques such as IDEAL uses a multi-peak model for the fat spectrum (Bley et al., 2010) (Reeder et al., 2005).

The frequency shift between water and fat indicates a difference in phase. This means that at a certain point in time, the difference between the transverse spins of water and fat can be described by an angle which can vary depending on acquisition time. For example, assuming a difference in frequency between water and fat of 220 Hz at 1.5 T. Since the period equals 1/frequency, this means that the water and fat molecules will spin in and out if phase every 4.6 msec as shown in Figure 2.17. By changing TE, the signal can be acquired with a different angle between the water and fat spins. The original Dixon method was based on a two-point acquisition system.

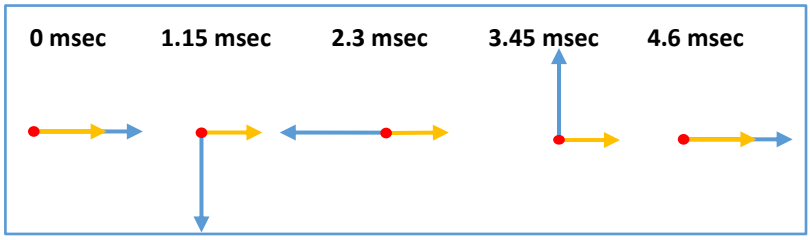

Figure 2.17: shows the phase difference between fat (yellow) and water (blue) in 1.5T field strength.

By acquiring an image where the angle between the water and fat is 0° (In Phase) TE= 0, 4.6, 9.2… and another image where the angle between the water and fat is 180° (Out of Phase) TE= 2.3, 6.9… .The first acquired image (In phase) equals the sum of both

the water and fat signal and the second image (out of phase) equals the difference between the water and fat signal as shown in Figure 2.18.

Hence:

$$\text{Water only Image (WO)} = 0.5 \times |S_{IP}+S_{OP}| \qquad (2.16)$$

$$\text{Fat only Image (FO)} = 0.5 \times |S_{IP}-S_{OP}| \qquad (2.17)$$

where S_{IP} is the signal acquired when fat and water are in phase and S_{OP} when they are out of phase. While the equations above give a simplified idea of how to calculate a water and fat signal, the actual calculations that are used are more complex as they take into account multiple variables such as B_o inhomogeneity and *T2** (Sharma et al., 2014a).

After Dixon's original design of the two-point system, the three-point Dixon sequences were developed as an improvement on the original (Yeung & Kormos, 2014). The three-point system works by acquiring an additional image in the order of (0°, 180°, 360°) or (-180°, 0°, 180°). Another modification on the original Dixon method was the iterative decomposition of water and fat with echo asymmetry and least-squares estimation (IDEAL). It is a three-point method in which the three imaging phases are timed so that each acquisition takes place at a different phase between the water and fat signals. Both modified Dixon approaches account for B0 and B1 magnetic field inhomogeneities (Costa et al., 2008).

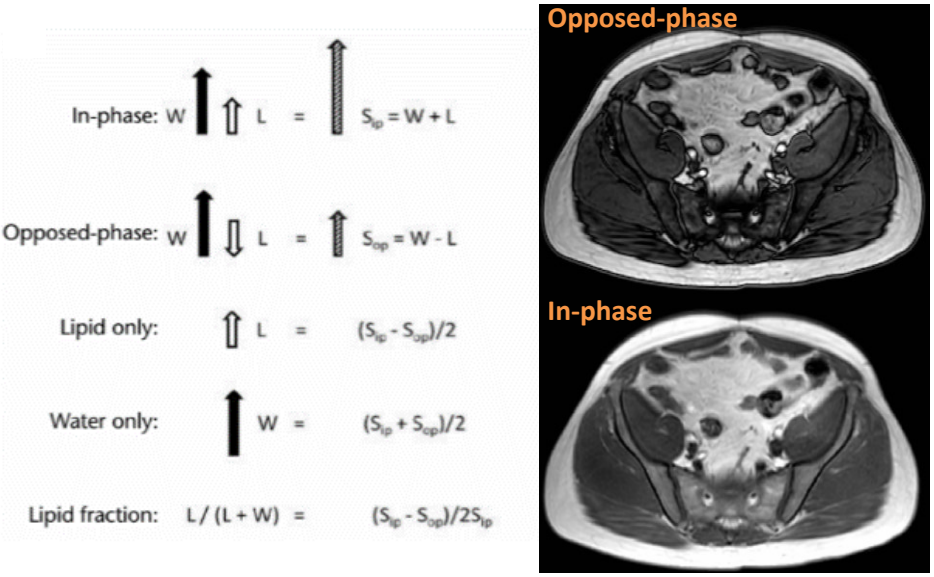

Figure 2.18: Shows the in-phase opposed-phased technique used in Dixon imaging (Sharma et al., 2014b).

2.3 Image Processing

Computers analyse images by treating them as numerical matrices where each cell in a matrix contains a number representing a pixel intensity value. As the human visual system can only recognise a limited number of grey scales, a typical JPEG image has a dynamic range of 8 bits, which can display 256 levels of brightness in each channel. In contrast, a 3T MRI image can have a dynamic range of up to 16 bits, which can display up to 65,536 levels of brightness or contrast. However, it's worth noting that the actual dynamic range of an MRI image can vary based on the specific imaging protocol and the type of tissue being imaged (Hoefflinger, 2015) (Gabr et al., 2008) . MRI data has a greater contrast to noise ratio compared to typical images which can be exploited by windowing (for visualisation) and in quantitative measurements. Hence, a larger dynamic range on the image data is needed. As a result, MRI image pixel values are often stored as floating points rather than integers. Many image processing algorithms were designed to operate on standard images and would fail if directly applied to MRI images. Therefore, in many cases, MRI images require adjustments before applying any image analysis, such as rescaling the intensity values on pixels to range from 0 to 1 or from 0 to 255, depending on the requirements of the analysis method.

2.3.1 Digital Image Filters

By treating the images as numerical matrices, mathematical, arithmetic, and logical operations can be used to manipulate the images in order to produce the desired result. These operations form the basis of digital image filtering. Images can be processed in the spatial domain by multiplying, adding, or subtracting values from each cell or in the frequency domain.

2.3.1.1 Image Convolution

Matrix convolutions is one of most used mathematical operations in spatial domain image processing. Convolution allows for fast multiplication of two numerical arrays of different sizes to generate a third array of which cells represent a linear combination

of the input arrays' cells. In image processing, the main input image is typically a grayscale image, while the second input image is much smaller in size known as a kernel. Changing the kernel's size and cell values can control the nature of the filtered image produced from the original input image. This is done by padding the kernel image across the main image, multiplying cell values, and summing the results to form the new cell values in the output image as shown in Figure 2.19. Filters are primarily used in image processing to reduce either high frequencies which can be used to smooth (blur) the image, or low frequencies which are used in highlighting edges in the image as shown in Figure 2.20. Low frequencies are also used to reduce hardware induced variations in the signal across the image (bias field correction). While a simple kernel can be used for image blurring as depicted in Figure 2.19, a gaussian blurring kernel can yield better results.

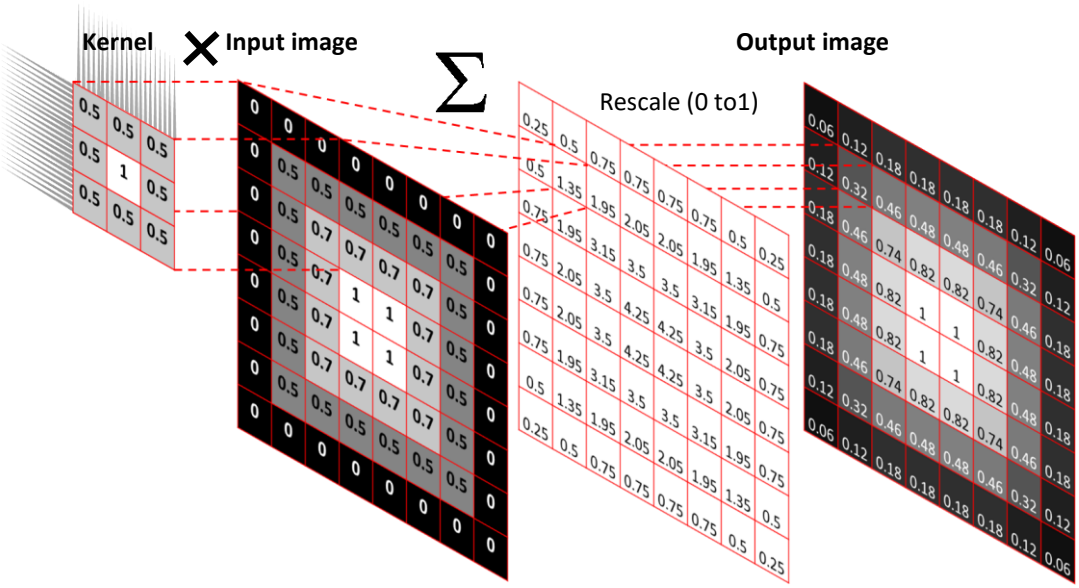

Figure 2.19: The use of 2D convolution in image processing, each cell in the output image is the sum of all the cells in the kernel multiplied by their corresponding cells in the input image. This process is repeated as the kernel moves around the input image covering all pixels.

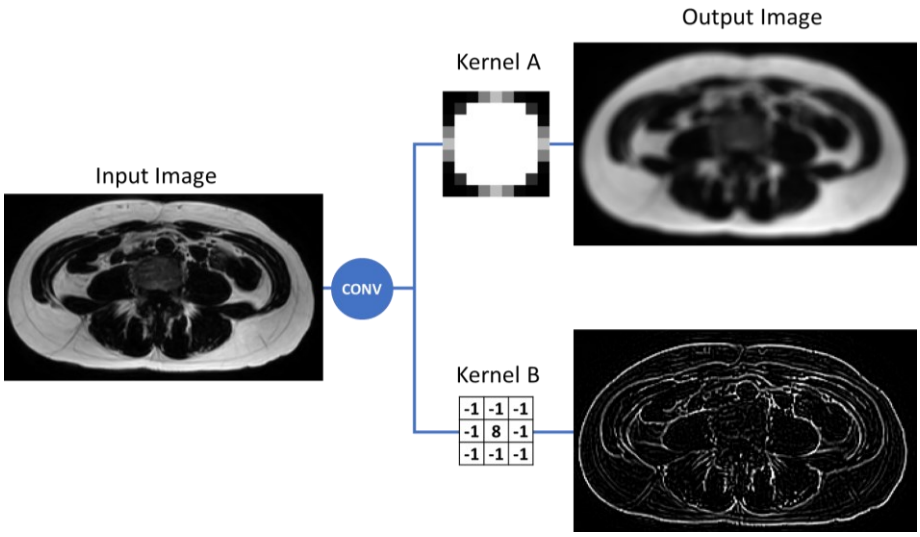

Figure 2.20: The use of different convolution kernels in generating different filtering outputs. Kernel A can be used in image smoothing while kernel B can be used in edge detection.

2.3.1.2 Image Frequency Domain Filters

Frequency domain operations require transforming an image into the frequency domain using Fourier transform, then multiplying it with a mask, and then transforming it back to the spatial domain. Similar to convolution kernels, the shape of the mask determines the output of the image frequency filters.

As previously explained, in MRI, an image's frequency domain is known as K-space. The frequency data distribution in an MRI image's k-space is identical to a 2D Fourier transform of a typical image where low frequency information is stored in the centre and high frequency information is located further from the centre of the k-space. Hence, multiplying a k-space with a mask containing zeros in the middle will eliminate the low frequency parts of the image. On the other hand, if multiplied with a mask containing zeros on edges rather than the middle, this will eliminate the high frequency parts of the image as shown in Figure 2.21.

Mathematically, the convolution process can be achieved faster using FFT. In the frequency domain, the Fourier Transform is used to convert the image and the kernel from the spatial domain to the frequency domain, where they are represented as

frequency spectra. The product of the two frequency spectra is then the convolution of the two functions in the spatial domain.

The advantage of using the frequency domain for convolution is that it is computationally efficient, as the convolution operation becomes a simple element-wise multiplication in the frequency domain.

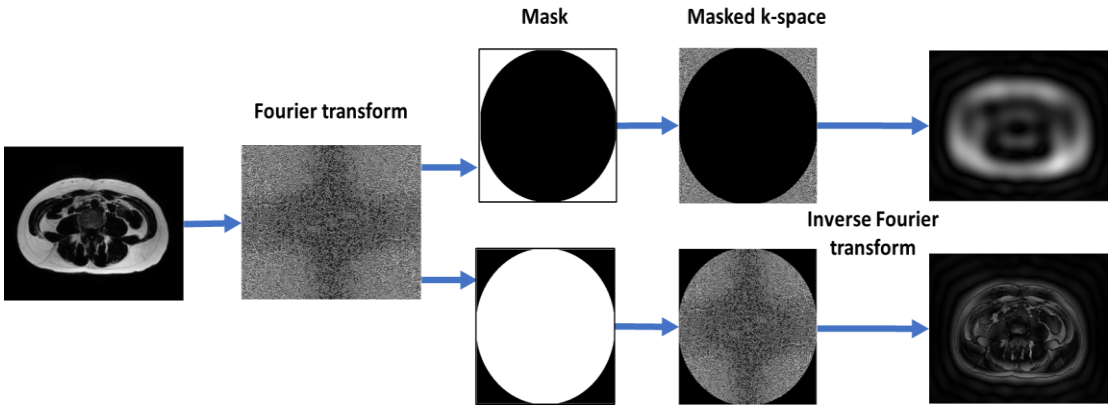

Figure 2.21: The use of different image frequency domain masks to generate different results by eliminating high or low frequency parts of an image.

2.3.2 Image Thresholding

Image thresholding describes the process of converting a grayscale image into a binary image where pixels with values above or below a selected threshold are converted into ones and all other pixels are converted into zeros. Manually choosing the most suitable threshold based on observations may be inaccurate in some instances, hence algorithms have been developed that automatically choose the ideal threshold that can covert the image into a black and white (zeros and ones) binary image while preserving the overall structure of objects in the image. Otsu's thresholding method operates by finding a threshold that minimizes the intraclass variance of the thresholded foreground and background pixels. Other thresholding methods were also developed such as Iterative thresholding, Peak-and-valley thresholding, and Fuzzy clustering thresholding (Sahoo et al., 1988). Thresholding is one of the key processes utilised in image segmentation as it can be used to differentiate between objects in an image based on pixel intensity as shown in Figure 2.22.

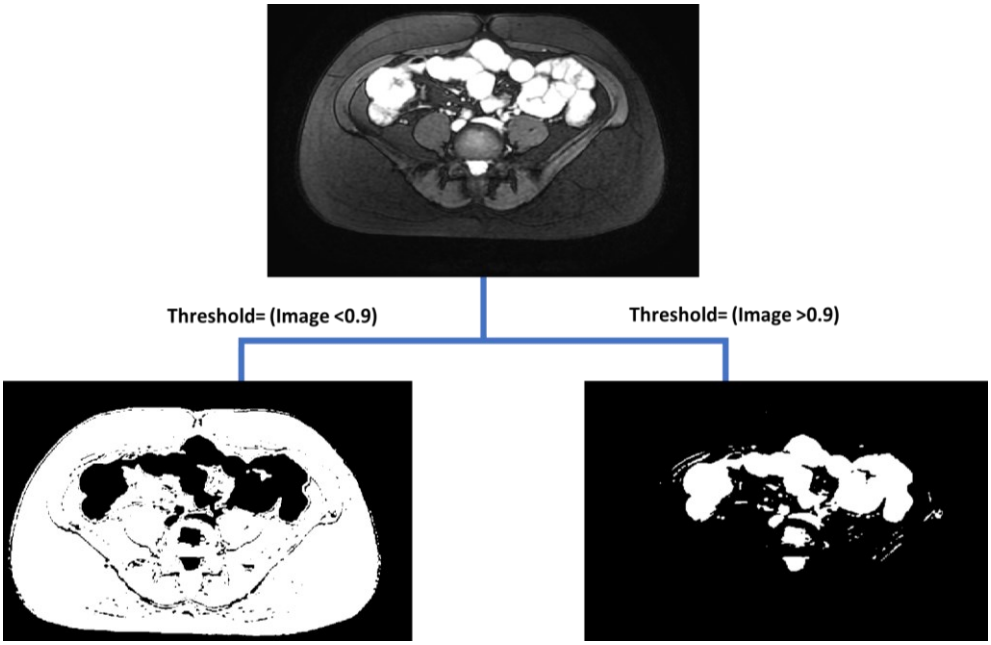

Figure 2.22: Pixel intensity thresholding used in segmenting high contrast bowels compared to the dark background tissue.

Choosing a single threshold for the whole image is knows as global thresholding. More advanced methods have been developed to generate multiple thresholding values based on local pixel intensity. These methods include adaptive thresholding and multilevel thresholding.

2.3.3 Morphological Operations

The basic concepts of morphological operations in image processing can be traced back to research on spatial set algebra and topology by Minkowski and Matheron (Mattioli, 1995) (Ackora-Prah et al., 2016). The term morphological operations describes a class of image analysis techniques that analyses images based on shapes. On a binary image, each group of white pixels, which are directly connected to each other are characterised as a distinct shape. These shapes can then be labelled, isolated, and reshaped based on the algorithm's structure.

2.3.4 Hit-and-Miss Transform

Morphological operations utilise hit and miss transformation to identify unique characteristics in a binary image. Similar to a convolution kernel, this is done by panning a mask with a specified size known as a structuring element across the image and comparing its configuration with the corresponding area on the image. A hit occurs when pixels on the structuring element match the pixels on the input image, and a miss occurs when they do not match. Based on the design of the structuring elements and the algorithm's instruction on what to do in the case of a hit or miss, these operations can be used to either detect certain aspects of the image or transform the image into a new shape.

2.3.5 Erosion and Dilation

As the name suggests, dilation causes an increase in the shape's border thickness, while erosion causes a decrease in the shape's thickness. Morphological erosion can transform a binary image into a skeletonized version of the shapes in input image by eroding the binary shapes into a line of single pixels. One of the simplest operators that can be used for erosion and dilation are the logical AND and OR operators. Figure 2.23 shows an example whereby using AND between the structuring element and the input image results in image erosion and using OR results in dilation of the original image.

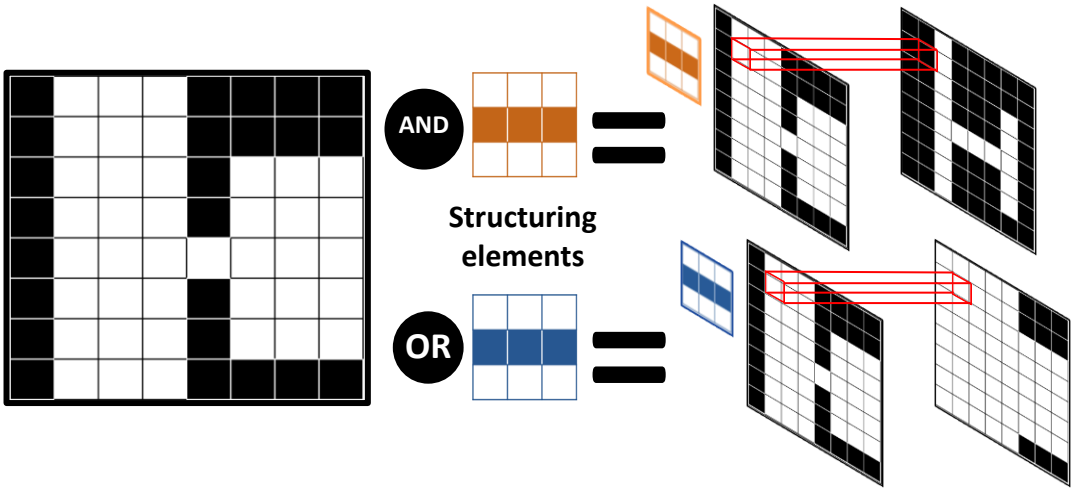

Figure 2.23: Using the same structuring element to preform erosion using *AND* operator where pixels are assigned the value of 1 only if all the pixels on the structuring elements match the corresponding pixels in the input image and dilation using *OR* operator where pixels are assigned value of 0 only if all the pixels on the structuring element do not match the corresponding pixels in the input image.

2.3.6 Connected-Component Labelling

Some structuring elements are designed to detect the connectivity of the pixels by identifying the connectivity of the pixel in the middle to surrounding pixels. A pixel is identified as connected to a surrounding pixel if it is directly attached to it from one of its the sides, this is known as 4-connected pixels, or from the corners, this is known as 8-connected pixels. This is done by placing the middle pixel of the element on one of the foreground pixels (white) and labelling all the connected pixels to the central pixel. After this the structuring element is then shifted to the newly labelled pixel and the connectivity is checked again. The newly discovered connected pixel is then labelled provided it has not already been labelled. Once all the pixels in a shape have been labelled, the algorithm assigns a number to the connected shape and moves on to the next shape as shown in Figure 2.24. In literature, structuring elements used to identify 4-connected pixels is known as Von Neumann neighbourhood and structuring elements used to identify 8-connected pixels is known as Moore neighbourhood. This process forms the foundation of many connected component labelling algorithms using more advanced variations with higher connectivity of up to 26 points in 3 dimensions.

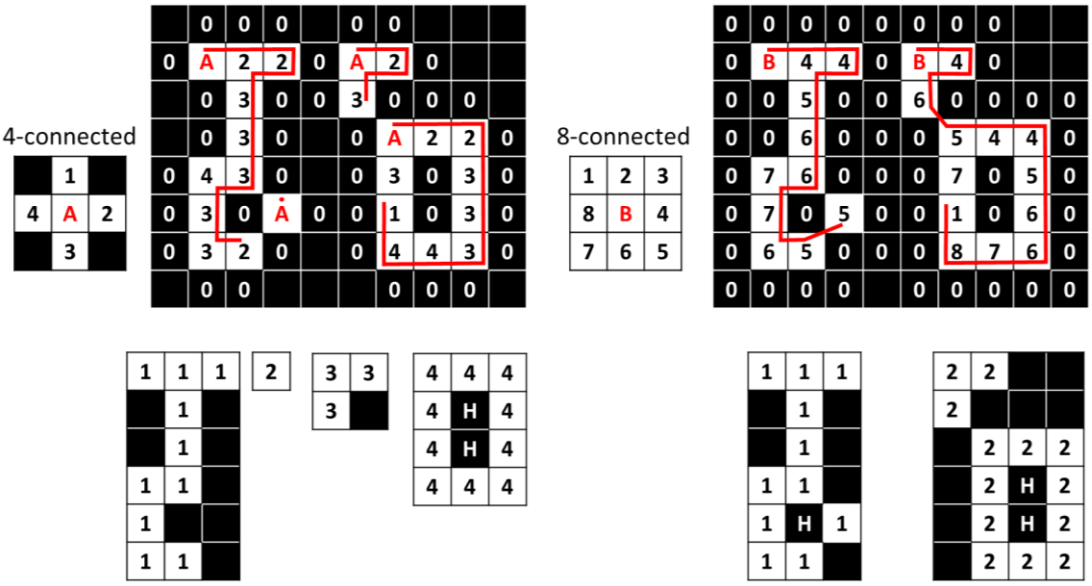

Figure 2.24: The process of identifying individual shapes in a binary image using 4 and 8 connected points.

2.4 Chapter Summary

This chapter introduced the principles underlying the formation of NMR signal and MRI image acquisition techniques. Dixon fat and water separation techniques explained in this chapter will be used to analyse abdominal fat in later chapters. The chapter also explains image analysis techniques that are used throughout this thesis.

The invention of MRI ushered in a new age of medical innovations and redefined the way we think about medical imaging. Advances in computer sciences accelerated the conversion of theoretical concepts of physics, arithmetic, and topology into real-world applications that save lives every day. Compared to other medical imaging modalities, which primarily rely on advances in engineering and technology, MRI is only bound by the imagination and creativity of scientists who can create new imaging sequences that can reveal a part of human physiology that has not been seen before using the same MRI machine structure.

References

Ackora-Prah, J., Acquah, R. K., & Ayekple, Y. E. (2016). Mathematical Morphological Distributive Concepts over Unions and Intersections. *Advances in Pure Mathematics*, *06*(10), 633–637. https://doi.org/10.4236/apm.2016.610052

Bley, T. A., Wieben, O., François, C. J., Brittain, J. H., & Reeder, S. B. (2010). Fat and water magnetic resonance imaging. In *Journal of Magnetic Resonance Imaging*. https://doi.org/10.1002/jmri.21895

Bloch, F. (1946). Nuclear induction. *Physical Review*, *70*(7–8), 460–474. https://doi.org/10.1103/PhysRev.70.460

Costa, D. N., Pedrosa, I., McKenzie, C., Reeder, S. B., & Rofsky, N. M. (2008). Body MRI using IDEAL. *American Journal of Roentgenology*, *190*(4), 1076–1084. https://doi.org/10.2214/AJR.07.3182

Hoefflinger, B. (2015). HDR- and 3D-vision sensors. CHIPS 2020 VOL. 2: New Vistas in Nanoelectronics, 201–209. https://doi.org/10.1007/978-3-319-22093-2_13/COVER

Del Grande, F., Santini, F., Herzka, D. A., Aro, M. R., Dean, C. W., Gold, G. E., & Carrino, J. A. (2014). Fat-Suppression Techniques for 3-T MR Imaging of the Musculoskeletal System. *RadioGraphics*, *34*(1), 217–233. https://doi.org/10.1148/rg.341135130

Delfaut, E. M., Beltran, J., Johnson, G., Rousseau, J., Marchandise, X., & Cotten, A. (1999). Fat Suppression in MR Imaging: Techniques and Pitfalls. *RadioGraphics*, *19*(2), 373–382. https://doi.org/10.1148/radiographics.19.2.g99mr03373

Eggers, H., Brendel, B., Duijndam, A., & Herigault, G. (2011). Dual-echo Dixon imaging with flexible choice of echo times. *Magnetic Resonance in Medicine*. https://doi.org/10.1002/mrm.22578

Glover, G. H., & Schneider, E. (1991). Three-point dixon technique for true water/fat decomposition with B0 inhomogeneity correction. *Magnetic Resonance in Medicine*. https://doi.org/10.1002/mrm.1910180211

Haase, A., Frahm, J., Hanicke, W., & Matthaei, D. (1985). 1H NMR chemical shift selective (CHESS) imaging. In *Physics in Medicine and Biology* (Vol. 30, Issue 4, pp. 341–344). IOP Publishing. https://doi.org/10.1088/0031-9155/30/4/008

Hahn, E. L. (1950). Spinechoes. In *Phys Rev Lett* (Vol. 80, Issue 4, pp. 580–594).

Hennig, J., Nauerth, A., & Friedburg, H. (1986). RARE imaging: A fast imaging method for clinical MR. *Magnetic Resonance in Medicine*, *3*(6), 823–833. https://doi.org/10.1002/mrm.1910030602

Ma, J. (2008). Dixon techniques for water and fat imaging. *Journal of Magnetic Resonance Imaging*, *28*(3), 543–558. https://doi.org/10.1002/jmri.21492

Sahoo, P. K., Soltani, S., & Wong, A. K. C. (1988). A survey of thresholding techniques. In *Computer Vision, Graphics and Image Processing* (Vol. 41, Issue 2, pp. 233–260). Academic Press. https://doi.org/10.1016/0734-189X(88)90022-9

Mattioli, J. (1995). Minkowski operations and vector spaces. In *Set-Valued Analysis* (Vol. 3, Issue 2, pp. 211–212). Kluwer Academic Publishers.. https://doi.org/10.1007/BF01038601

Purcell, E. M., Torrey, H. C., & Pound, R. V. (1946). Resonance absorption by nuclear magnetic moments in a solid [7]. In *Physical Review* (Vol. 69, Issues 1–2, pp. 37–38). American Physical Society. https://doi.org/10.1103/PhysRev.69.37

Reeder, S. B., Pineda, A. R., Wen, Z., Shimakawa, A., Yu, H., Brittain, J. H., Gold, G. E., Beaulieu, C. H., & Pelc, N. T. (2005). Iterative decomposition of water and fat with echo asymmetry and least-squares estimation (IDEAL): Application with fast spin-echo imaging. *Magnetic Resonance in Medicine*. https://doi.org/10.1002/mrm.20624

Sharma, P., Altbach, M., Galons, J. P., Kalb, B., & Martin, D. R. (2014a). Measurement of liver fat fraction and iron with MRI and MR spectroscopy techniques. In *Diagnostic and Interventional Radiology*. https://doi.org/10.5152/dir.2013.13124

Sharma, P., Altbach, M., Galons, J. P., Kalb, B., & Martin, D. R. (2014b). Measurement of liver fat fraction and iron with MRI and MR spectroscopy techniques. *Diagnostic and Interventional Radiology*, *20*(1), 17–26. https://doi.org/10.5152/dir.2013.13124

Dixon, W. T. (1984). Simple proton spectroscopic imaging. *Radiology*, *153*(1), 189–194. https://doi.org/10.1148/radiology.153.1.6089263

Yeung, H. N., & Kormos, D. W. (2014). Separation of true fat and water images by correcting magnetic field inhomogeneity in situ. *Radiology*. https://doi.org/10.1148/radiology.159.3.370415

3 Crohn’s Disease

3.1 Introduction

Crohn’s Disease (CD) is a chronic, relapsing and remitting inflammatory disease affecting the gastrointestinal tract. Recently, the prevalence of Crohn's disease has been increasing, reaching up to 157 per 100,000 people, which means that there are currently at least 115,000 CD patients in UK alone. Up to a third of CD patients are diagnosed before the age of 21 (NICE, 2019). In Scotland and Lothian, IBD prevalence is 1 in 125 (0.8%) (Jones et al., 2019).

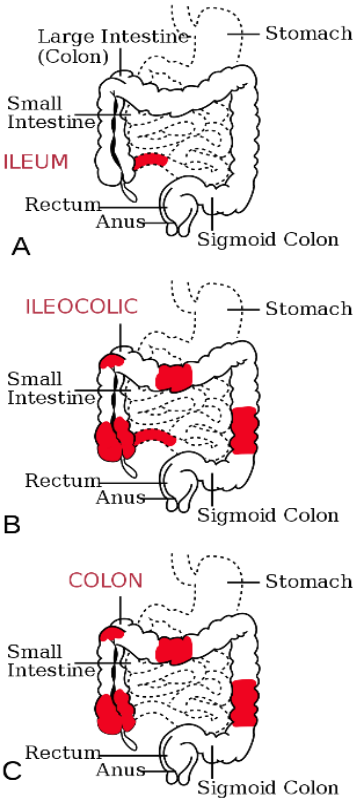

Figure 3.1: The most common sites of intestinal involvement in Crohn's disease (Fvasconcellos, 2006).

CD is considered one of the main inflammatory bowel diseases (IBDs). The two major types of IBD are ulcerative colitis and Crohn's disease (Lamb et al., 2019). While the effects of ulcerative colitis are restricted to the colon and the large intestines, CD can affect any part of the gastrointestinal tract from the mouth to the anus (Figure 3.1).

For treatment and research purposes, CD has been identified to have three states: inflammatory, stricturing, and fistulising. Inflammatory CD is identified by inflammation of the gastrointestinal tract with no apparent evidence of stricturing or fistulising disease. This inflammation can eventually lead to luminal narrowing and fibrosis. These patients become classified as having stricturing disease. Once fibrostenotic changes take place, it becomes irreversible and needs surgical intervention. Fistulizing CD occurs when the transmural inflammation continues to develop a sinus or fistulous tract. Fistulae can appear between the bowel and any other

adjacent organ. If the fistulous tract is not complete between the bowel and an adjacent organ, an intra-abdominal abscess may develop (Feuerstein & Cheifetz, 2017a).

Due to the complex pathology of CD, a clear cause and effect relationship cannot be used to indicate the underlying principle of the disease. However, the causes of CD can be attributed to genetic predisposition, intestinal microorganisms' interactions and immune reactivity. Intestinal inflammation occurs due to a dysregulated immune reactivity to the gastrointestinal microbiota of genetically susceptible individuals (Shanahan, 2002). One of the highest numbers of observed CD incidents was in Europe and North America (322 and 319 per 100,000 persons per year, respectively). Developing countries have reported a lower prevalence of CD. Hence, it has been suggested that environmental and dietary factors could increase the risk of CD (Holt et al., 2017).

CD patients are classified into three categories (mild, moderate and severe) based on their symptoms and disease activity. Mild CD patients can tolerate oral nutrition and show no significant signs of dehydration, abdominal pain, or ileus. Nor do they show severe body weight loss. Moderate CD patients suffer from intermittent vomiting, painful mass and weight loss of more than 10% of their body weight. Despite intensive treatment, severe CD patients suffer from drastic body weight loss, ileus, abscess, or persistent symptoms. Treatment and disease management procedures tend to differ based on these stages of disease activity (Travis et al., 2006).

3.2 Crohn's Disease Clinical Indices

The complicated pathology of the disease and the uncertainty of the direct causes of CD make it difficult to use a single direct method for disease activity assessment. Hence, multiple disease activity metrics have been developed for this purpose. These activity indexes differ in both diagnostic modalities and the variables they consider.

There are also several standardised guidelines for the assessment of CD, such as the Guideline for Diagnostic Assessment (ECCO-ESGAR) (Maaser et al., 2019) (Sturm et al., 2019). These assessment guidelines and procedures are based on objective findings

of endoscopic, radiological and histological examinations (Feuerstein & Cheifetz, 2017b).

Common clinical findings that are associated with CD include (Khoshkish et al., 2012):

1. Clinical history compatible with symptoms such as diarrhoea, abdominal pain, malaise, weight loss, and/or rectal bleeding.
2. Endoscopic findings of cobblestone, ulcers, skip lesions or perianal disease.
3. Radiological findings of fistula, stricture, or discrete ulceration with "skip" areas.
4. Macroscopic evidence of bowel wall thickening, mesenteric lymphadenopathy and creeping fat during surgery.
5. Histopathologic findings of noncaseating epithelioid granulomas or transmural inflammation.

3.2.1 The Crohn's Disease Activity Index

The Crohn's Disease Activity Index (CDAI) was primarily developed as a method of assessment of disease response to treatment. It consists of eight variables related to the disease, where each one is given a specified weighting based on its ability to predict disease activity. Table 3.1 shows these variables along with their weighting. These variables are then used to calculate a score which indicates disease activity that ranges from 0 to over 600. While upper limits could not be defined due to variables such as body weight and haematocrit levels, cut-off values were recognised based on recorded scores for a group of 112 patients, which were compared with patients' medical conditions. A CDAI score of 150 or lower represents inactive disease, and a score of 450 represents severe disease conditions (Best et al., 1976) (Connors, 2011). Other activity indexes were developed, such as patient reported outcomes (PRO2) which uses only the number of liquid or very soft stools and reported levels of abdominal pain (Khanna et al., 2015). Another index is the Harvey-Bradshaw index, which relies on general wellbeing, abdominal pain, number of liquid stools per day, abdominal mass and the nature of complications that occur (Harvey & Bradshaw, 1980)

Table 3.1: CDAI variables and weights

Variable	Scale	Weight
Liquid or very soft stools	Daily number of stool count summed over for 7 days	2
Abdominal pain	Daily ratings of abdominal pain summed over 7 days where: 0 = none, 1 = mild, 2 = moderate, 3 = severe	6
General wellbeing	Daily ratings of general wellbeing summed over 7 days where: 0 = generally well, 1 = slightly below par, 2 = poor, 3 = very poor, 4 = terrible	6
Features of extraintestinal disease	Any of the following present during the previous 7 days	
	a) Arthritis or arthralgia	20
	b) Skin or mouth lesions, including pyoderma, gangrenosum, erythema nodosum, aphthous stomatitis	20
	c) Iritis or uveitis	20
	d) Anal fissure, fistula, or peri-rectal abscess	20
	e) Other external fistula	20
	f) Fever > 100°F	20
Antidiarrheal use	0 = no, 1 = yes	30
Abdominal mass	0 = none, 2 = questionable, 5 = definite	10
Hematocrit	47- hematocrit (males)	6
	42- hematocrit (females)	6
Body weight below standard	100 [1 − (body weight/standard weight*)]	1

*Standard Body weight is defined as body weight before CD. If it is unavailable, the population mean weight for a patient's sex, age, and height is used.

3.2.2 Endoscopy

Endoscopy is the gold standard investigative modality used in disease activity monitoring in IBD (Maaser et al., 2019). The CD Endoscopic Index of Severity (CDEIS) is a scoring system that relies on endoscopic procedures to examine the five intestinal segments: ileum, right colon, transverse colon, left colon, sigmoid and rectum. The original scoring system relied on relatively complex endoscopic

observations such as deep ulcers, superficial ulcers, the ratio of surface affected by disease and the ratio of surface affected by ulcers. Each of these variables is given a specific weight, and a total score is calculated (Mary & Modigliani, 1989). In 2004 a group of researchers developed a simplified endoscopic scoring system called simplified endoscopic activity score for CD (SES-CD) (Daperno et al., 2004), which relies on ulcer size, ulcerated and affected surfaces, and stenosis. CD can also be monitored by examining mucosal healing. Research data indicates that achieving mucosal healing monitored by endoscopy may improve the outcome of the disease (Schnitzler et al., 2009) (Baert et al., 2010).

Both CDEIS and SES-CD demonstrated a good correlation with disease activity when they were used to track therapeutic changes in CD (Sipponen et al., 2010). However, it is very difficult to rely solely on endoscopy to assess disease activity as it has significant drawbacks. These disadvantages include not providing detection of inflammation on deeper layers of the intestine and the extraintestinal and dependency on the operator. Patients do not usually consent to endoscopy even though its relatively safe, and finally, the required degree of endoscopic healing and the different types of lesions are not well established (Benitez et al., 2013).

3.2.3 Biochemical Biomarkers

Some biochemical biomarkers, such as faecal calprotectin (FC), are also used in the diagnostic process of IBDs due to their easy accessibility. In some cases, faecal markers can even help avoid endoscopic procedures (Vermeire et al., 2006). The presence of several neutrophil-derived proteins in the stools, such as calprotectin, is proportional to neutrophil migration to the gastrointestinal tract and can predict mucosal healing (Røseth et al., 2004). As it is a measure of inflammation, FC is not disease specific. While FC can be a reliable tool for the detection of colonic mucosal inflammation, it is less sensitive in the detection of small intestinal CD (Zittan et al., 2018). FC is typically used in conjunction with endoscopic examination (Bjarnason, 2017).

C-reactive protein (CRP) is considered one of the most important up-regulated proteins during an acute-phase stimulus. Several conditions are associated with a CRP response,

such as inflammatory diseases, infectious stimuli, tissue necrosis, neoplasia and childbirth. Researchers and clinicians use CRP as one of the biomarkers when making treatment decisions for CD patients (S. Vermeire, Van Assche, & Rutgeerts, 2004). While both moderate and severe patients show high levels of CRP (Baumgart, 2018), the sensitivity of CRP in predicting disease activity is highly dependent on cut-off values, and a significant number of CD patients demonstrated low CRP levels despite clinically active disease (Magro et al., 2014).

3.3 Cross Sectional Imaging in CD

Due to their practical, objective, and non-invasive approach, the use of cross-sectional imaging techniques to monitor CD have been increasing rapidly. These techniques include Ultrasound (US), Computed tomography (CT) and MRI. Cross-sectional imaging allows for the analysis of features and characteristics of the abdomen that are inaccessible via traditional endoscopic techniques (Benitez et al., 2013). Because of this, the disease assessment criteria and variables for CD in cross-sectional imaging differ from endoscopic indexes of disease activity. While US has been used in CD, it is reported to have an inferior diagnostic accuracy and poorer disease localisation for CD compared to existing MRI techniques, with greater inter- and intra-observer variability (Taylor et al., 2018). Many CT and MR imaging procedures used for CD require the intestines to be distended using relatively high amounts of intraluminal contrast agents for better visualisation of anatomical references and of morphologic features caused by the disease (Furukawa et al., 2007). More specifically, MRI and CT require the use of oral and intravenous contrast agents to better highlight the inflamed regions.

3.3.1 MRI Disease Activity Indexes

Recent advances in MRI enable it to achieve very high accuracy for assessing disease activity in CD. Hence, MRI became one of the most popular CD assessment modalities for its ability to image soft tissues without the use of the harmful ionising radiation found in CT.

Multiple MRI-based disease activity indexes and grading systems were developed for monitoring CD. The Magnetic Resonance Index of Activity (MaRIA) (Rimola et al., 2011) mainly focuses on five aspects of the disease. These aspects include bowel wall thickness (in mm), ulcers, oedema, measurements of wall signal intensity (WSI) before and after intravenous (IV) contrast administration and relative contrast enhancement (RCE) of the intestinal wall.

The MaRIA score depends on intravenous injection of gadolinium as a contrast agent for the measurement of bowel wall thickness, where a volumetric interpolated breath-hold examination (VIBE) sequences is acquired before and after administering gadolinium. T2-weighted scans and pre- and postcontrast-enhanced T1-weighted scans are used along with fat saturation to detect the presence of oedema. This is because fat saturation allows for better identification of mural oedema and perienteric inflammatory changes. Each patient is required to consume 1500 mL of a 2.5% mannitol solution 45 minutes prior to the MRI in order to achieve an adequate distension of the entire small intestine. Patients who could can not tolerate such a large volume of luminal contrast are instructed to consume 750–1000 mL of the same solution instead, as this amount is sufficient to achieve the ideal distension of the terminal ileum. The MaRIA score was validated by comparing the results with the endoscopic CDEIS index.

MaRIA score is calculated using the following formula for each segment:

MaRIA (segment) = (Wall thickness in millimetres × 1.5) + (Relative contrast enhancement × 0.02) + (Oedema × 5) + (Ulceration × 10).

Figure 3.1 shows MRI images acquired for MaRIA score index along with a corresponding endoscopic image.

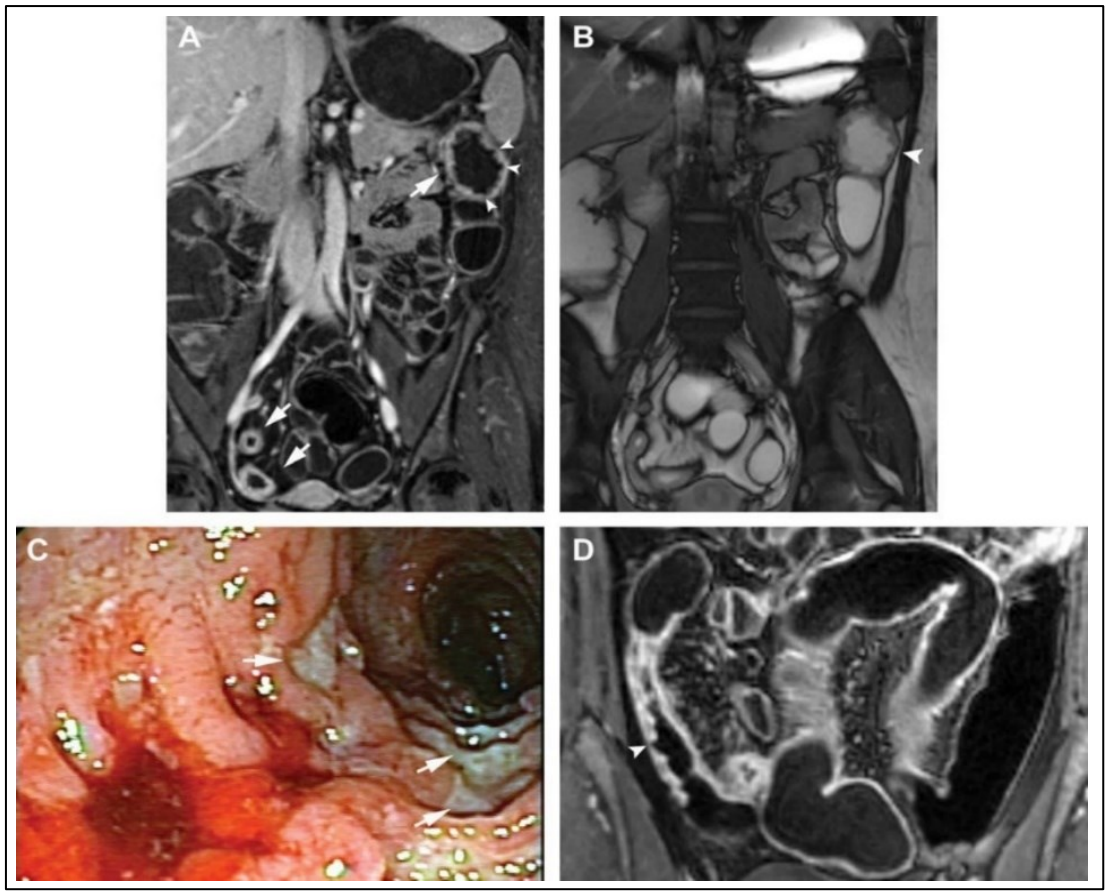

Figure 3.1: Ulcerative lesions of large bowel using MaRIA score method. (A) Bowel wall thickening and diffuse hyperenhancement after intravenous contrast of the distal ileum and splenic flexure (arrows). Ulcers can also be seen in T2 sequences (arrowhead in B). (C) Ulceration in the same segment seen at endoscopy. (D) Ulceration in the terminal ileum (arrowheads), along with the presence of wall thickening and hyperenhancement of the ileal segment (Rimola et al., 2011).

Similar to the MaRIA score, the Clermont score is a T2-weighted imaging based system which relies on quantitative measurements such as bowel wall thickness (in mm), ulcers, and oedema (Buisson et al., 2013). Table 3.2 shows the different parameters used in calculating MaRIA and Clermont indexes. The key difference in the Clermont score method is that it avoids the use of gadolinium by taking advantage of Diffusion Weighted Imaging (DWI). Using the most affected digestive segment to calculate the Apparent Diffusion Coefficient (ADC) showed a high correlation with MaRIA scores. This was also confirmed by other studies (Rozendorn et al., 2018).

Other disease activity indexes, such as the Crohn's Disease MRI Index (CDMI) (Steward et al., 2012), which relies on expert radiologists to rank disease features found on MRI images on a scale of 0-3 based on observed features severity. The Magnetic

Resonance Enterography Global Score (MEGS) is an index based on CDMI, however, it involves the addition of another specific key parameter, the length of the affected bowel (Makanyanga et al., 2014) (Rozendorn et al., 2018).

Table 3.2: MRI-based parameters included in MaRIA and Clermont activity index

	MaRIA	Clermont
Relative Contrast (RCE)	0.02 × (RCE)	-
Bowel wall Enhancement thickness	1.5 × thickness in (mm)	1.646 × thickness in (mm)
Presence of ulcers	+10 (if yes)	+8.036 (if yes)
Presence of Oedema	+5 (if yes)	+5.613 (if yes)
Apparent Diffusion Coefficient (ADC)	_____	-1.321×ADC
Constant	+5.039	_____

As traditional MRI-based disease assessment methods rely on intravenous gadolinium, CD patients typically undergo repeated exposure to gadolinium administration which adds cost and places patients at risk of various complications. These complications include possible nephrogenic systemic fibrosis, allergic reaction, and long-term brain deposition following repeated use (US FDA, 2017). Hence, the development of contrast-free MRI imaging sequences eliminates these risks associated with gadolinium and allow for a more frequent and overall safer assessment of the disease progression.

3.3.2 Computed Tomography

CT has been used for many years as a diagnostic tool for CD. CT Enterography (CTE) is a non-invasive imaging technique that offers a better small bowel visualisation than the standard abdominopelvic CT. CTE complements ileocolonoscopy (IC) and can visualise and even reveal small bowel inflammation in approximately 50% of CD patients who show no signs of CD in endoscopic examination. This diagnostic method also has evolved more recently in contrast-enhanced examination that uses intravenous administration of iodine contrast agents and CT-enteroclysis, which can be obtained by using a sizable amount of contrast agent administered orally (1500 to 2000 mL or more) or by positioning a nasojejunal tube; this technique typically allows the evaluation of the colon as well (Saibeni et al., 2007). The CT technique combines small bowel

distension with oral contrast and abdominopelvic CT examination in the intestinal phase after intravenous contrast medium administration. Patients are required to drink approximately 1.5–2 litres of oral contrast over 45–60 min. Contrast agents maximise the contrast between the small bowel wall and the lumen, providing an assessment of bowel wall enhancement patterns and mucosal thickening. The most common CT scan findings in CD patients include submucosal fibro-fatty infiltration, mesenteric adenopathy, engorged ileal vasa recta, small bowel wall stratification and thickening, with or without contrast enhancement (Saibeni et al., 2007). Figure 3.2 shows examples of active CD manifestations in CT.

Figure 3.2: Examples of active CD manifestations in CT. A: wall thickening and mucosal hyperemia encompassing a segment of ileum (arrow). B: long segment of markedly thickened inflamed bowel in the pelvis (arrows). C: an acutely inflamed loop of colon (arrow). D: thickening and mucosal hyperemia of the terminal ileum. E: thickening of an intermediate length segment of terminal ileum (arrow); F: marked thickening, mucosal hyperemia, and adjacent vasa recta engorgement of the neo-terminal ileum (arrow) (Guglielmo et al., 2020)

Precise small bowel distension is essential for evaluating bowel wall thickness and mucosal enhancement. Accurate detection of small bowel pathology requires detailed luminal navigation from the gastro-oesophagal junction to the anus (Ilangovan et al., 2012).

Mao et al., compared the use of CTE in evaluating postoperative recurrence of CD after ileocolic resection (ICR). They examined 32 CD patients that underwent ICR. Rutgeerts score (i0-i4) was used to define endoscopic recurrence, whereas CTE recurrence was determined by a previously validated CTE score (CTE0–CTE3). Their results shows a good correlation between CTE and endoscopic recurrence ($r = 0.782$, $P < 0.0001$) (Mao et al., 2013).

Mohamed et al., evaluated the accuracy of CTE radiological signs of gastrointestinal inflammation in determining disease activity in CD patients. Parameters such as abnormal wall thickening, mucosal enhancement, enlarged mesenteric lymph nodes, engorged vasa recta, and increased mesenteric fat density were assessed using CT enterography in 26 CD patients. Their results showed significant differences between moderate and severe histological findings when assessing engorged vasa recta, fat oedema and lymph node enlargement. However, no significant differences between moderate and severe diseases were found in bowel wall thickening and mucosal enhancement (Mohamed et al., 2012).

While CT has a better spatial and temporal resolution, MRI offers a better contrast resolution and may show fistulae better than CT. Adults may also experience less risk from gadolinium-based intravenous contrast than they would from iodinated contrast in a CT scan (Ilangovan et al., 2012). Nevertheless, research revealed that the diagnostic performance of small intestinal CT and MRI was comparable. Radiation exposure is also considered as a major drawback of CT. Puylaert et al., analysed 19 publications that used imaging modalities as a grading method for disease activity in CD. Their data showed a disease grading accuracy of 86% for MRI, 84% for CT and 44% for Ultrasound on a per-patient study basis (Puylaert et al., 2015).

3.4 CD Treatment

As a chronic illness, CD therapy mainly focuses on treating symptoms, inducing remission as an interim measure, and maintaining remission in the long term. Hence, CD management requires a stepwise escalation of treatment measures tethered with constant monitoring of the disease activity levels and progression. In the initial

diagnosis and management of CD, laboratory testing, endoscopic evaluation, and faecal biomarkers are frequently used. Imaging is also crucial to the diagnosis and assessment of IBD. Throughout a patient's lifetime, many imaging modalities can be employed, from the initial screening and diagnosis of IBD to establishing the degree of intestinal involvement, tracking disease activity, and assessing for consequences of untreated IBD. When considering factors such as the cost, radiation exposure, the requirement for anaesthesia, and image quality, each available imaging modality has its own set of advantages and risks (Haas et al., 2016).

Intestinal resection is needed in about two-thirds of CD patients at some point throughout their history. The diseased bowel cannot be completely removed surgically, and postoperative recurrence (POR) is still a common complication. Within a year of resection, 70% to 90% of patients experienced endoscopic recurrence. Currently, Ileocolonoscopy (IC) is regarded as the "gold standard" for POR detection. The severity of the recurrence, as determined by the Rutgeerts score, strongly predicts the return of symptoms, the emergence of CD-related problems, and the requirement for additional surgery. However, IC can only distinguish the intestinal mucosa inside the endoscope's field of view. Patients with proximal upper small bowel lesions and anastomotic stenosis could not be examined for neoterminal ileum lesions. Additionally, IC was unable to detect extraintestinal problems, including abscess and fistula, which may have affected the therapeutic approach (Mao et al., 2013).

When Crohn's disease first presents or flares up in a 12-month period, monotherapy with traditional glucocorticosteroid is used to induce remission. Glucocorticoids can suppress proinflammatory proteins' expression and up-regulate anti-inflammatory proteins (Rhen & Cidlowski, 2005). Immunomodulatory drugs, such as thiopurines or methotrexate are effectively considered as first line therapies in the management of CD. Patients who are intolerant or refractory to immunomodulatory agents can be treated with biological agents like anti-TNF therapy (Infliximab, NAPP pharmaceuticals or Adalimumab, Abbvie), anti-integrin therapy (Vedolizumab, Takeda) and the recently licenced antibody to the p40 subunit of IL-12/23, Ustekinumab (Janssen Pharmaceuticals, Johnson and Johnson). It is best practice to

undertake a clinical assessment of disease activity using one or a number of the above mentioned modalities in a timely manner and whenever patients have symptoms (NICE, 2019).

Monitoring the patient's response to treatment, disease activity, and progression is essential, as each patient may respond differently to the prescribed treatment. For those with active fistulising CD who have not responded to conventional therapy, are intolerant of it, or have contraindications, infliximab is advised as a treatment option. Infliximab is prescribed as part of a scheduled course of therapy up to 12 months following the start of therapy or until treatment failure (including the requirement for surgery), whichever comes first. In order to determine whether continued treatment is still clinically appropriate, patients have their disease re-evaluated.

The three main surgical options for CD are bowel resection, strictureplasty, and bypass. Bowel resection with or without anastomosis is the most popular surgical procedure. However, strictureplasty has revolutionised the surgical concept of CD over the past 20 years. This is because strictureplasty does not require the removal of any part of the intestines, rather it repairs a stricture by widening the narrow area. Another option is to use a bypass, which could be external, like a stoma, or internal, with or without exclusion. Due to the possibility of developing an infected mucocele and the increased risk of cancer in the excluded segment, internal bypass is now typically avoided. It is occasionally carried out in the form of a gastroenterostomy on patients with gastroduodenal CD (Chandra & Moore, 2011).

As the assessment of disease progression and response to treatment forms an essential part of CD management, advances in diagnostic tools, medical imaging modalities, and algorithmic disease activity metrics can help to develop more robust and reliable treatment regimens for CD.

References:

Baert, F., Moortgat, L., Van Assche, G., Caenepeel, P., Vergauwe, P., De Vos, M., Stokkers, P., Hommes, D., Rutgeerts, P., Vermeire, S., & D'Haens, G. (2010). Mucosal Healing Predicts Sustained Clinical Remission in Patients With Early-Stage Crohn's Disease. *Gastroenterology*, *138*(2), 463–468. https://doi.org/10.1053/j.gastro.2009.09.056

Baumgart, D. C. (2018). The Diagnosis and Treatment of Crohn's Disease and Ulcerative Colitis. *Deutsches Aerzteblatt Online*, *106*(8), 123–133. https://doi.org/10.3238/arztebl.2009.0123

Benitez, J. M., Meuwis, M. A., Reenaers, C., Van Kemseke, C., Meunier, P., & Louis, E. (2013). Role of endoscopy, cross-sectional imaging and biomarkers in Crohn's disease monitoring. *Gut*, *62*(12), 1806–1816. https://doi.org/10.1136/gutjnl-2012-303957

Best, W. R., Becktel, J. M., Singleton, J. W., & Kern, F. (1976). Development of a Crohn's Disease Activity Index: National Cooperative Crohn's Disease Study. *Gastroenterology*, *70*(3), 439–444. https://doi.org/10.1016/S0016-5085(76)80163-1

Bjarnason, I. (2017). The use of fecal calprotectin in inflammatory bowel disease. In *Gastroenterology and Hepatology* (Vol. 13, Issue 1, pp. 53–56). Millenium Medical Publishing. /pmc/articles/PMC5390326/

Buisson, A., Joubert, A., Montoriol, P. F., Ines, D. D., Hordonneau, C., Pereira, B., Garcier, J. M., Bommelaer, G., & Petitcolin, V. (2013). Diffusion-weighted magnetic resonance imaging for detecting and assessing ileal inflammation in Crohn's disease. *Alimentary Pharmacology and Therapeutics*, *37*(5), 537–545. https://doi.org/10.1111/apt.12201

Chandra, R., & Moore, J. W. E. (2011). The Surgical Options and Management of Intestinal Crohn's Disease. In *Indian Journal of Surgery* (Vol. 73, Issue 6, pp. 432–438). Springer. https://doi.org/10.1007/s12262-011-0319-1

Connors, J. M. (2011). Crohn's disease of the stomach and duodenum. *XPharm: The Comprehensive Pharmacology Reference*, *1976*, 1–13. https://doi.org/10.1016/B978-008055232-3.60714-7

Daperno, M., D'Haens, G., Van Assche, G., Baert, F., Bulois, P., Maunoury, V., Sostegni, R., Rocca, R., Pera, A., Gevers, A., Mary, J.-Y., Colombel, J.-F., & Rutgeerts, P. (2004). Development and validation of a new, simplified endoscopic

activity score for Crohn's disease: the SES-CD. *Gastrointestinal Endoscopy*, *60*(4), 505–512. http://www.ncbi.nlm.nih.gov/pubmed/15472670

Feuerstein, J. D., & Cheifetz, A. S. (2017a). Crohn Disease: Epidemiology, Diagnosis, and Management. *Mayo Clinic Proceedings*, *92*(7), 1088–1103. https://doi.org/10.1016/j.mayocp.2017.04.010

Feuerstein, J. D., & Cheifetz, A. S. (2017b). *Crohn Disease: Epidemiology, Diagnosis, and Management*. *92*(July), 1088–1103.

Furukawa, A., Saotome, T., Yamasaki, M., Maeda, K., Nitta, N., Takahashi, M., Tsujikawa, T., Fujiyama, Y., Murata, K., & Sakamoto, T. (2007). Cross-sectional Imaging in Crohn Disease. *RadioGraphics*, *24*(3), 689–702. https://doi.org/10.1148/rg.243035120

Haas, K., Rubesova, E., & Bass, D. (2016). Role of imaging in the evaluation of inflammatory bowel disease: How much is too much? *World Journal of Radiology*, *8*(2), 124. https://doi.org/10.4329/wjr.v8.i2.124

Harvey, R. F., & Bradshaw, J. M. (1980). A simple index of Crohn's-disease activity. *Lancet (London, England)*.

Holt, D. Q., Moore, G. T., Strauss, B. J. G., Hamilton, A. L., De Cruz, P., & Kamm, M. A. (2017). Visceral adiposity predicts post-operative Crohn's disease recurrence. *Alimentary Pharmacology and Therapeutics*, *45*(9), 1255–1264. https://doi.org/10.1111/apt.14018

Guglielmo, F. F., Anupindi, S. A., Fletcher, J. G., Al-Hawary, M. M., Dillman, J. R., Grand, D. J., Bruining, D. H., Chatterji, M., Darge, K., Fidler, J. L., Gandhi, N. S., Gee, M. S., Grajo, J. R., Huang, C., Jaffe, T. A., Park, S. H., Rimola, J., Soto, J. A., Taouli, B., … Baker, M. E. (2020). Small bowel crohn disease at CT and MR enterography: Imaging atlas and glossary of terms. *Radiographics*, *40*(2), 354–375. https://doi.org/10.1148/rg.2020190091

Ilangovan, R., Burling, D., George, A., Gupta, A., Marshall, M., & Taylor, S. A. (2012). CT enterography: Review of technique and practical tips. In *British Journal of Radiology* (Vol. 85, Issue 1015, pp. 876–886). British Institute of Radiology. https://doi.org/10.1259/bjr/27973476

Jones, G. R., Lyons, M., Plevris, N., Jenkinson, P. W., Bisset, C., Burgess, C., Din, S., Fulforth, J., Henderson, P., Ho, G. T., Kirkwood, K., Noble, C., Shand, A. G., Wilson, D. C., Arnott, I. D. R., & Lees, C. W. (2019). IBD prevalence in Lothian, Scotland, derived by capture-recapture methodology. *Gut*, *68*(11), 1953–1960. https://doi.org/10.1136/gutjnl-2019-318936

Khanna, R., Zou, G., D'Haens, G., Feagan, B. G., Sandborn, W. J., Vandervoort, M. K., Rolleri, R. L., Bortey, E., Paterson, C., Forbes, W. P., & Levesque, B. G. (2015). A retrospective analysis: The development of patient reported outcome measures for the assessment of Crohn's disease activity. *Alimentary Pharmacology and Therapeutics*. https://doi.org/10.1111/apt.13001

Khoshkish, S., Arefi, K., Charmehali, M., & Vahedi, H. (2012). *Risk Factors for Postoperative Recurrence of Crohn ' s Disease*. *4*(4), 199–205.

Lamb, C. A., Kennedy, N. A., Raine, T., Hendy, P. A., Smith, P. J., Limdi, J. K., Hayee, B., Lomer, M. C. E., Parkes, G. C., Selinger, C., Barrett, K. J., Davies, R. J., Bennett, C., Gittens, S., Dunlop, M. G., Faiz, O., Fraser, A., Garrick, V., Johnston, P. D., … Hawthorne, A. B. (2019). British Society of Gastroenterology consensus guidelines on the management of inflammatory bowel disease in adults. In *Gut* (Vol. 68, Issue Suppl 3, pp. s1–s106). Gut. https://doi.org/10.1136/gutjnl-2019-318484

Fvasconcellos, S. (2006). *File:Patterns of Crohn's Disease.svg - Wikimedia Commons*. https://commons.wikimedia.org/wiki/File:Patterns_of_Crohn%27s_Disease.svg#filelinks

Maaser, C., Sturm, A., Vavricka, S. R., Kucharzik, T., Fiorino, G., Annese, V., Calabrese, E., Baumgart, D. C., Bettenworth, D., Borralho Nunes, P., Burisch, J., Castiglione, F., Eliakim, R., Ellul, P., González-Lama, Y., Gordon, H., Halligan, S., Katsanos, K., Kopylov, U., … Stoker, J. (2019). ECCO-ESGAR Guideline for Diagnostic Assessment in IBD Part 1: Initial diagnosis, monitoring of known IBD, detection of complications. *Journal of Crohn's and Colitis*, *13*(2), 144–164. https://doi.org/10.1093/ecco-jcc/jjy113

Magro, F., Rodrigues-Pinto, E., Santos-Antunes, J., Vilas-Boas, F., Lopes, S., Nunes, A., Camila-Dias, C., & Macedo, G. (2014). High C-reactive protein in Crohn's disease patients predicts nonresponse to infliximab treatment. *Journal of Crohn's and Colitis*. https://doi.org/10.1016/j.crohns.2013.07.005

Makanyanga, J. C., Pendsé, D., Dikaios, N., Bloom, S., McCartney, S., Helbren, E., Atkins, E., Cuthbertson, T., Punwani, S., Forbes, A., Halligan, S., & Taylor, S. A. (2014). Evaluation of Crohn's disease activity: Initial validation of a magnetic resonance enterography global score (MEGS) against faecal calprotectin. *European Radiology*, *24*(2), 277–287. https://doi.org/10.1007/s00330-013-3010-z

Mao, R., Gao, X., Zhu, Z. H., Feng, S. T., Chen, B. L., He, Y., Cui, Y., Li, Z. P., Hu, P. J., & Chen, M. H. (2013). CT Enterography in evaluating postoperative

recurrence of crohn's disease after ileocolic resection: Complementary role to endoscopy. *Inflammatory Bowel Diseases*, *19*(5), 977–982. https://doi.org/10.1097/MIB.0b013e318280758c

Mary, J. Y., & Modigliani, R. (1989). Development and validation of an endoscopic index of the severity for Crohn's disease: a prospective multicentre study. Groupe d'Etudes Thérapeutiques des Affections Inflammatoires du Tube Digestif (GETAID). *Gut*, *30*(7), 983–989. http://www.ncbi.nlm.nih.gov/pubmed/2668130%0Ahttp://www.pubmedcentral.nih.gov/articlerender.fcgi?artid=PMC1434265

Mohamed, A. M., Amin, S. K., El-Shinnawy, M. A., Elfouly, A., & Baki, A. H. (2012). Role of CT enterography in assessment of Crohn's disease activity: Correlation with histopathologic diagnosis. *Egyptian Journal of Radiology and Nuclear Medicine*, *43*(3), 353–359. https://doi.org/10.1016/j.ejrnm.2012.05.005

Crohn's disease: management. NICE guideline NG129. National Institute for Health and Care Excellence. 2019.https://www.nice.org.uk/guidance/ng129 (accessed Mar 2023).

Puylaert, C. A. J., Tielbeek, J. A. W., Bipat, S., & Stoker, J. (2015). Grading of Crohn's disease activity using CT, MRI, US and scintigraphy: a meta-analysis. *European Radiology*, *25*(11), 3295–3313. https://doi.org/10.1007/s00330-015-3737-9

Rhen, T., & Cidlowski, J. A. (2005). Antiinflammatory Action of Glucocorticoids — New Mechanisms for Old Drugs. *New England Journal of Medicine*, *353*(16), 1711–1723. https://doi.org/10.1056/nejmra050541

Rimola, J., Ordás, I., Rodriguez, S., García-Bosch, O., Aceituno, M., Llach, J., Ayuso, C., Ricart, E., & Panés, J. (2011). Magnetic resonance imaging for evaluation of Crohn's disease: Validation of parameters of severity and quantitative index of activity. *Inflammatory Bowel Diseases*, *17*(8), 1759–1768. https://doi.org/10.1002/ibd.21551

Røseth, A. G., Aadland, E., & Grzyb, K. (2004). Normalization of faecal calprotectin: a predictor of mucosal healing in patients with inflammatory bowel disease. *Scandinavian Journal of Gastroenterology*. https://doi.org/10.1080/00365520410007971

Rozendorn, N., Amitai, M. M., Eliakim, R. A., Kopylov, U., & Klang, E. (2018). A review of magnetic resonance enterography-based indices for quantification of Crohn's disease inflammation. In *Therapeutic Advances in Gastroenterology*. https://doi.org/10.1177/1756284818765956

Saibeni, S., Rondonotti, E., Iozzelli, A., Spina, L., Tontini, G. E., Cavallaro, F., Ciscato, C., De Franchis, R., Sardanelli, F., & Vecchi, M. (2007). Imaging of the small bowel in Crohn's disease: A review of old and new techniques. In *World Journal of Gastroenterology* (Vol. 13, Issue 24, pp. 3279–3287). Baishideng Publishing Group Inc. https://doi.org/10.3748/wjg.v13.i24.3279

Schnitzler, F., Fidder, H., Ferrante, M., Noman, M., Arijs, I., Van Assche, G., Hoffman, I., Van Steen, K., Vermeire, S., & Rutgeerts, P. (2009). Mucosal healing predicts long-term outcome of maintenance therapy with infliximab in Crohn's disease. *Inflammatory Bowel Diseases*, *15*(9), 1295–1301. https://doi.org/10.1002/ibd.20927

Shanahan, F. (2002). *Crohn ' s disease*. *359*.

Sipponen, T., Nuutinen, H., Turunen, U., & Färkkilä, M. (2010). Endoscopic evaluation of Crohn's disease activity: Comparison of the CDEIS and the SES-CD. *Inflammatory Bowel Diseases*, *16*(12), 2131–2136. https://doi.org/10.1002/ibd.21300

Steward, M. J., Punwani, S., Proctor, I., Adjei-Gyamfi, Y., Chatterjee, F., Bloom, S., Novelli, M., Halligan, S., Rodriguez-Justo, M., & Taylor, S. A. (2012). Non-perforating small bowel Crohn's disease assessed by MRI enterography: Derivation and histopathological validation of an MR-based activity index. *European Journal of Radiology*, *81*(9), 2080–2088. https://doi.org/10.1016/j.ejrad.2011.07.013

Sturm, A., Maaser, C., Calabrese, E., Annese, V., Fiorino, G., Kucharzik, T., Vavricka, S. R., Verstockt, B., Van Rheenen, P., Tolan, D., Taylor, S. A., Rimola, J., Rieder, F., Limdi, J. K., Laghi, A., Krustins, E., Kotze, P. G., Kopylov, U., Katsanos, K., … Stoker, J. (2019). Ecco-esgar guideline for diagnostic assessment in ibd part 2: Ibd scores and general principles and technical aspects. *Journal of Crohn's and Colitis*, *13*(3), 273-284E. https://doi.org/10.1093/ecco-jcc/jjy114

Taylor, S. A., Mallett, S., Bhatnagar, G., Baldwin-Cleland, R., Bloom, S., Gupta, A., Hamlin, P. J., Hart, A. L., Higginson, A., Jacobs, I., McCartney, S., Miles, A., Murray, C. D., Plumb, A. A., Pollok, R. C., Punwani, S., Quinn, L., Rodriguez-Justo, M., Shabir, Z., … Morris, S. (2018). Diagnostic accuracy of magnetic resonance enterography and small bowel ultrasound for the extent and activity of newly diagnosed and relapsed Crohn's disease (METRIC): a multicentre trial. *The Lancet Gastroenterology and Hepatology*. https://doi.org/10.1016/S2468-1253(18)30161-4

Travis, S. P. L., Stange, E. F., Lémann, M., Öresland, T., Chowers, Y., Forbes, A.,

D'Haens, G., Kitis, G., Cortot, A., Prantera, C., Marteau, P., Colombel, J. F., Gionchetti, P., Bouhnik, Y., Tiret, E., Kroesen, J., Starlinger, M., & Mortensen, N. J. M. M. (2006). European evidence based consensus on the diagnosis and management of Crohn's disease: Current management. *Gut*, *55*(SUPPL. 1), 16–35. https://doi.org/10.1136/gut.2005.081950b

US FDA. (2017). *FDA Drug Safety Communication: FDA identifies no harmful effects to date with brain retention of gadolinium-based contrast agents for MRIs; review to continue*. U.S. Department of Health and Human Services.

Vermeire, S., Van Assche, G., & Rutgeerts, P. (2004). C-Reactive Protein as a Marker for Inflammatory Bowel Disease. *Inflammatory Bowel Diseases*, *10*(5), 661–665. https://doi.org/10.1097/00054725-200409000-00026

Vermeire, S., Van Assche, G., & Rutgeerts, P. (2006). Laboratory markers in IBD: Useful, magic, or unnecessary toys? In *Gut*. https://doi.org/10.1136/gut.2005.069476

Zittan, E., Kelly, O. B., Gralnek, I. M., Silverberg, M. S., & Hillary Steinhart, A. (2018). Fecal calprotectin correlates with active colonic inflammatory bowel disease but not with small intestinal Crohn's disease activity. *JGH Open*, *2*(5), 201–206. https://doi.org/10.1002/jgh3.12068

4 Visceral Fat Hypertrophy and Abdominal Fat Segmentation Algorithm

4.1 Visceral Fat Hypertrophy

The mesentery is defined as a double layer of the peritoneal membrane that supports the small intestine. It is of a fan shape, and its shorter edge is attached to the back wall of the abdomen while the small intestine lies within its longer boundary (Healy & Reznek, 2000).

Visceral fat hypertrophy, also known as fat wrapping or creeping fat, refers to the extension and thickening of mesenteric fat to partially, or in some cases fully, cover the small or large intestine. Figure 4.1 illustrates this phenomenon. Crohn BB first described it in the original publication as a sign of CD (Crohn et al., 1932). The visceral hypertrophy of mesenteric fat surrounds the inflamed segments of the gut covering more than 50% of the intestinal circumference, which is of significant importance and a common and specific feature of CD. Fat wrapping has been found to correlate well with fibrosis, muscular hypertrophy, transmural inflammation, and stricture formation (Peyrin-Biroulet et al., 2007). For this reason, fat wrapping became a radiological hallmark for CD and has been used by clinicians to identify sites of inflammation (Sheehan et al., 1992).

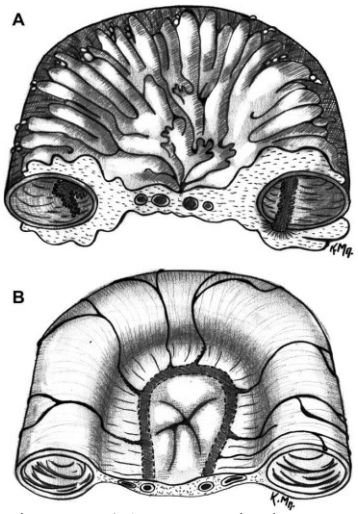

Figure 4.1: Intestinal cross-sections (A) showing fat wrapping in CD and (B) normal comparison (Fink, Karagiannides,et al., 2012)

Abdominal fat is mainly classified into Subcutaneous Adipose Tissue (SAT) and Visceral Adipose Tissue (VAT). As a result of visceral fat hypertrophy, CD patients tend to have higher ratios of VAT to SAT (Cravo et al., 2017).

Adipocytes are the main cellular components of white adipose tissue (WAT). While their primary function is to control energy balance by storing and redirecting triacylglycerol, they also play vital roles as endocrine and paracrine organs. When

adipocytes accumulate in large numbers, they form adipose tissue (Ali et al., 2013). Adipocytes are generally divided into brown, beige, and white cells covering diverse intermediate forms. White fat cells represent the main type in adipose tissues in adults (Huh et al., 2014).

Interestingly, the absolute number of adipocyte cells is bound by genetic factors and tends to remain relatively stable after the end of the growth phase (Rosen & Spiegelman, 2014). In the case of obesity, the enlargement of adipocytes occurs, causing the expansion of VAT in the abdomen, which can lead to hormonal alteration and inflammation. However, histological evidence shows that in the case of visceral fat hypertrophy, the number of adipose cells increases around the inflamed areas and the cells become smaller in size and higher in density (Peyrin-Biroulet et al., 2007) (Shen et al., 2019). Figure 4.2 shows the differences in density of adipose cells in VAT of CD patients compared to that of healthy controls. The humoral and cellular alterations within creeping fat tissue differ from the cellular alterations observed in the case of obesity (Kredel & Siegmund, 2014).

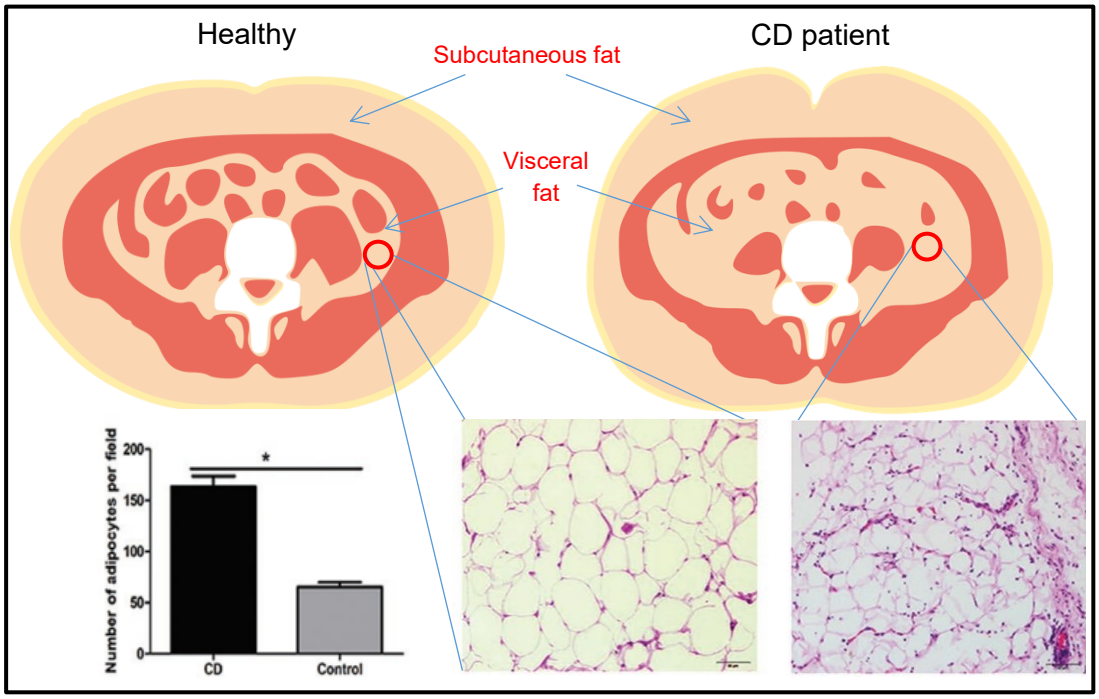

Figure 4.2: shows the differences in visceral fat concentrations on MRI and histological examinations (Shen et al., 2019).

The exact cause of fat wrapping in CD has been widely debated. Recent studies suggest that fat wrapping is triggered by inflammatory stimuli and bacterial translocation. While clinicians used to consider fat wrapping as an outcome of the disease pathology changes, research indicates that it may be a contributing factor to inflammation as adipocytes in CD patients are found to be the main source of cellular pro-inflammatory cytokines (TNFα), interleukin-6 and C-reactive protein (CRP) (Peyrin-Biroulet et al., 2007) (Kredel & Siegmund, 2014). A study comparing conventional ileocolic resections with intestinal resections, including excision of the mesentery, found that the inclusion of the mesentery in ileocolic resection for CD is associated with a reduction in disease recurrence (Coffey et al., 2018) which indicates that the mesenteric fat in CD patients is contributing towards CD recurrence after surgery. A similar study in 2021 investigated the association between resection of the mesentery and postoperative outcomes in patients with Crohn's colitis undergoing colorectal surgery. Their results showed that the inclusion of the mesentery in colorectal resection surgery is associated with improved long-term outcomes (Zhu et al., 2021).

In clinical practice, fat wrapping is often used to further confirm a diagnosis of CD (Golder, 2009), and surgeons use it to outline the extent of active disease in the bowels (Sheehan et al., 1992). However, the complexity of the abdominal visceral fat structure makes it difficult to objectively quantify it as a disease activity metric. Hence, most research investigating the impact of fat wrapping and its utility as a disease activity biomarker consider it as a binary measure where they confirm or reject the presence of fat wrapping in CD patients. This is most evident in ultrasound, as it has been used for many years as a tool for identifying fat wrapping due to its wide availability and sensitivity to tissue density. Kucharzik et al. used ultrasound to investigate many CD activity biomarkers, including fat hypertrophy, on 134 CD patients at baseline and after 3, 6, and 12 months of treatment. At baseline, 63 patients were identified to have mesenteric fat hypertrophy on ultrasound scans. After 12 months of treatment, the number of patients with fat wrapping decreased gradually throughout the study reaching 24 patients (Kucharzik et al., 2017). Maconi et al. also investigated the presence of fat wrapping on 185 CD patients using ultrasound. Out of the 185 patients, mesenteric fat hypertrophy was detected in 88 (47.6%) CD patients. Their results

showed that the presence of fat hypertrophy significantly correlated with established disease measures such as CDAI, CRP and erythrocyte sedimentation rate (ESR) (Maconi et al., 2008).

Maconi et al.'s criteria for the presence of fat hypertrophy on ultrasound was a hyperechoic halo surrounding the bowel wall with a thickness larger than 5 mm as shown in Figure 4.3. Such a criterion was chosen arbitrarily based on their observations. This demonstrates some of the main drawbacks of using ultrasound to detect fat hypertrophy in CD patients. The lack of established criteria in literature and clinical practice for fat wrapping in ultrasound, along with the subjectivity of ultrasonic imaging techniques, makes it difficult to use ultrasound as an objective quantification method for fat wrapping in CD.

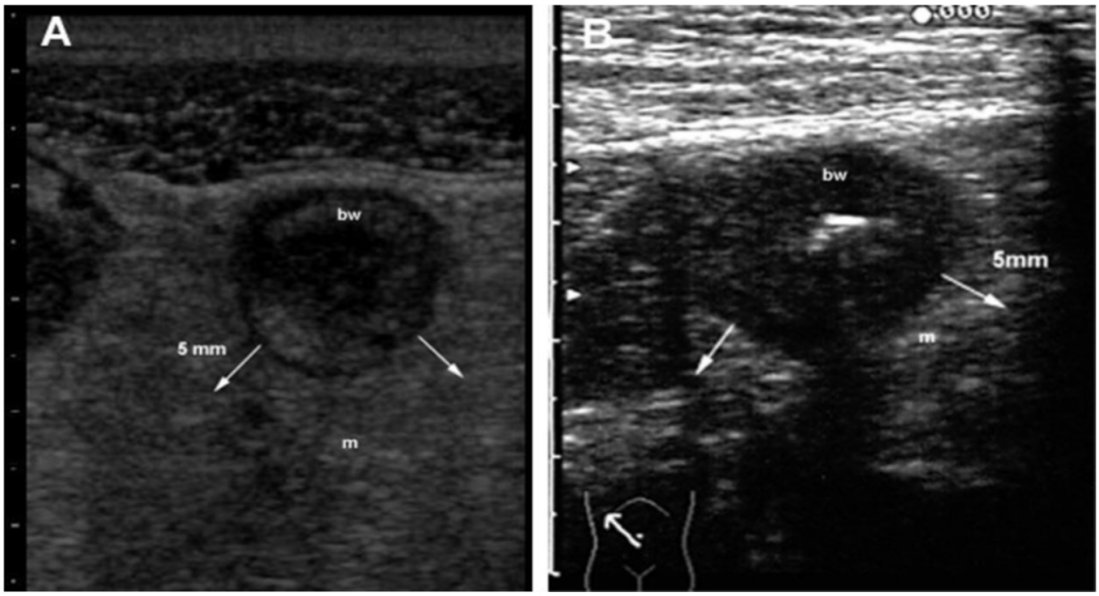

Figure 4.3: Ultrasonographic images of (A) severe mesenteric fat hypertrophy (m) assessed as a hyperechoic halo surrounding bowel wall (bw) in transverse section, and (B) mild mesenteric fat hypertrophy (m) in CD patients (Maconi et al., 2008).

CT is considered the ideal modality for studying fat quantification due to its ability to calculate tissue attenuation coefficients. This results in an accurate differentiation between muscles and fat tissue (Rossner et al., 1990)

Several studies conducted using CT indicated a positive correlation between VAT area measurements and various CD complications. The exact measurements of attenuation coefficients for muscles and fat can vary. Cravo et al. found that the Hounsfield unit

(HU) for muscles ranges from -29 to 150; VAT from -150 to -50 HU, and SAT ranges from -190 to -30 HU. By using these different attenuation coefficients, they were able to calculate VAT and SAT areas at the level of the third lumbar vertebrae (L3). They found a higher correlation between increased VAT/SAT ratios in patients with inflammation in the colon than patients with inflammation at the terminal ileum (Cravo et al., 2017).

Li et al. used CT to calculate the ratio of VAT area to SAT area in CD patients at the level of the umbilicus, with the patient in the supine position. Their research showed that VAT areas and mesenteric fat index (MFI) (defined as the ratio of the VAT area to SAT area) measurements correlated well with a postoperative endoscopic recurrence at six months after surgery in 48 CD patients (Li et al., 2015). Figure 4.4 shows Li et al.'s results. Another study found that patients with visceral obesity had a significantly longer operative time ($P = 0.012$), more blood loss ($P = 0.019$), longer bowel resection length ($P = 0.003$), postoperative ileus ($P = 0.039$) and a greater number of complications overall thus implying a possible relationship between visceral fat hypertrophy and disease burden.

While the typical modality for single-slice body fat measurements is CT, recent advances in MRI fat and water separation techniques proved that MRI could be a reliable modality for imaging fat (Klopfenstein et al., 2012). MRI is considered to be the preferred method for repeated volumetric measurements of abdominal fat quantity due to the exposure to ionizing radiation in CT scans (Seidell et al., 1990). When imaging a large field of view such as the abdomen, the Dixon method offers a better and more accurate water and fat separation compared to other sequences due to its robustness and SNR efficiency (Seidell et al., 1990).

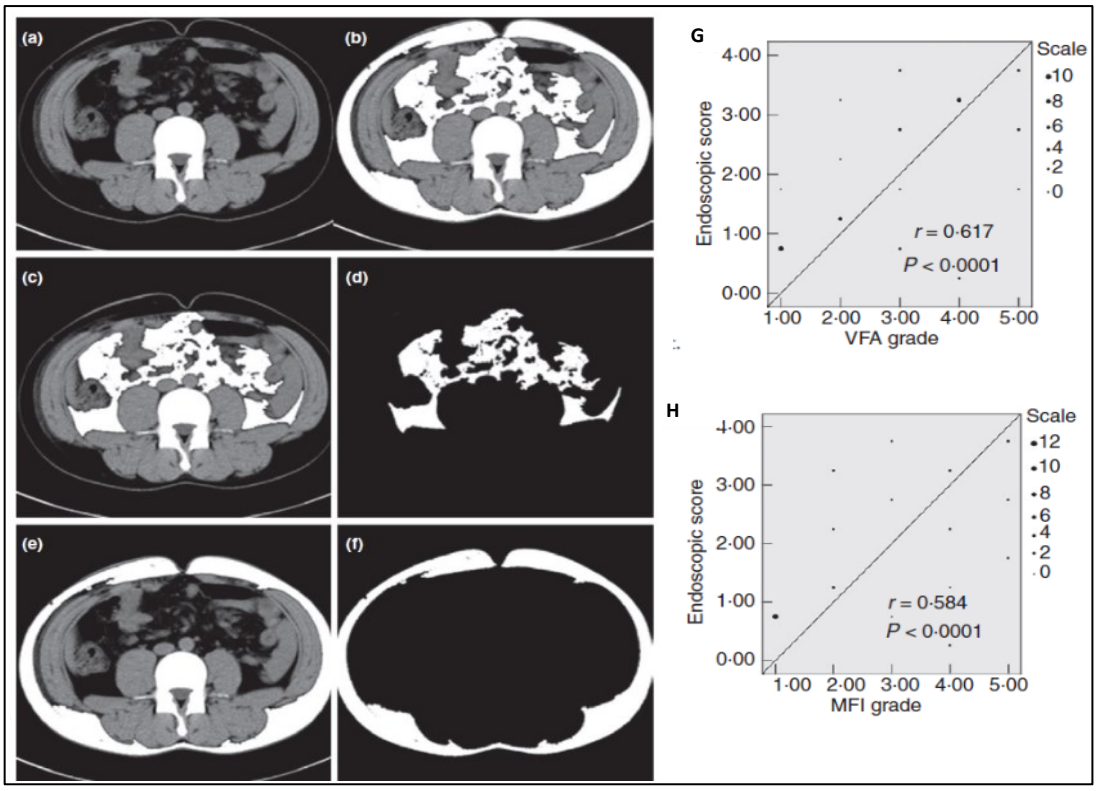

Figure 4.4: CT measurement of the visceral fat area (VFA) and subcutaneous fat area (SFA) of a patient with CD. (a) Original transverse CT imaging at the level of the umbilicus. (b) Total fat tissue was extracted from the original image. (c, d) VAT extracted from the original image. (e, f) SAT extracted from the original image. Correlation between the visceral fat area (VFA) (G), the mesenteric fat index (MFI) (H) and Rutgeerts scores in patients with available postoperative endoscopy results. r, Spearman's correlation coefficient (Li et al., 2015).

4.2 Abdominal Fat Segmentation in MRI

As previously mentioned, in CT, the differences between VAT and SAT fat can be detected using differences in attenuation coefficients between the tissues; however, standard MRI fat imaging techniques do not offer the same level of sensitivity to different types of fat tissue density. Therefore, to assess abdominal fat volumes in MRI, a post-processing segmentation method is required to differentiate between VAT and SAT. Due to this issue, some studies resorted to visual assessments by radiologists to indicate the existence of fat wrapping on MRE scans (Althoff et al., 2019) and manual segmentation for quantification of VAT and SAT areas (Z. Zhou et al., 2021).

In Desreumaux et al.'s research, the intra-abdominal fat accumulation was quantified using a turbo-spin-echo sequence in patients with CD and healthy controls. In

transverse 6-mm-thick slices around the umbilicus region, areas of intra-abdominal and abdominal SAT tissues were estimated. A total of 31 abdominal fat and intra-abdominal fat areas were quantified by manually outlining the total and intra-abdominal fat areas. The abdominal SAT area was calculated by subtracting the intra-abdominal fat area from the total fat tissue. Their results showed that while CD patients and HVs had similar total abdominal VAT and SAT fat areas, CD patients had a significantly higher ratio of intra-abdominal to total abdominal fat compared to HVs (0.34 ± 0.11 vs 0.22 ± 0.07; $P= 0.012$) (Desreumaux et al., 1999).

In order to study the effects of fat wrapping on VAT, a segmentation method is needed to separate VAT and SAT fat in the abdomen. Traditionally, manual segmentation is used where a trained researcher draws lines separating VAT from the SAT fat on the axial plane (Holt et al., 2017) (Kullberg et al., 2009). Hence, researchers tend to use semi-automated segmentation methods such as active contouring (Benfield et al., 2008) and magic wand selection (Gronemeyer et al., 2000) to accelerate the segmentation process. However, both manual and semi-automated segmentation methods are time-consuming and prone to biases by the operator. Some researchers developed fully automated segmentation algorithms based on fuzzy clustering (A. Zhou et al., 2011), graph-cuts (Christensen et al., 2017) and machine learning (Estrada et al., 2020). Many of these algorithms are bound to a specific region in the abdomen (Kullberg et al., 2007) or require access to high-performance computers and large training databases, such as the case for machine learning approaches.

4.3 Aims and Objectives

In order to establish an objective measurement of abdominal fat volumes, an automated segmentation algorithm was developed on MATLAB to calculate VAT and SAT volumes in axial MRI abdominal scans.

Aim: To develop a segmentation algorithm to measure VAT and SAT volumes on 2-point Dixon MRI scans and validate its performance against manual segmentation.

Objectives:

- Develop a fast and easy to use segmentation algorithm that can differentiate between VAT and SAT accurately.
- Compare the results generated by algorithm with manually segmented images.

4.4 Methods

4.4.1 Automated Abdominal Fat Segmentation Algorithm

In order to employ image analysis techniques on MRI images to study abdominal fat, one of the most critical issues that needs to be resolved is distinguishing between VAT and SAT fat automatically. Once an automated and reliable algorithm has been developed to solve this problem, the rest of the image processing challenges are easier to solve. For this research, an algorithm has been created that utilizes a combination of adaptive grayscale thresholding, gaussian filters and morphological operations to find the inner abdominal area, which is then used to differentiate between VAT and SAT fat. Figure 4.5 shows a step-by-step diagram explaining the fat segmentation algorithm process.

4.4.1.1 Selection of the Slices to be Used

When the user runs the code, an interactive pop-up window will appear, showing the images in multiple orientations to aid the user in identifying the axial slices included in the quantification. A second window then asks the user to input the analysis's start and ending axial slice numbers. For this study, a region between the top of the hip joint and second lumbar vertebrae (L2) was selected for quantification across all subjects. Due to the height and position variations between each subject, this region's size and location can vary; hence, it was identified visually using the vertebral column as a reference. The imported images are converted into a black and white binary image using Otsu's adaptive thresholding method, which chooses a threshold that minimizes the interclass variance of the thresholded black and white pixels (Otsu, 1979).

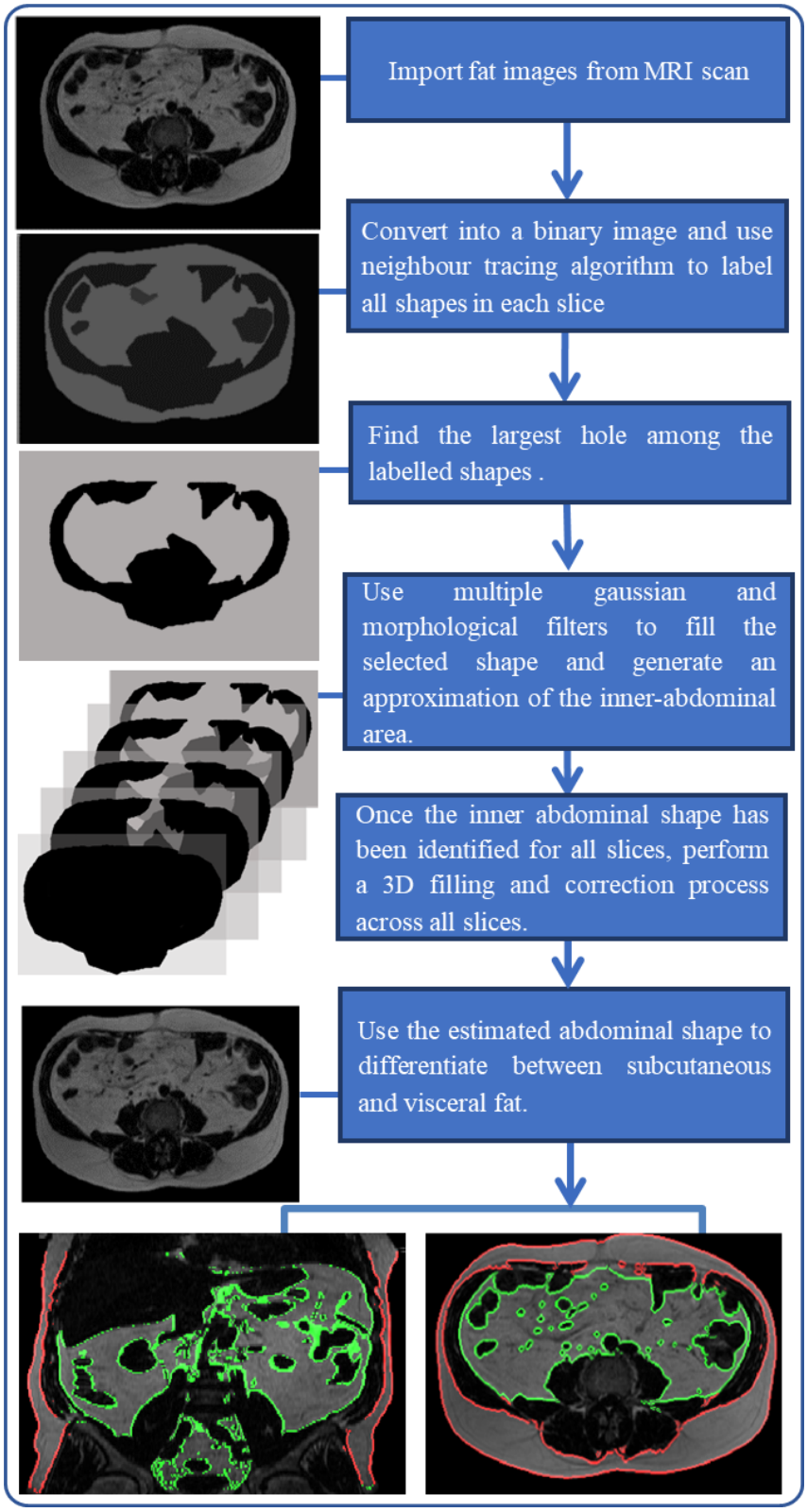

Figure 4.5: A diagram explaining the fat segmentation algorithm in steps.

4.4.1.2 Line Extraction Function

The algorithm loops through each axial slice utilizing a variation of MATLAB's "bwboundaries" function which is based on Moore-Neighbor tracing algorithm modified by Jacob's stopping criteria (*MATLAB Bwboundaries - MathWorks*, n.d.) to identify and label each connected shape and hole (zero pixels surrounded by one pixels) on the binary image. This is shown as step 2 in Figure 4.5. As the fat on the binary axial image appears as one connected bright shape, the function identifies the muscles as a large "hole" in that shape, which consists of muscles and organs. This is shown as step 3 in Figure 4.5. After this hole has been identified, the algorithm runs multiple gaussian filters and morphological operations filling the mid-section of the shape with each step. At the end of this process, the resulting shape closely resembles the inner-abdominal area. This is shown as step 4 in Figure 4.5. Once all the axial slices have been processed, the algorithm performs multiple correction steps on the newly formed 3D inner-abdominal structure by filling all missing gaps in the 3D inner-abdominal volume adjusting the shapes in each slice to closely resemble the shape in the slice before and after it. This process can even produce new axial inner-abdominal shapes to fill the missing slices if the first process failed to produce one.

4.4.1.3 Segmenting Visceral Fat and Subcutaneous Fat

The final 3D inter-abdominal shape is then used to differentiate between the SAT and VAT fat on the original image. The segmented images are then viewed on the software to evaluate the algorithm's performance on the coronal, sagittal, and axial planes. In the software viewing window, the VAT is outlined in green, and the SAT fat is outlined in red. This is shown as the final step in Figure 4.5.

4.4.2 Dixon Images Segmentation Validation

To validate the segmentation algorithm performance, 10 manually segmented Dixon images acquired from a previous study (Murray et al., 2019) were used as reference. Segmented images using the algorithm were compared to their corresponding manually segmented images using the Sørensen–Dice coefficient, which calculates the

similarities between two data sets (automated and manual segmentation) (Zou et al., 2004).

The validation scans were manually segmented into three regions, SAT region, VAT region and intramuscular & Spinal Tissue region (IMST). However, the algorithm only segments two regions, SAT and VAT which includes spinal and intramuscular fat as shown in Figure 4.6 A. While the algorithm performs multiple filtration steps to remove some of the spinal and intra-muscular fat, they are generally characterized as part of the VAT region. To evaluate the algorithm's performance, fat tissues characterised as VAT in the algorithm segmentation was compared with fat tissue characterized as VAT in manual masks and it was also compared to the sum of the fat tissues from the VAT+IMST regions as the sum of these two masks generate a closer form to the intended segmentation as shown in Figure 4.6 B.

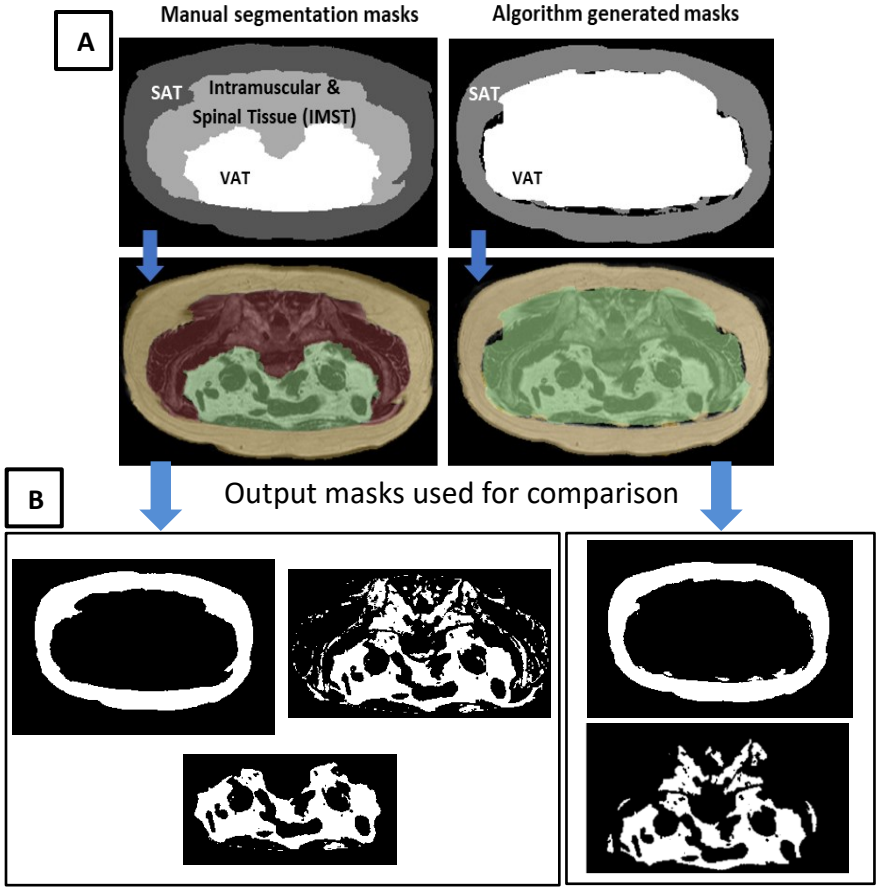

Figure 4.6: Segmentation masks generated from manual segmentation compared to algorithm generated masks.

4.4.3 Statistical analysis

Shapiro-Wilk normality test was conducted on both groups to test the null hypothesis that the data has an abnormal distribution.

Statistical analysis with unpaired, two-tailed t-tests were conducted, and differences were considered significant when the p-value was ≤ 0.05. All absolute values are presented as mean ± SD.

Linear regression and Pearson's correlation coefficient (r) were used to calculate the correlation between fat volumes calculated using the automated algorithm and manual segmentation.

4.5 Results

A total of 10 manually segmented Dixon images (BMI=29.6±4.7 kg/m^2) were used for evaluating the performance of the automated segmentation algorithm. Table 4.1 shows the segmentation validation results using Dice coefficient and correlation R values comparing fat volumes and ratios measured using automated and manual segmentation. Figure 4.7 shows VAT and SAT volumes calculated using the automated segmentation algorithm plotted against manually segmented SAT and VAT using the VAT manual mask. Table 4.1 show the performance of the segmentation algorithm in more detail.

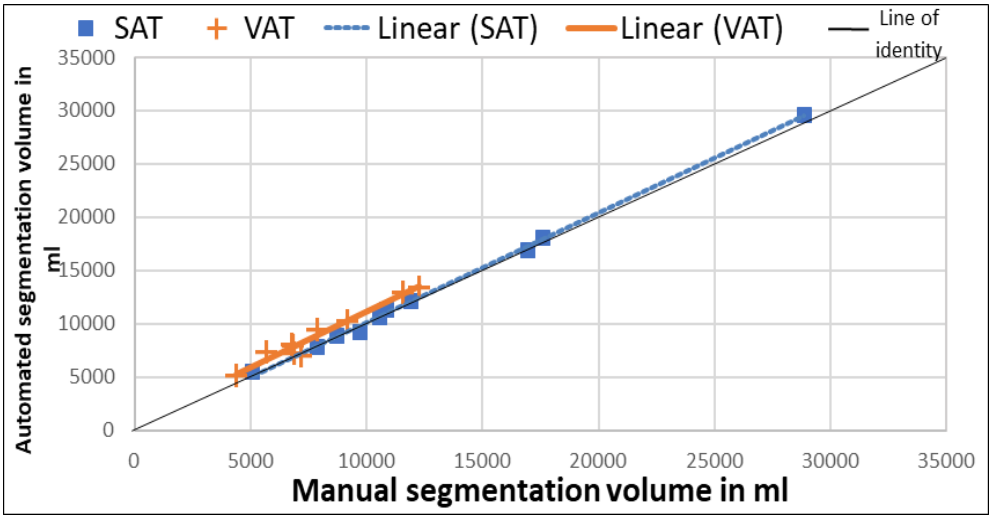

Figure 4.7: Plot diagram showing the correlation between fat volumes calculated using automated and manual segmentation.

For SAT, automated segmentation highly correlated with manual segmentation with a Pearson's correlation coefficient of 0.99; p>0.001 and a mean Dice coefficient of 0.95±0.022. When comparing the VAT algorithm segmentation with the manual VAT+IMST mask segmentation, the results show an r value of 0.98 and a Dice coefficient of 0.90±0.03 compared to 0.85±0.034 when only the manual VAT mask was used as a reference as shown in Figure 4.8. While using different manual segmentation masks as a reference for VAT resulted in different dice coefficients, both manual masks resulted in a high correlation value (r= 0.98).

Table 4.1: Segmentation algorithm performance validated against manual segmentation

Masks	VAT	VAT+IMST	SAT	VAT/TAT
Mean Manual Data (ml)	7860±2481	10096±2788	12816±6810	0.4±0.11
Range (ml)	4378-12251	6149-14786	5086-28860	0.24-0.57
Mean Auto Data (ml)	8903±2651		13038±6985	0.426±0.1
Range (ml)	5146-13400		5514-29590	0.27-0.59
Correlation (r)	0.98*	0.98*	0.99*	0.99*
Mean Dice Co-efficient	0.85±0.034	0.90±0.03	0.95±0.022	————

* p-value<0.001

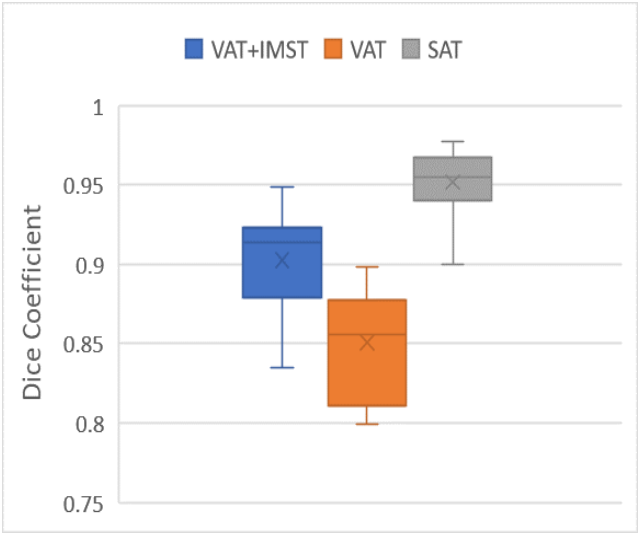

Figure 4.8: Box plot showing the Dice coefficient values for VAT, SAT and VAT+IMST areas.

The average algorithm processing time is 60 seconds on a machine with 2.6 GHz Intel i7-6700HQ CPU processor and 16.0 GB RAM.

4.6 Discussion

It is clear from Figure 4.7 that for the calculations of both VAT and SAT volumes the automated segmentation algorithm were very close to those calculated by the manual segmentation. The SAT trendline sits on top of the line of identity (the x=y line). However, the VAT trendline sits slightly above it. This indicates that the results from the automated algorithm were slightly higher than those calculated manually. This was to be expected as the automated algorithm results were compared to the VAT manual mask not the VAT+IMST mask.

Looking at Table 4.1, the automated segmentation algorithm performed very well compared to manual segmentation with r values of above 0.98 overall and an average dice coefficient of 0.95±0.022 for SAT and 0.9±0.034 for VAT. This allows for a fast and objective measurements of abdominal fat volumes in MRI.

While the algorithm demonstrated a high correlation with manual segmentation, removing the intramuscular and spinal fat from the VAT volume was not taken into account which explains the lower dice coefficient values for VAT segmentation when compared with manual VAT mask segmentation.

The manual segmentation relies on identifying the greyscale threshold value visually for each scan. However, the algorithm uses adaptive Otsu's automated thresholding method (Otsu, 1979). This introduces further discrepancies between the automated and manual segmentation.

4.7 Conclusion

The developed algorithm offers a fast and objective method to measure abdominal fat volumes. The algorithm was designed with a simple structure avoiding the need for high performance computers or long processing time. This allows for measuring a larger abdominal area and simplifying the measurement of abdominal fat in MRI for researchers and clinicians.

References

Ali, A. T., Hochfeld, W. E., Myburgh, R., & Pepper, M. S. (2013). Adipocyte and adipogenesis. *European Journal of Cell Biology*, *92*(6–7), 229–236. https://doi.org/10.1016/j.ejcb.2013.06.001

Althoff, P., Schmiegel, W., Lang, G., Nicolas, V., & Brechmann, T. (2019). Creeping Fat Assessed by Small Bowel MRI Is Linked to Bowel Damage and Abdominal Surgery in Crohn's Disease. *Digestive Diseases and Sciences*, *64*(1), 204–212. https://doi.org/10.1007/s10620-018-5303-1

Benfield, L. L., Fox, K. R., Peters, D. M., Blake, H., Rogers, I., Grant, C., & Ness, A. (2008). Magnetic resonance imaging of abdominal adiposity in a large cohort of British children. *International Journal of Obesity*, *32*(1), 91–99. https://doi.org/10.1038/sj.ijo.0803780

Bredella, M. A., Ghomi, R. H., Thomas, B. J., Torriani, M., Brick, D. J., Gerweck, A. V., Misra, M., Klibanski, A., & Miller, K. K. (2010). Comparison of DXA and CT in the assessment of body composition in premenopausal women with obesity and anorexia nervosa. *Obesity*, *18*(11), 2227–2233. https://doi.org/10.1038/oby.2010.5

Christensen, A. N., Larsen, C. T., Mandrup, C. M., Petersen, M. B., Larsen, R., Conradsen, K., & Dahl, V. A. (2017). Automatic segmentation of abdominal fat in mri-scans, using graph-cuts and image derived energies. *Lecture Notes in Computer Science (Including Subseries Lecture Notes in Artificial Intelligence and Lecture Notes in Bioinformatics)*, *10270 LNCS*, 109–120. https://doi.org/10.1007/978-3-319-59129-2_10

Coffey, C. J., Kiernan, M. G., Sahebally, S. M., Jarrar, A., Burke, J. P., Kiely, P. A., Shen, B., Waldron, D., Peirce, C., Moloney, M., Skelly, M., Tibbitts, P., Hidayat, H., Faul, P. N., Healy, V., O'Leary, P. D., Walsh, L. G., Dockery, P., O'Connell, R. P., … Dunne, C. P. (2018). Inclusion of the mesentery in ileocolic resection for Crohn's disease is associated with reduced surgical recurrence. *Journal of Crohn's and Colitis*, *12*(10), 1139–1150. https://doi.org/10.1093/ecco-jcc/jjx187

Cravo, M. L., Velho, S., Torres, J., Costa Santos, M. P., Palmela, C., Cruz, R., Strecht, J., Maio, R., & Baracos, V. (2017). Lower skeletal muscle attenuation and high visceral fat index are associated with complicated disease in patients with Crohn's disease: An exploratory study. *Clinical Nutrition ESPEN*, *21*, 79–85. https://doi.org/10.1016/j.clnesp.2017.04.005

Crohn, B. B., Ginzburg, L., & Oppenheimer, G. D. (1932). REGIONAL ILEITIS: A PATHOLOGIC AND CLINICAL ENTITY. *Journal of the American Medical Association*, *99*(16), 1323–1329. https://doi.org/10.1001/JAMA.1932.02740680019005

Desreumaux, P., Ernst, O., Geboes, K., Gambiez, L., Berrebi, D., Muller-Alouf, H., Hafraoui, S., Emilie, D., Ectors, N., Peuchmaur, M., Cortot, A., Capeon, M.,

Auwerx, J., & Colombel, J. F. (1999). Inflammatory alterations in mesenteric adipose tissue in Crohn's disease. *Gastroenterology*, *117*(1), 73–81. https://doi.org/10.1016/S0016-5085(99)70552-4

Estrada, S., Lu, R., Conjeti, S., Orozco-Ruiz, X., Panos-Willuhn, J., Breteler, M. M. B., & Reuter, M. (2020). FatSegNet: A fully automated deep learning pipeline for adipose tissue segmentation on abdominal dixon MRI. *Magnetic Resonance in Medicine*, *83*(4), 1471–1483. https://doi.org/10.1002/mrm.28022

Fink, C., Karagiannides, I., Bakirtzi, K., & Pothoulakis, C. (2012). Adipose tissue and inflammatory bowel disease pathogenesis. *Inflammatory Bowel Diseases*, *18*(8), 1550–1557. https://doi.org/10.1002/ibd.22893

Golder, W. A. (2009). The "creeping fat sign" - Really diagnostic for Crohn's disease? In *International Journal of Colorectal Disease* (Vol. 24, Issue 1, pp. 1–4). https://doi.org/10.1007/s00384-008-0585-y

Gronemeyer, S. A., Steen, R. G., Kauffman, W. M., Reddick, W. E., & Glass, J. O. (2000). Fast adipose tissue (FAT) assessment by MRI. *Magnetic Resonance Imaging*, *18*(7), 815–818. https://doi.org/10.1016/S0730-725X(00)00168-5

Healy, J. C., & Reznek, R. H. (2000). Peritoneal anatomy. *Imaging*, *12*(1), 1–9. https://doi.org/10.1259/img.12.1.120001

Holt, D. Q., Moore, G. T., Strauss, B. J. G., Hamilton, A. L., De Cruz, P., & Kamm, M. A. (2017). Visceral adiposity predicts post-operative Crohn's disease recurrence. *Alimentary Pharmacology and Therapeutics*, *45*(9), 1255–1264. https://doi.org/10.1111/apt.14018

Huh, J. Y., Park, Y. J., Ham, M., & Kim, J. B. (2014). Crosstalk between adipocytes and immune cells in adipose tissue inflammation and metabolic dysregulation in obesity. In *Molecules and Cells* (Vol. 37, Issue 5, pp. 365–371). Korean Society for Molecular and Cellular Biology. https://doi.org/10.14348/molcells.2014.0074

Klopfenstein, B. J., Kim, M. S., Krisky, C. M., Szumowski, J., Rooney, W. D., & Purnell, J. Q. (2012). Comparison of 3 T MRI and CT for the measurement of visceral and SAT adipose tissue in humans. *British Journal of Radiology*, *85*(1018), e826. https://doi.org/10.1259/bjr/57987644

Kredel, L. I., & Siegmund, B. (2014). Adipose-tissue and intestinal inflammation - visceral obesity and creeping fat. *Frontiers in Immunology*, *5*(SEP), 1–12. https://doi.org/10.3389/fimmu.2014.00462

Kucharzik, T., Wittig, B. M., Helwig, U., Börner, N., Rössler, A., Rath, S., Maaser, C., Naumann, A., Pelster, G., Spengler, J., Büning, C., Gentz, E., Matthes, H., Nürnberg, D., Jung, A., Maul, J., Baumgart, D. C., Strobel, D., Manok, G., … Fähndrich, M. (2017). Use of Intestinal Ultrasound to Monitor Crohn's Disease Activity. *Clinical Gastroenterology and Hepatology*, *15*(4), 535-542.e2. https://doi.org/10.1016/j.cgh.2016.10.040

Kullberg, J., Ahlström, H., Johansson, L., & Frimmel, H. (2007). Automated and reproducible segmentation of visceral and SAT adipose tissue from abdominal MRI. *International Journal of Obesity*, *31*(12), 1806–1817. https://doi.org/10.1038/sj.ijo.0803671

Kullberg, J., Brandberg, J., Angelhed, J. E., Frimmel, H., Bergelin, E., Strid, L., AhlströM, H., Johansson, L., & Lönn, L. (2009). Whole-body adipose tissue analysis: Comparison of MRI, CT and dual energy X-ray absorptiometry. *British Journal of Radiology*, *82*(974), 123–130. https://doi.org/10.1259/bjr/80083156

Li, Y., Zhu, W., Gong, J., Zhang, W., Gu, L., Guo, Z., Cao, L., Shen, B., Li, N., & Li, J. (2015). Visceral fat area is associated with a high risk for early postoperative recurrence in crohn's disease. *Colorectal Disease*, *17*(3), 225–234. https://doi.org/10.1111/codi.12798

Maconi, G., Greco, S., Duca, P., Ardizzone, S., Massari, A., Cassinotti, A., Radice, E., & Porro, G. B. (2008). Prevalence and clinical significance of sonographic evidence of mesenteric fat alterations in Crohn's disease. *Inflammatory Bowel Diseases*, *14*(11), 1555–1561. https://doi.org/10.1002/ibd.20515

Otsu, N. (1979). THRESHOLD SELECTION METHOD FROM GRAY-LEVEL HISTOGRAMS. *IEEE Trans Syst Man Cybern*, *SMC-9*(1), 62–66. https://doi.org/10.1109/tsmc.1979.4310076

Peyrin-Biroulet, L., Chamaillard, M., Gonzalez, F., Beclin, E., Decourcelle, C., Antunes, L., Gay, J., Neut, C., Colombel, J. F., & Desreumaux, P. (2007). Mesenteric fat in Crohn's disease: A pathogenetic hallmark or an innocent bystander? *Gut*, *56*(4), 577–583. https://doi.org/10.1136/gut.2005.082925

Rosen, E. D., & Spiegelman, B. M. (2014). What we talk about when we talk about fat. *Cell*, *156*(1–2), 20–44. https://doi.org/10.1016/j.cell.2013.12.012

Rossner, S., Bo, W. J., Hiltbrandt, E., Hinson, W., Karstaedt, N., Santago, P., Sobol, W. T., & Crouse, J. R. (1990). Adipose tissue determinations in cadavers - A comparison between cross-sectional planimetry and computed tomography. *International Journal of Obesity*, *14*(10), 893–902.

Seidell, J. C., Bakker, C. J. G., & Van Der Kooy, K. (1990). Imaging techniques for measuring adipose-tissue distribution - A comparison between computed tomography and 1.5-T magnetic resonance. *American Journal of Clinical Nutrition*, *51*(6), 953–957. https://doi.org/10.1093/ajcn/51.6.953

Sheehan, A. L., Warren, B. F., Gear, M. W. L., & Shepherd, N. A. (1992). Fat-wrapping in Crohn's disease: Pathological basis and relevance to surgical practice. *British Journal of Surgery*, *79*(9), 955–958. https://doi.org/10.1002/BJS.1800790934

Shen, W., Li, Y., Zou, Y., Cao, L., Cai, X., Gong, J., Xu, Y., & Zhu, W. (2019). Mesenteric Adipose Tissue Alterations in Crohn's Disease Are Associated with the Lymphatic System. *Inflammatory Bowel Diseases*, *25*(2), 283–293.

https://doi.org/10.1093/ibd/izy306

Trace region boundaries in binary image - MATLAB bwboundaries - MathWorks United Kingdom. (n.d.). Retrieved December 30, 2022, from https://uk.mathworks.com/help/images/ref/bwboundaries.html

Zhou, A., Murillo, H., & Peng, Q. (2011). Novel segmentation method for abdominal fat quantification by MRI. *Journal of Magnetic Resonance Imaging*, *34*(4), 852–860. https://doi.org/10.1002/jmri.22673

Zhou, Z., Xiong, Z., Shen, Y., Li, Z., Hu, X., & Hu, D. (2021). Magnetic resonance imaging-based body composition is associated with nutritional and inflammatory status: a longitudinal study in patients with Crohn's disease. *Insights into Imaging*, *12*(1), 1–12. https://doi.org/10.1186/s13244-021-01121-3

Zhu, Y., Qian, W., Huang, L., Xu, Y., Guo, Z., Cao, L., Gong, J., Coffey, J. C., Shen, B., Li, Y., & Zhu, W. (2021). Role of Extended Mesenteric Excision in Postoperative Recurrence of Crohn's Colitis: A Single-Center Study. *Clinical and Translational Gastroenterology*, *12*(10), e00407. https://doi.org/10.14309/ctg.0000000000000407

Zou, K. H., Warfield, S. K., Bharatha, A., Tempany, C. M. C., Kaus, M. R., Haker, S. J., Wells, W. M., Jolesz, F. A., & Kikinis, R. (2004). Statistical Validation of Image Segmentation Quality Based on a Spatial Overlap Index. *Academic Radiology*. https://doi.org/10.1016/S1076-6332(03)00671-8

5 MRI Changes in Visceral Fat in Crohn's Disease

5.1 Introduction

As explained in Chapter 3, fat hypertrophy is a radiological hallmark for CD that correlates well with fibrosis, transmural inflammation, and stricture formation. The developed segmentation algorithm simplifies abdominal fat analysis allowing for an objective and detailed measurements of abdominal fat in CD patients.

5.2 Single Slice Versus Volumetric Measurement of Abdominal Fat

While some studies examine abdominal fat measurements using volumetric measurements, most studies rely on single-slice cross-sectional imaging. In CT scans, single-slice measurements of abdominal fat tissue were primarily adapted to limit exposure to ionizing radiation. The use of manual and semi-automated segmentation methods in MRI limits the use of volumetric measurements as they are time-consuming. Some studies have shown that measurements of abdominal fat areas around the L3 and the L4 can be used as a surrogate measure for volumetric body fat in healthy volunteers (HV) (Shen et al., 2004) (Mourtzakis et al., 2008). However, other studies have indicated significant variations between single-slice and multi slice measurements (Ellis et al., 2007) (Kanaley et al., 2007). CD induces irregularity in abdominal fat tissue distribution, which may not be captured using single-slice imaging.

Erhayiem et al. investigated the utility of abdominal fat ratios in differentiating between inflammatory CD and complicated CD in a retrospective study. They collected CT scans from 50 CD patients (29 patients with complicated CD and 21 patients with inflammatory CD). The ratio of VAT to SAT fat areas was measured using a single-slice cross-sectional image at the level of the umbilicus (around the L4 vertebra). Their results demonstrated that patients with complicated CD had significantly higher abdominal fat ratios compared to patients with inflammatory CD (mean fat ratio for

complicated CD =0.48 ± 0.18, inflammatory CD=0.22 ± 0.09; p=.01). Figure 5.1 shows their results (Erhayiem et al., 2011).

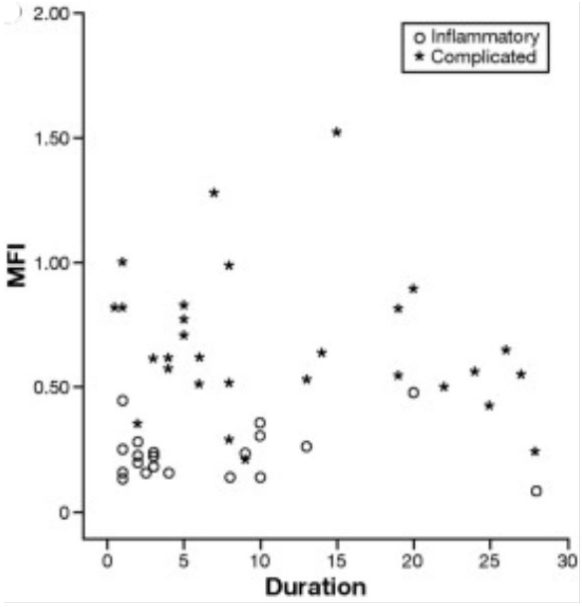

Figure 5.1: Differences in the ratio of VAT/SAT (MFI) between patients with inflammatory CD and patients with complicated CD plotted against the duration of the disease in years (Erhayiem et al., 2011).

Büning et al.'s study included 24 CD patients and 11 healthy controls, which were scanned using axial T1w-flash MRI sequences and total fat mass (FM) with air-displacement plethysmography. Both patients and HVs were females of similar age (P = 0.42) and BMI (P= 0.15). Their results showed a higher VAT/ total fat ratio in CD patients compared to healthy controls (65.2±24.4 mL/kg vs 36.7±24.5 mL/kg P=0.004). Figure 5.2 shows their results. Unlike the single-slice cross-sectional scanning method used in CT studies, the abdomen was scanned in the area between the symphysis pubis and the liver. Using a semi-automated segmentation software, they calculated different types of abdominal fat tissue volumes. They found that, on average, patients with CD accumulated nearly twice as much fat in the form of VAT compared to the healthy controls. Furthermore, their results showed an increased VAT/FM ratio at baseline, but not BMI, related to a higher disease activity six months later. This indicates that the assessment of VAT/FM ratios could have prognostic value in patients with CD (Büning et al., 2015).

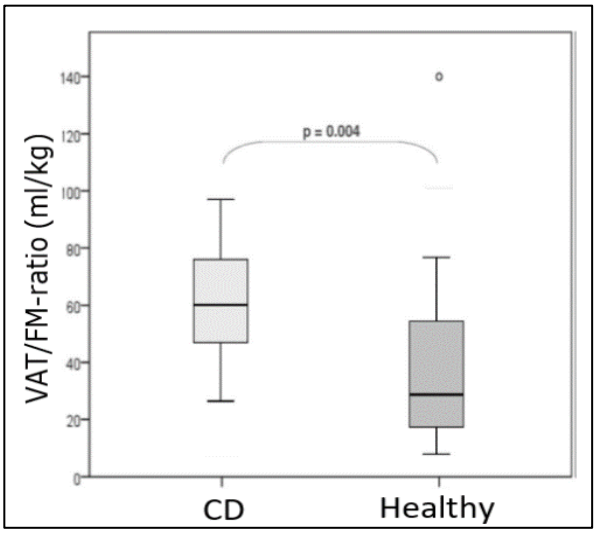

Figure 5.2: Results of measuring VAT to abdominal fat ratio produced by Büning by using air-displacement plethysmography to measure total abdominal fat (Büning et al., 2015).

Another study compared single-slice CT measurements at the L3 level with volumetric fat measurements on Dual-energy X-ray absorptiometry (DXA) in Crohn's patients. This study compared abdominal fat tissue measured from DXA scans with fat area measured from single-slice CT scans. While the study focused on muscle mass, their results show a very high correlation between CT measurements at the L3 and whole-body DXA scans in SAT volume measurements ($r=0.928$, $p<0.001$, $n=37$); however, the study did not mention any significant correlation in VAT volumes which is where fat hypertrophy may induce fat volume variations across the abdomen (Bredella et al., 2010).

As the developed segmentation algorithm eliminates the time-consuming process of manual segmentation, it allows for a direct comparison between single-slice and volumetric measurements on the same MRI scans.

5.3 Long Term Effects of Visceral Fat Hypertrophy

Another aspect of fat wrapping that can be studied with the aid of automated segmentation, is the long-term effects of fat wrapping. While it's been established as a marker for CD, long-term changes in abdominal fat due to CD has not been investigated thoroughly in research.

Z. Zhou et al. performed a longitudinal retrospective study evaluating the changes in MRI-based body composition during follow-ups in patients with CD. They included data from 49 CD patients that had baseline and follow-up MRE scans. VAT and SAT were manually segmented and measured at the level of the third lumbar vertebra (L3) from the axial T1-weighted images. The study compared multiple body compositions such as VAT areas, SAT areas, skeletal muscle and ratio of VAT to total abdominal fat (VAT/TAT) and compared them with disease activity biomarkers such as CRP and MRE scores. The correlation between CRP and body composition parameters was only reflected in the VA/TAT ratio ($r = 0.355$, $p < 0.05$). VA/TAT also showed high correlation with MRE scores proposed by Kitazume et al. ($r = 0.479$, $p < 0.01$) (Kitazume et al., 2019). Results also showed a decrease in the abdominal fat ratio (VAT/TAT) on follow-up scans compared to baseline scans in CD patients regardless of follow-up duration and treatment type implying that VAT/TAT ratios changes with treatment as patients go into remission (Figure 5.3) (Zhou et al., 2021).

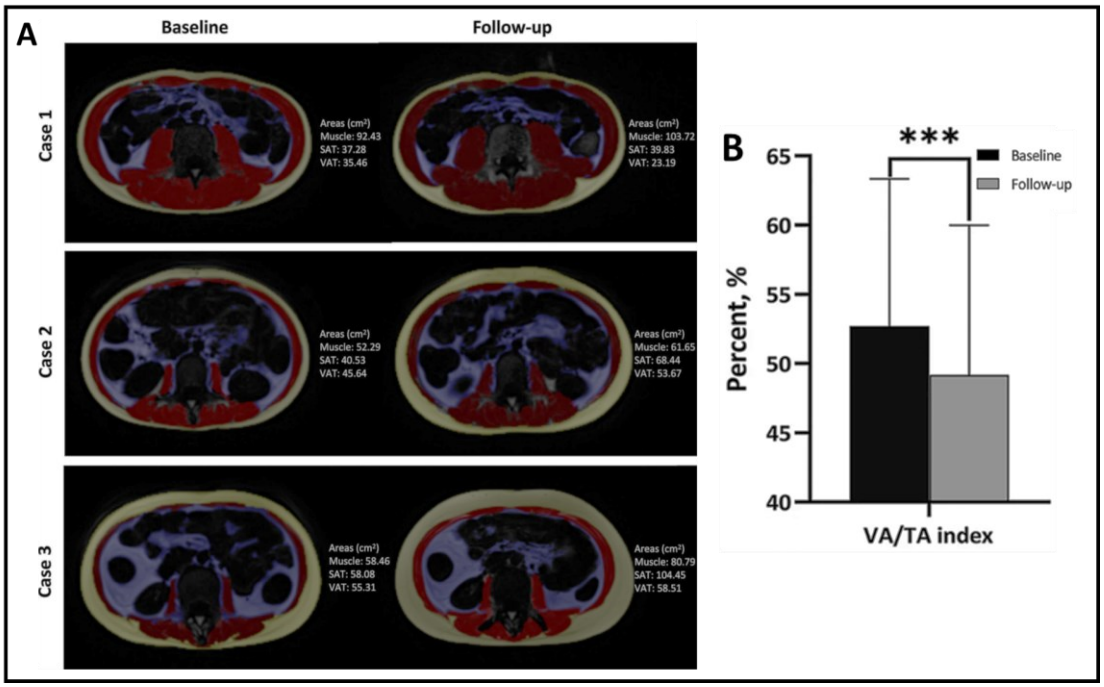

Figure 5.3: (A) Changes in abdominal fat areas during follow-up in three CD cases. The VAT/TAT ratio changes of all three cases are − 11.95%, − 9.01% and − 12.88%, respectively. (B) Value of VAT/TAT index at baseline and follow-up (Zhou et al., 2021).

5.4 Aims and Objectives

Based on the literature available, which depicts visceral fat hypertrophy as a radiological finding in CD, we hypothesize that it would be possible to use MRI volumetric measurements of intra- abdominal fat to assess the effects of fat wrapping in CD patients using the developed segmentation algorithm.

Aim: To quantify mesenteric fat hypertrophy by measuring VAT and SAT volumes on MRI scans using the developed segmentation algorithm.

Hypothesis: In a comparative study, the measured ratio of VAT to total adipose tissue (TAT) on MRI images will be higher in CD than in HVs. The measured ratio of VAT to TAT will change over time as a result of fat hypertrophy in CD patients in a retrospective longitudinal study using clinical MRI scans.

Objectives:

- Measure the ratio of VAT to TAT on retrospective scans of CD patients and HVs.
- Recruit and scan a cohort of HVs and CD patients for a prospective comparison test.
- Compare the results acquired from CD patients to HVs.
- Implement a sub-analysis across a selected group of CD patients and HVs matched for BMI to investigate the dependency of VAT/TAT measurements on BMI.
- Compare volumetric to single-slice measurements on 2-point Dixon MRI scans.
- Measure the ratio of VAT/TAT in CD patients on multiple MRI scans acquired across long periods to trace abdominal fat growth in each CD patient.

This chapter describes two separate retrospective studies and a prospective study performed to evaluate the extent of fat wrapping in CD patients. The first retrospective study compares 2-point Dixon MRI scans of CD patients and HVs to evaluate the differences in abdominal fat ratios in both groups. The second retrospective study evaluates abdominal fat volume changes across long periods of time by examining

retrospective MRE scans of CD patients that were acquired as part of their standard care practices. And finally, a prospective study evaluates the differences between patients with active CD and HVs recruited with a wide range of BMIs. The prospective study data was also used to examine the differences between single slice and volumetric measurements of abdominal fat.

5.5 Methods

5.5.1 Retrospective Comparative Study

2-point Dixon scans of CD patients and HVs were acquired from four previous studies. HV scans were acquired from and "The Effects of Oral Feeding and Gastric Emptying" (Murray et al., 2019) study which was approved by NHS ethics committee (ref: A16042015, issued: 12/04/2016). CD patients' scans were acquired from (Khalaf et al., 2018) and (Mcging et al., 2022).

5.5.2 Prospective Study Scanning Parameters

2-point Dixon axial scans were acquired in the supine position between the top of the hip joint and L2 vertebra on a Philips 3T Ingenia wide bore scanner (Philips, Best, The Netherlands). Table 5.1 shows the full scanning parameters.

Table 5.1: Prospective study scanning parameters

Parameter	2-echo Dixon
Plane	Axial
TR (ms)	3.7
TE (ms)	1.19, 2.37
Flip angle	10
Turbo factor	1
FOV (mm)	300×240×400
Matrix size	384×384×150
ST	3 mm
Pixel spacing (x,y) (in mm)	1.25×1.25
Compression	SENSE2

The study was approved by the University of Nottingham ethics committee (ref: 197-1901, issued: 17/05/2019) for recruiting HVs and the NHS ethics committee (ref: 19/YH/0337, issued: 26/11/2019) for recruiting CD patients. All subjects gave informed consent and were required to fast for a minimum of 6 hours prior to the scan. A planned sub-analysis was implemented across CD patients and HVs matched for BMI to investigate the effects of BMI variations on VAT and SAT volumes. Each patient was matched with a HV with the same gender and BMI (±1 kg/m^2).

5.5.3 Prospective Study Eligibility Criteria

CD patients inclusion criteria:

- Age > 16 years
- Active CD defined as:
  - Intestinal inflammation or deep ulceration seen on CT or MR enterography, with the disease activity quantified via the MaRIA score.
  - Ulceration seen at ileocolonoscopy, aiming for a simple endoscopic score for Crohn's disease (SES-CD) of 4-19 in the absence of complicated disease.
  - Faecal calprotectin of >250μg/g.
  - C-Reactive protein >5mg/dl.
- Ability to give informed consent.
- Willingness to adhere to the study protocol.

CD patients' exclusion criteria:

- Significant physical disability.
- Abnormal blood results other than those explained by CD.
- Pregnancy or breastfeeding.
- Contraindications for MRI scanning, e.g. pacemaker.
- Have any other inflammatory bowel disease other than CD that could influence the study's outcome.

HVs Inclusion criteria:

- Healthy.
- Aged 18-75.
- Male or female.
- Able to give informed consent.

HVs exclusion criteria:

- Pregnancy declared by the candidate.
- Contraindications for MRI scanning, i.e. metallic implants, pacemakers, history of metallic foreign body in the eye(s) and penetrating eye injury.

- History declared by the candidate of pre-existing gastrointestinal disorders that would affect the study results, such as inflammatory bowel disease, chronic liver disease and cancer in the abdomen.

5.5.4 Comparing Single-Slice to Volumetric Measurements on Dixon Scans

Single slice measurements in CT and MRI scans are typically applied on a 6 mm slice thickness. The study MRI scans have a slice thickness of 3 mm. Hence, to compare single slice to volumetric measurements, the automated segmentation software was used to segment two slices (6mm slice equivalence) around the L2, L3, L4 & L5 spinal regions. Pearson's correlation coefficient was used to calculate the correlation between volumetric and fat measurement in each region.

5.5.5 Longitudinal Retrospective Study Data Collection

MRE scans were acquired from NHS records under the following inclusion criteria:

- Age > 16 years.
- Participants have had multiple MRI scans across longs periods of times.
- Active CD defined as Intestinal inflammation or deep ulceration seen on MR enterography
- A minimum period of 6 months between each scan.

6 patients were excluded from the study for having different scanning resolutions between each scan, which can affect the comparative measurements.
All acquired MRE scans were taken between the year 2012 to 2022 under NHS ethical approval (ref: 296172 issued: 01/07/2021).

5.5.6 Abdominal Fat Analysis in Clinical MRI Scans

As mentioned in the previous chapter, a crucial part of the algorithm process is finding the line between VAT and SAT on an MRI image. Converting the MRI image to a binary image before the line extraction processes take place allows this algorithm to

work on various axial MRI scans by modifying the adaptive thresholding level to work for intended images. MRI sequences such as *T1* weighted and 2-point Dixon scans are traditionally used for fat analysis. However, the line extraction function can also work on Time-of-Flight MR Angiography scans (Chapter 6) and MRI scans that clinicians routinely acquire as part of CD patients' clinical care.

An MRI sequence that offers fat and water separation is required to study abdominal fat. For accuracy, the participant is typically asked to fast for a minimum of six hours before the scan, making sure that bowels are empty. If the patients' bowels contained water, they would appear bright on the image and might be misidentified as fat. CD patients typically undergo MRE scans as part of their treatment process, which are optimized to examine the bowels. Hence, prior to an MRE scan, the patient is required to drink an oral contrast agent making sure that the patient's bowels appear bright. An MRE scan requires multiple scanning sequences, which includes axial Single-Shot Fast Spin Echo (SS-FSE) used to assess for mural oedema and axial *T2* Fast Imaging Employing Steady-state Acquisition (FIESTA) which is used for differentiating between oedema and submucosal fat (Griffin et al., 2012). On SS-FSE images, fat appears bright compared to muscles which can be utilized for fat measurements; however, the contrast agent in the bowel causes them to have a similar contrast to the fat. On FIESTA fat-saturated images, fat tissue appears dark with bright bowels. By combing both images, the FIESTA images can be used as a reference to remove the bowels from the SS-FSE image as shown in Figure 5.4. Once the bowels are deleted from the SS-FSE images, the resulting binary image can be used to measure VAT and SAT fat using the line extraction function.

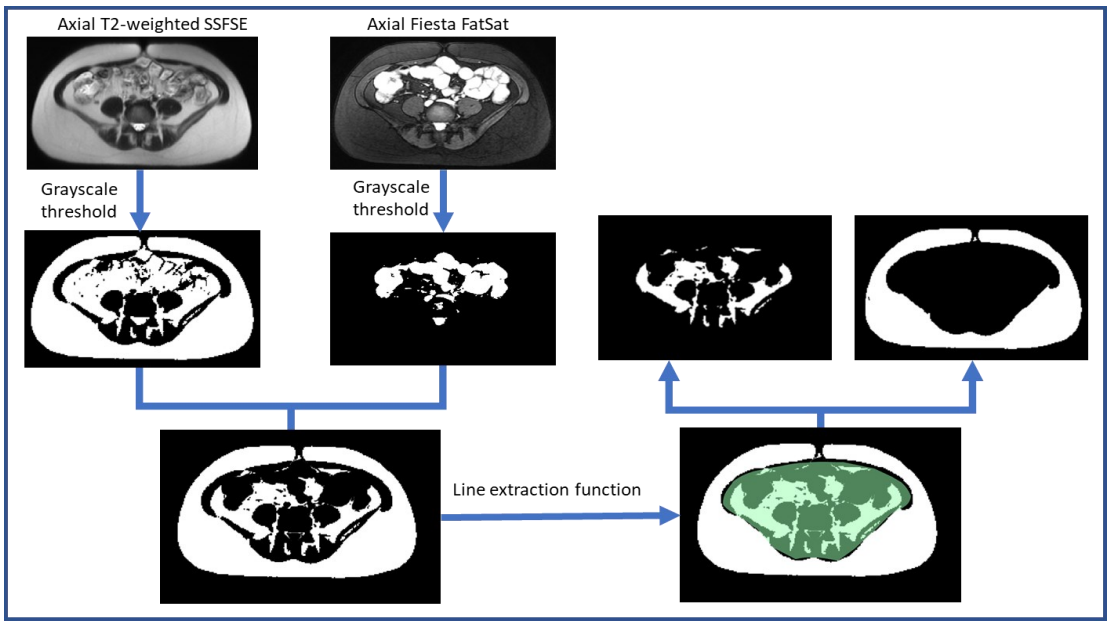

Figure 5.4: The use of FIESTA images to identify bowels in SSFSE images.

5.5.7 MRE Scans Segmentation Validation

To validate the automated segmentation performance on MRE scans, 2 slices were manually segmented around the L4 region on 11 SS-FSE MRI scans. Pearson's correlation coefficient was used to calculates the correlation between fat volumes calculated using automated and single-slice manual segmentation.

5.5.8 Statistical analysis

Shapiro-Wilk normality test was conducted on both groups to test the null hypothesis that the data has an abnormal distribution. Effect sizes were measured in normally distributed data using Cohen's d test with effect sizes of ($d = 0.2$) considered as small, ($d = 0.5$) as medium, and ($d \geq 0.8$) as large based on benchmarks suggested by Cohen (Cohen, 1988).

Statistical analysis with unpaired, two-tailed t-tests were conducted, and differences were considered significant when the p-value was ≤ 0.05. All absolute values are presented as mean ± SD.

Linear regression and Pearson's correlation coefficient were calculated to evaluate the effects BMI and abdominal VAT volumes have on VAT/TAT fat ratios using SPSS software.

5.6 Results

5.6.1 Retrospective Comparative Study

At total of 48 2-point Dixon scans were acquired from previous studies. Out of the 48, 17 were CD patients (9 males and 8 females) and 31 HVs (25 males and 6 females). Average BMIs were 26±5 kg/m^2 for CD patients and 27±5 kg/m^2 HVs. CD patients had slightly higher fat ratios compared to HVs (mean VAT/TAT in HV= 0.3±0.1 and CD=0.34±0.1; p=0.37). Male CD patients had significantly higher VAT/TAT ratios compared to male HVs (mean VAT/TAT in Male HV= 0.33±0.095 and Male CD=0.42±0.085; p=0.02). A Shapiro-Wilk test was performed on both CD and HV groups which did not show evidence of non-normality for VAT/TAT fat ratios (CD; W= .969, p = .803) (HV; W= .943, p = .097). These can be seen in Figure 5.5. No significant differences were observed in the measured in VAT and SAT volumes between CD patients and HVs.

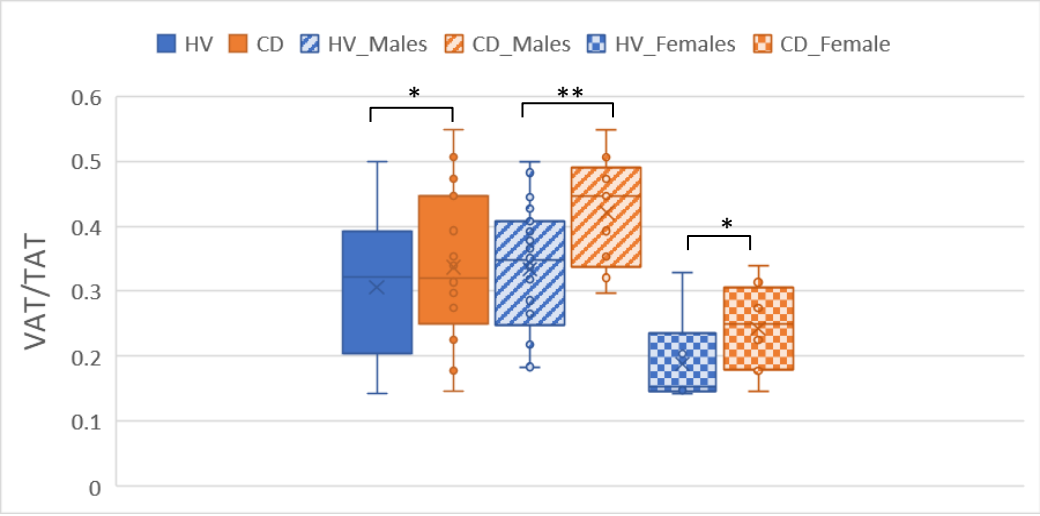

* Nonsignificant p-value (>0.05)
** p-value=0.023
Figure 5.5: Box diagram showing the differences in VAT/TAT ratios in CD patients compared HVs.

5.6.2 Prospective Comparative Study Results

15 patients with active CD and 17 HVs were recruited for this study. Details of the cohort are shown in Table 5.2. The HVs were selected to have a widespread BMI to investigate the effect of visceral fat growth on vascularity (BMI ranging from 21 to 42 kg/m^2 with an average of 29±7 kg/m^2). CD patients had an average BMI of 25±3 kg/m^2. The recruited patients had a higher average age compared with HVs. 13 out of the 15 CD patients underwent bowel resection surgery prior to the scan as part of their treatment. CD patients had significantly higher fat ratios compared to HVs (mean VAT/TAT in HV= 0.25±0.15 and CD=0.41±0.12; p=0.0013, d=1.17). Splitting the data by gender shows significant differences in VAT/TAT ratios in CD compared to HVs for both genders (mean VAT/TAT in females: HV= 0.17±0.04, CD=0.3±0.08; p =0.004) (mean VAT/TAT in Males: HV= 0.34±0.17, CD=0.49±0.06; p =0.03, d=1.12). These results are shown in Figure 5.6.

Table 5.2: Prospective comparative study participant's demographics

	CD	Control
n	15	17
Sex (%)		
Male	7 (54%)	8 (47%)
Female	6 (46%)	9 (53%)
Age (yr)		
Mean	49±14	30±10
Range	25-81	22-62
Mean BMI (±SD) (kg/m)	24(±3)	29(±7)
Mean CRP (±SD) (mg/L)	6.6±6.8	___
FC (±SD) (µg/g)	538±938	___

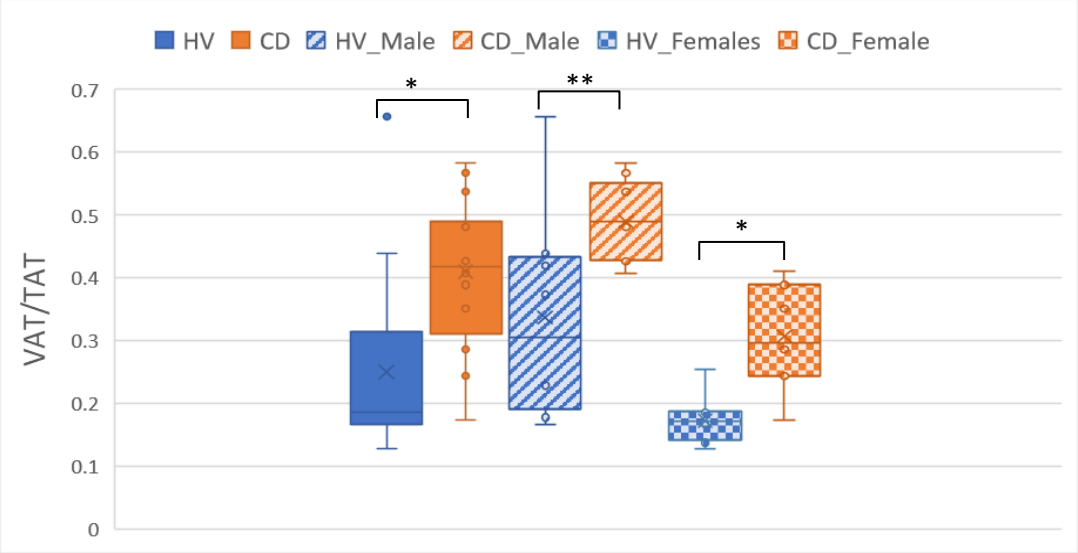

* p-value <0.005
** p-value<0.05

Figure 5.6: Box diagram showing the differences in VAT/TAT ratios in CD patients compared to HVs in the competitive prospective study.

No significant differences were found in VAT and SAT volumes between CD patients and HVs. The results showed no significant correlation between VAT/TAT ratio and BMIs for both CD patients (r= -0.025; p= 0.92) and HVs (r=-0.22; p= 0.39). These results are shown in Figure 5.7.

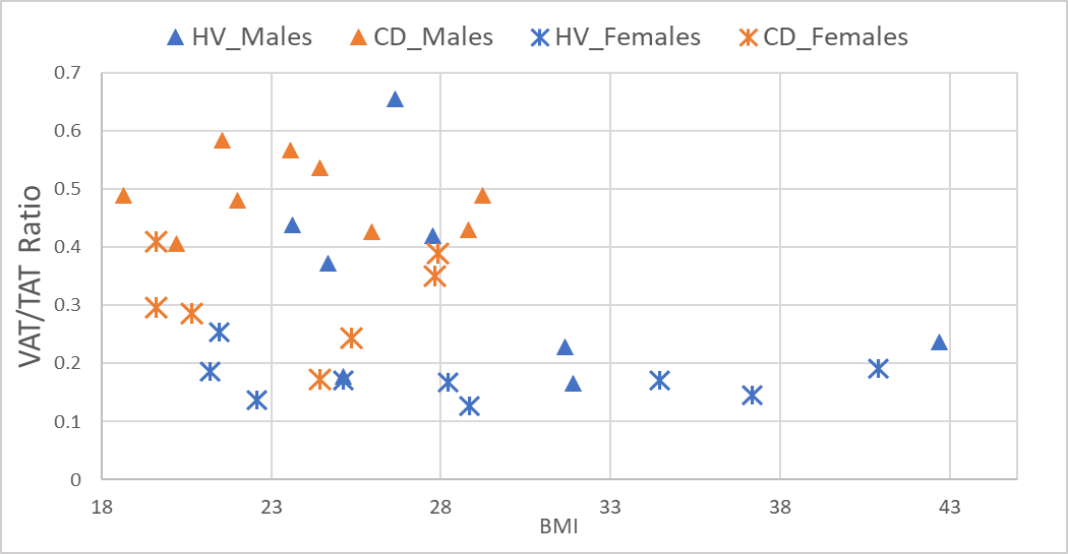

Figure 5.7: VAT/TAT ratio of CD patients and HVs plotted against their BMIs.

In HVs, a higher correlation was found between SAT and BMIs (r= 0.909, p <0.001) compared to VAT (r= 0.498, p = 0.042). In CD patients, both SAT and VAT fairly correlated with BMIs (VAT; r= 0.56, p = 0.024), (SAT; r= 0.569, p = 0.021). These results are shown in Figure 5.8.

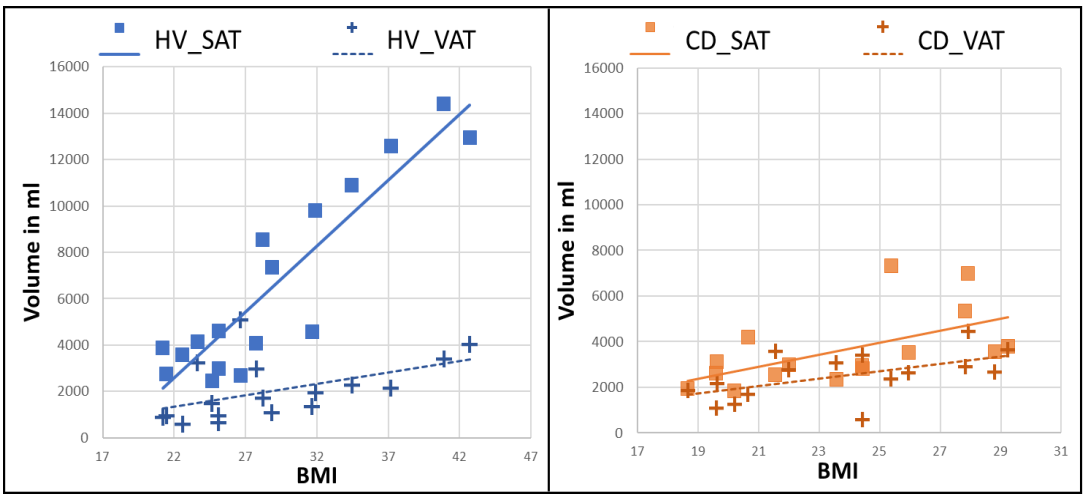

Figure 5.8: VAT and SAT volumes for HV (left) and CD patients' (right) plotted against their BMIs.

Out of the 17 HVs, 8 were selected to match 8 CD patients in BMIs and gender (mean BMI= 26±3 kg/m^2) for further comparison between the two groups. CD patients showed higher VAT/TAT values in the sub-analysis compared to HV with matched BMIs (mean VAT/TAT in matched BMIs test HVs=0.25±0.13 compared to 0.4±0.11 for CD; p=0.03). Figure 5.9 shows the VAT/TAT ratios of each HV paired with a CD patient with a matching BMI and gender.

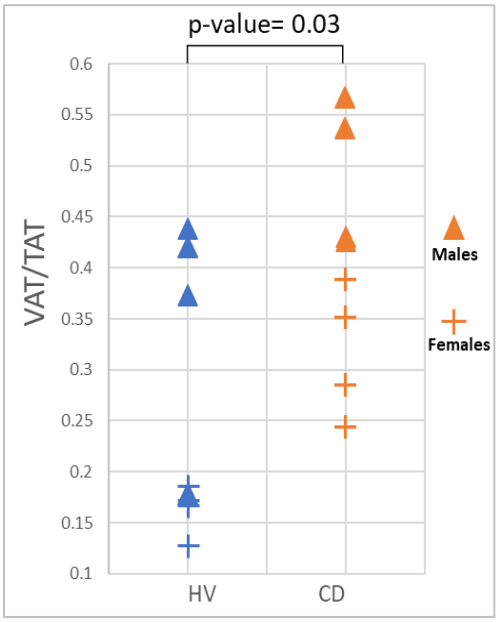

Figure 5.9: Paired dot graph showing HVs compared with CD patients with matching BMIs.

5.6.3 Comparing Single-Slice to Volumetric Abdominal Fat Measurements

Single slice measurements in CT and MRI scans are typically applied on a 6 mm slice thickness. This study's MRI scans have a slice thickness of 3 mm. Hence, to evaluate the efficiency of using single-slice abdominal fat measurements compared to volumetric measurements, the automated segmentation software was used to segment two slices (6mm slice equivalence) around the L2, L3, L4 & L5 spinal regions.

Table 5.3 shows the results of comparing volumetric fat measurements (L2 to the hip joint) to single-slice measurements around the L2, L3, L4 and L5 regions for CD patients and HVs.

Results showed very high correlation between single-slice and volumetric fat measurements (L2 to the hip joint) and single-slice measurements for both CD and HVs with highest correlation for VAT, SAT, and VAT/TAT ratio around the L5 region.

Table 5.3: Comparing the results of single-slice and volumetric measurements

	VAT		SAT		VAT/TAT	
	HV	CD	HV	CD	HV	CD
Average fat volume ± std						
Volumetric	2038±1304	2509±1031	6607±4089	3622±1630	0.25±0.14	0.41±0.12
L2	61±46	71±42	123±91	69±34	0.34±0.17	0.47±0.13
L3	58±41	67±38	152±99	84±39	0.28±0.15	0.43±0.15
L4	50±37	65±31	182±107	99±44	0.22±0.14	0.39±0.12
L5	57±32	65±26	197±121	113±51	0.25±0.14	0.37±0.11
Pearson's correlation with volumetric measurements						
L2	0.967*	0.847*	0.977*	0.918*	0.940*	0.866*
L3	0.988*	0.891*	0.982*	0.941*	0.979*	0.933*
L4	0.985*	0.937*	0.991*	0.911*	0.982*	0.943*
L5	0.982*	0.958*	0.994*	0.971*	0.977*	0.954*

* p-value<0.001

Figure 5.10 shows VAT, SAT and VAT/TAT ratios calculated from single-slice measurements around the four spinal regions plotted against volumetric measurements for HVs and CD patients.

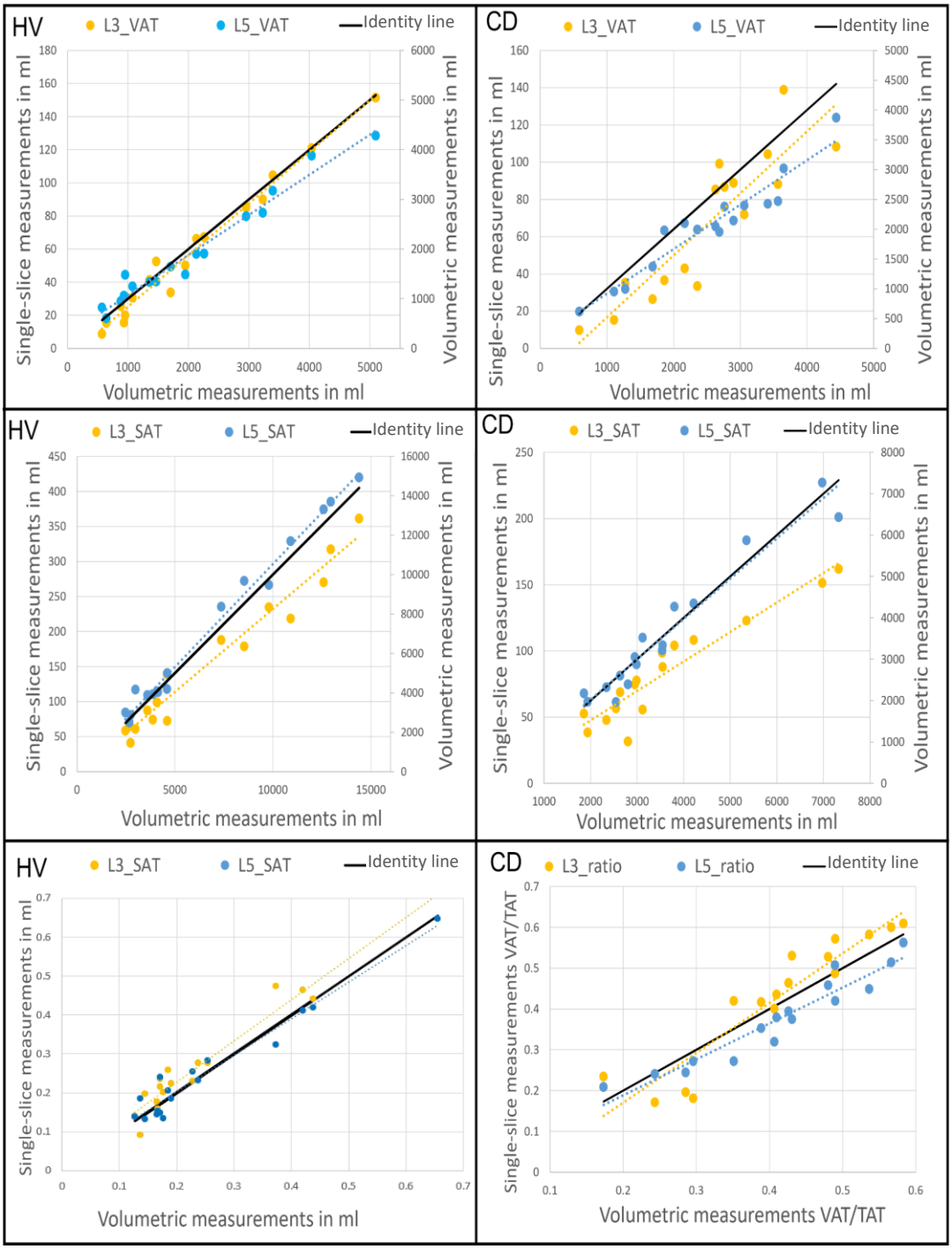

Figure 5.10: Scatter plots showing the correlation between single-slice (L3 and L5) and volumetric measurements for VAT (first row), SAT (second row) and VAT/TAT ratios (bottom row) for HVs (left) and CD patients (right).

5.6.4 Longitudinal Retrospective Study

A total of 41 MRE scans from 16 CD patients with multiple MRE scans were acquired from NHS records. 6 patients were excluded from the study for having different scanning resolutions between each scan, which can affect the comparative measurements. As a result, 25 MRE scans acquired from 10 CD patients (5 males) were included in the study. Out of the 10 patients, 5 had three scans at separate time points, and 5 had two scans with a minimum of one year between each MRE scan.

To validate the performance of the segmentation algorithm on the CD patients' scans collected from NUH database, out of the 25 scans included in this study 11 scans were randomly selected for manual segmentation. Two axial slices were manually segmented around the L4 region as some of the scans did not include the L5 region. Results showed a very high correlation between manual single-slice measurements and automated algorithm volumetric measurements for VAT ($r=0.98$; $p<0.001$), SAT ($r=0.87$; $p<0.001$) and VAT/TAT ratios ($r=0.92$; $p<0.001$). These results are shown in Figure 5.11.

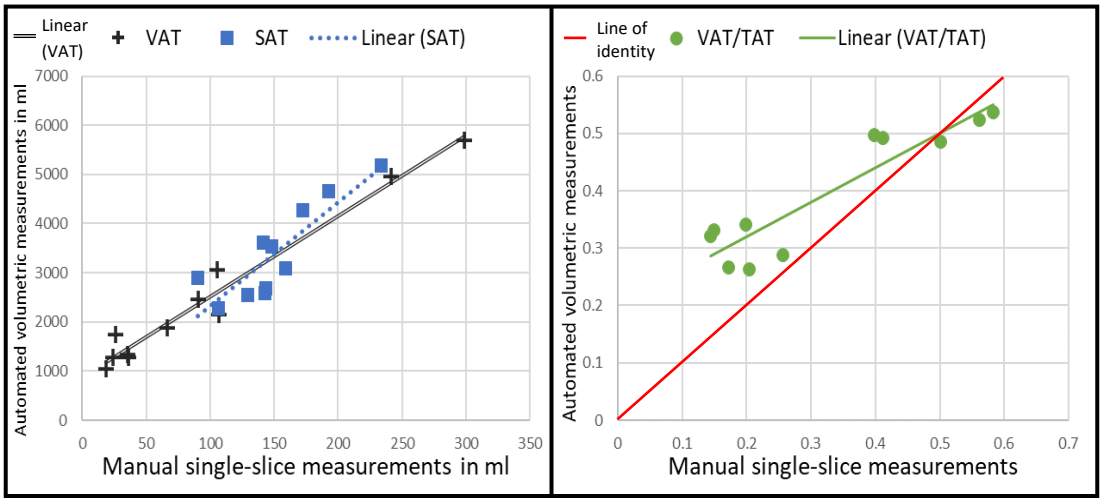

Figure 5.11: Scatter plots showing the correlation between manual single-slice and automated volumetric measurements for VAT & SAT (left) and VAT/TAT ratios (right).

Between the first and the last scan, 7 patients (4 males and 3 females) showed an increase in VAT/TAT ratio (mean VAT/TAT changes= +5.9%±5.6%; over a period of 125±64 months) and 3 patients had a decrease in VAT/TAT ratios (mean VAT/TAT changes= 4.5% ±3.7%; over a period of 77±43 months). For VAT volumes, 5 CD

patients showed an increase between the first and last acquired scan (mean VAT changes= +21%±14%; over a period of 103±59 months) and 5 patients showed a decrease in VAT volumes (mean VAT changes= -15%±12%; over a period of 91±44 months). For SAT volumes, 5 CD patients showed an increase between the first and last acquired scan (mean SAT changes= +20%±13%; over a period of 81±37 months) and 5 patients showed a decrease in VAT volumes (mean SAT changes= -18%±8%; over a period of 89±47 months). These are shown in Figure 5.12.

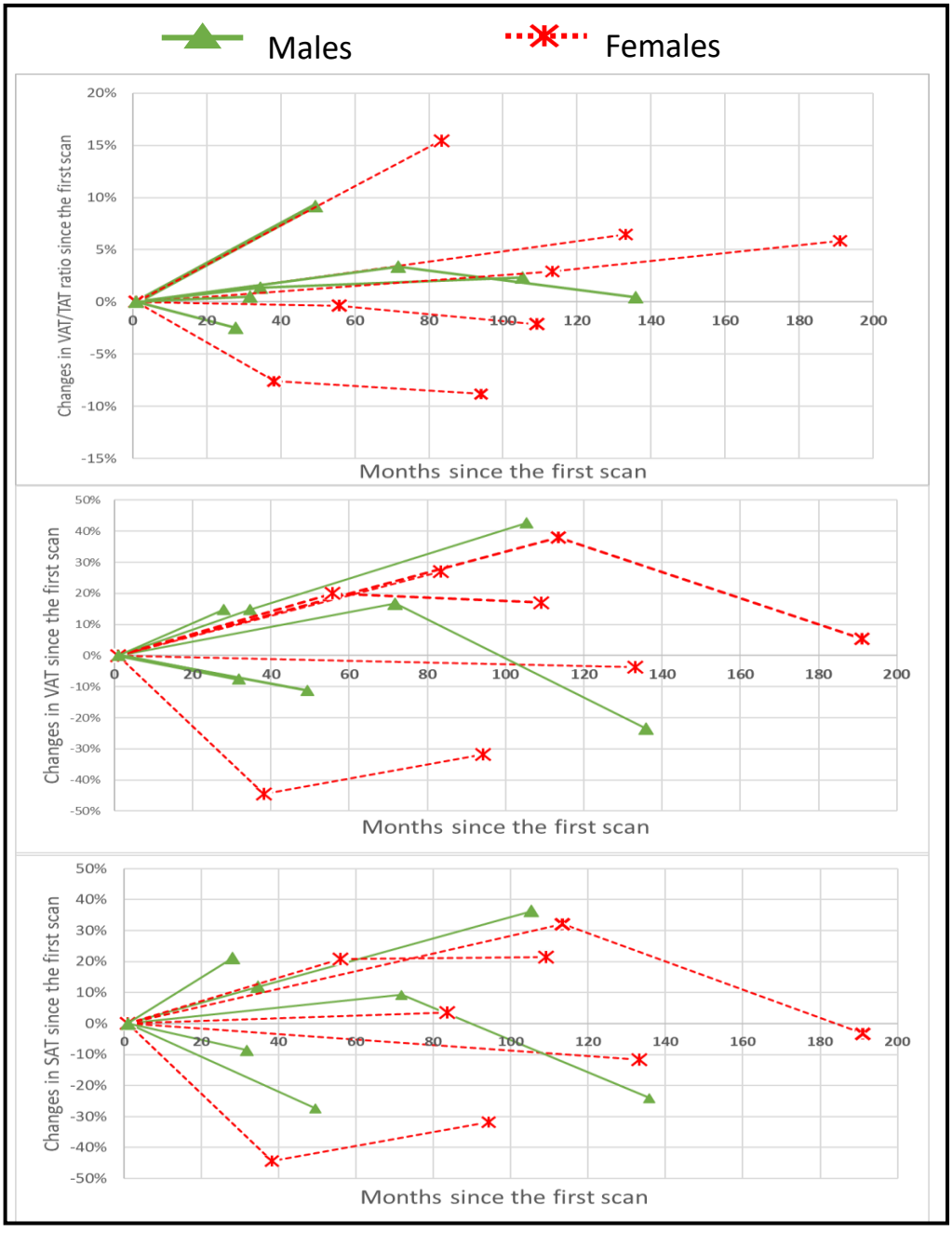

Figure 5.12: Changes in VAT/TAT ratio (top), VAT (middle), SAT (bottom) plotted against time since the first scan in months.

5.7 Discussion

Using the segmentation algorithm, a retrospective study was performed using MRI Dixon images of CD patients and HVs acquired from previous studies. These results were shown in Figure 5.5 (Chapter 5.6.2). These results did not show significant differences in VAT/TAT ratios between the two groups which could be explained by the high ratio of males to females in HVs (25 males and 6 females). Splitting the data by gender revealed significant differences in VAT/TAT ratios between male CD and HVs (mean VAT/TAT in HV= 0.33±0.095 and CD=0.42±0.085; p =0.02). No significant differences between female HVs and CD patients were found which can be explained by the small number of female subjects in both groups (8 CD and 6 HVs) and the significant differences in BMIs (26±4 kg/m^2 for CD patients compared to 23±2 kg/m^2 for HVs).

For further analysis, we recruited a cohort of 15 CD patients and 17 HVs with a wide range of BMIs for a prospective comparative study. Results shown in Figure 5.6 indicate that CD patients had a significantly higher VAT/TAT fat ratios compared to HVs (mean VAT/TAT in HV= 0.25±0.15 and CD=0.41±0.12; p =0.0013, d=1.12). The differences proceeded even after splitting the data by gender (mean VAT/TAT in females: HV= 0.17±0.04, CD=0.3±0.08; p =0.004) (mean VAT/TAT in Males: HV= 0.34±0.17, CD=0.49±0.06; p =0.03). Sub-analysis results displayed in Figure 5.9 showed that CD patients had a significantly higher VAT/TAT ratios compared to HVs after matching for BMI and gender. While VAT and SAT volumes showed significant correlation with BMI (as shown in Figure 5.8), VAT/TAT ratios showed no correlation with BMI (as shown in Figure 5.7) making it a more robust measurement to assess the effects of fat wrapping in CD patients. These results agree with previous studies which showed significant differences in VAT/TAT ratio between CD patients and HVs (Desreumaux et al., 1999), CD patients with higher and lower disease activity (Labarthe et al., 2020) and CD patients with complicated and inflammatory CD (Erhayiem et al., 2011).

Table 5.3 shows a detailed analysis comparing volumetric fat measurements with single-slice measurements taken at the level of L2, L3, L4 and L5. Results showed that single-slice measurements highly correlated with volumetric measurements across all regions. Measurements at the L5 level showed correlation values above 0.95 for both fat tissues across CD patients and HVs. Previous studies have been conducted on the validity of single-slice fat tissue measurements however, they were mostly conducted on HVs (Shen et al., 2004) (Mourtzakis et al., 2008). These results showed that while the correlation between single-slice and multi-slice measurements can vary depending on the spinal position in CD patients, they can still be used as a surrogate measurement for volumetric fat volumes. However, these small variations may have a larger impact on studies with small sample size. For example, for the sub-analysis group, volumetric measurements revealed significant differences between HVs and CD patients (mean VAT/TAT in HVs=0.25±0.13 compared to 0.4±0.11 for CD; p=0.03), these differences become insignificant when using measurements at L5 (mean VAT/TAT in HVs=0.25±0.11 and 0.35±0.09 for CD; p=0.08).

For the longitudinal retrospective study, automated volumetric fat measurements showed high correlation to manual single-slice measurements at the L4 region on 11 randomly selected MRE scans.

Results showed that even though VAT and SAT volumes fluctuated between each scan, VAT/TAT ratios increased in 7 out of the 10 CD patients between their first and last acquired MRE scan. While more information regarding treatment and surgical history is required for further analysis, previous studies showed a high correlation between disease activity and VAT/TAT ratios in longitudinal studies of CD patients. Z. Zhou et al.'s study showed a decrease in the VAT/TAT ratios on follow-up scans compared to baseline scans in CD patients regardless of follow-up duration and treatment type. However, their results also showed that VAT/TAT correlated well with CRP ($r = 0.355$, $p < 0.05$) and MRE scores ($r = 0.479$, $p < 0.01$) (Zhou et al., 2021). Büning et al. used air-displacement plethysmography to measure total abdominal fat. Their results showed an increased VAT/FM ratio at baseline, but not BMI, which related to a higher disease activity six months after the baseline measurements (Büning et al., 2015).

The results further validate the value of abdominal fat measurements for IBD diseases such as CD. Fast and automated measurements of abdominal fat tissues not only can aid in quantifying the effects of visceral fat hypertrophy, but they also allow for further detailed analysis of abdominal fat distribution such as comparing the fat volumes at the L2, L3, L4 and L5. Characterizing abdominal fat distribution can potentially reveal whether the effects of fat wrapping are higher around the effected bowel segments compared with the rest of the abdominal region.

The use of FIESTA and SS-FSE scans allow for identification of the bowel location however, patient movement between each scan causes further segmentation errors. In the prospective study, CD patients had a higher age compared to HV (CD age =49±14 and HV age=30±100) which may influence abdominal fat differences between the two groups. For the retrospective longitudinal study, more information about the treatment, surgeries, and medical history is required for further analysis. Since the MRE scan sequences were not optimized for imaging fat, noise interferences and image contrast variations cause some fat mis-registrations.

5.8 Conclusion

Establishing a significant correlation between single-slice and volumetric abdominal fat measurements in CD patients could potentially help future IBD researchers that do not have access to an automated segmentation method.

Both retrospective and prospective comparative studies showed significant differences in VAT/TAT ratio between CD patients and HVs demonstrating the usefulness of the VAT/TAT ratio as a surrogate measure for fat wrapping in CD. Thus, paving the way for the inclusion of an accurate and objective assessment of fat wrapping in CD disease activity metrics. Further validation to standard disease activity metrics is needed across larger cohorts to better investigate the utility of abdominal fat ratios as a potential biomarker as a non-invasive measure of disease activity.

References

Bredella, M. A., Ghomi, R. H., Thomas, B. J., Torriani, M., Brick, D. J., Gerweck, A. V., Misra, M., Klibanski, A., & Miller, K. K. (2010). Comparison of DXA and CT in the assessment of body composition in premenopausal women with obesity and anorexia nervosa. *Obesity*, *18*(11), 2227–2233. https://doi.org/10.1038/oby.2010.5

Büning, C., Von Kraft, C., Hermsdorf, M., Gentz, E., Wirth, E. K., Valentini, L., & Haas, V. (2015). Visceral adipose tissue in patients with Crohn's disease correlates with disease activity, inflammatory markers, and outcome. *Inflammatory Bowel Diseases*, *21*(11), 2590–2597. https://doi.org/10.1097/MIB.0000000000000527

Cohen, J. (1988). Statistical Power Analysis for the Behavioral Sciences. In *Statistical Power Analysis for the Behavioral Sciences*. Routledge. https://doi.org/10.4324/9780203771587

Desreumaux, P., Ernst, O., Geboes, K., Gambiez, L., Berrebi, D., Muller-Alouf, H., Hafraoui, S., Emilie, D., Ectors, N., Peuchmaur, M., Cortot, A., Capeon, M., Auwerx, J., & Colombel, J. F. (1999). Inflammatory alterations in mesenteric adipose tissue in Crohn's disease. *Gastroenterology*, *117*(1), 73–81. https://doi.org/10.1016/S0016-5085(99)70552-4

Ellis, K. J., Grund, B., Visnegarwala, F., Thackeray, L., Miller, C. G., Chesson, C. E., El-Sadr, W., & Carr, A. (2007). Visceral and SAT adiposity measurements in adults: Influence of measurement site. *Obesity*, *15*(6), 1441–1447. https://doi.org/10.1038/oby.2007.172

Erhayiem, B., Dhingsa, R., Hawkey, C. J., & Subramanian, V. (2011). Ratio of Visceral to SAT Fat Area Is a Biomarker of Complicated Crohn's Disease. *Clinical Gastroenterology and Hepatology*, *9*(8), 684-687.e1. https://doi.org/10.1016/j.cgh.2011.05.005

Griffin, N., Grant, L. A., Anderson, S., Irving, P., & Sanderson, J. (2012). Small bowel MR enterography: Problem solving in Crohn's disease. In *Insights into Imaging* (Vol. 3, Issue 3, pp. 251–263). Springer. https://doi.org/10.1007/s13244-012-0154-3

Kanaley, J. A., Giannopoulou, I., & Ploutz-Snyder, L. L. (2007). Regional differences in abdominal fat loss. *International Journal of Obesity*, *31*(1), 147–152. https://doi.org/10.1038/sj.ijo.0803359

Labarthe, G., Dolores, M., Verdalle-Cazes, M., Charpentier, C., Roullee, P., Dacher, J. N., Savoye, G., & Savoye-Collet, C. (2020). Magnetic resonance imaging assessment of body composition parameters in Crohn's disease. *Digestive and Liver Disease*, *52*(8), 878–884. https://doi.org/10.1016/j.dld.2020.06.024

Khalaf, A., Hoad, C. L., Menys, A., Radford, S., Nowak, A., Paparo, S., Lingaya, M.,

Falcone, Y., Singh, G., Taylor, S. A., Spiller, R. C., Gowland, P. A., Marciani, L., & Moran, G. W. (2018). P099 Postprandial intestinal motility and related physiology in active small-bowel Crohn's disease. *Journal of Crohn's and Colitis*, *12*(supplement_1), S143–S144. https://doi.org/10.1093/ecco-jcc/jjx180.226

Mcging, J., Nicholas, R., Serres, S., Greenhaff, P., Francis, S., & Moran, G. W. (2022). P062 31P MRS and MRI phenotyping of muscle metabolic quality in IBD fatigue. *Journal of Crohn's and Colitis*, *16*(Supplement_1), i171–i172. https://doi.org/10.1093/ecco-jcc/jjab232.191

Mourtzakis, M., Prado, C. M. M., Lieffers, J. R., Reiman, T., McCargar, L. J., & Baracos, V. E. (2008). A practical and precise approach to quantification of body composition in cancer patients using computed tomography images acquired during routine care. *Applied Physiology, Nutrition and Metabolism*, *33*(5), 997–1006. https://doi.org/10.1139/H08-075

Murray, K. A., Hoad, C. L., Garratt, J., Kaviani, M., Marciani, L., Smith, J. K., Siegmund, B., Gowland, P. A., Humes, D. J., & Spiller, R. C. (2019). A pilot study of visceral fat and its association with adipokines, stool calprotectin and symptoms in patients with diverticulosis. *PLoS ONE*, *14*(5), e0216528. https://doi.org/10.1371/journal.pone.0216528

Shen, W., Punyanitya, M., Wang, Z., Gallagher, D., St-Onge, M.-P., Albu, J., Heymsfield, S. B., & Heshka, S. (2004). Total body skeletal muscle and adipose tissue volumes: estimation from a single abdominal cross-sectional image. *Journal of Applied Physiology (Bethesda, Md.: 1985)*, *97*(6), 2333–2338. https://doi.org/10.1152/japplphysiol.00744.2004

Zhou, Z., Xiong, Z., Shen, Y., Li, Z., Hu, X., & Hu, D. (2021). Magnetic resonance imaging-based body composition is associated with nutritional and inflammatory status: a longitudinal study in patients with Crohn's disease. *Insights into Imaging*, *12*(1), 1–12. https://doi.org/10.1186/s13244-021-01121-3

Kitazume, Y., Fujioka, T., Takenaka, K., Oyama, J., Ohtsuka, K., Fujii, T., & Tateisi, U. (2019). Crohn disease: A 5-Point MR enterocolonography classification using enteroscopic findings. *American Journal of Roentgenology*, *212*(1), 67–76. https://doi.org/10.2214/AJR.17.18897

6 Mesenteric Blood Flow

6.1 Introduction

CD is known to be associated with hypervascularity of the mesentery, including vascular dilation and wide spacing of the vasa recta (Meyers & McGuire, 1995). The arteries supply to the small bowel branch out to a series of intestinal arteries within the mesentery. The terminal branches, or vasa recta, appear tall and widely spaced in the jejunum and become shorter and more closely arranged in the ileum (Stallard et al., 1994). Mesenteric hypervascularity is not specific to CD and could be seen in mesenteric thromboembolism, vasculitis, and bowel strangulation. The presence of the comb sign helps to identify acute inflammation in the patient with known CD and can help in differentiating active CD from hypovascular diseases such as lymphoma (Madureira, 2004).

6.2 Mesenteric Vascularity in CT

CT is regarded as the ideal modality to view the effects of hypervascularity in CD. On CT enterography scans (CTE), the hypervascularity of the mesentery with vascular dilation resembles the shape of the teeth of a comb; hence it's known as the comb sign. Some studies attempted to quantify the effects of the comb sign using CT; in most cases, it is used as a binary marker rather than a quantitative measurement where radiologists view each image and confirm or deny its presence in each subject. These binary measurements form a part of a more extensive disease activity scoring index (M. Chen et al., 2017).

Sakurai et al. investigated disease activity parameters on CTE including bowel-wall thickening, mural hyperenhancement, mesenteric hypervascularity (comb sign), increased fat density, mesenteric fibrofatty proliferation, and enlarged mesenteric lymph nodes validated against endoscopic findings using the Simple Endoscopic Score for Crohn's Disease (SES-CD) (Sakurai et al., 2017). The severity of mesenteric hypervascularity was assessed by measuring the diameter of each vessel and

characterising it as normal, mild or severe and was given a score of 0, 1 or 2 accordingly. Their results show that mesenteric hypervascularity exhibited a higher correlation with SES-CD compared with standard bowel wall measurements.

Wu et al. implanted a manual quantification method for measuring mesenteric hypervascularity in CD using CTE scans. This was done by drawing multiple 1 cm^2 ROIs around the mesentery in each scan, where expert radiologists manually calculated the number of vessels in each ROI in a double-blind manner (as shown in Figure 6.1). Their work showed that accurate quantification of the comb sign could be used as a categorical variable in a disease activity index for CD (Wu et al., 2012).

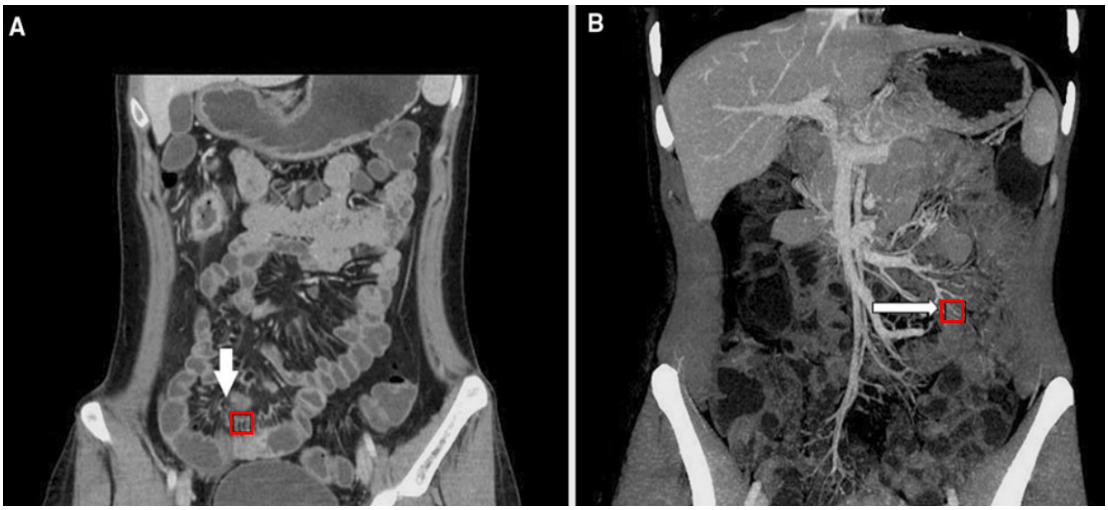

Figure 6.1: Coronal CTE images showing mesenteric vessels in a CD patient (A) compared to a healthy volunteer (B). A White arrow indicates a 1 cm^2 ROI used for generating a comb sign score (Wu et al., 2012).

Mesenteric angiography is a contrast agent-based X-ray diagnostic tool employed to examine vessels in the abdomen. While its primary use is to identify the source of bleeding in intestinal haemorrhage, it can be used to investigate the blood vessels that supply the small and large intestines. Figure 6.2 shows mesenteric angiography applied on a CD patient in a case study (Friedman & Tegtmeyer, 1979).

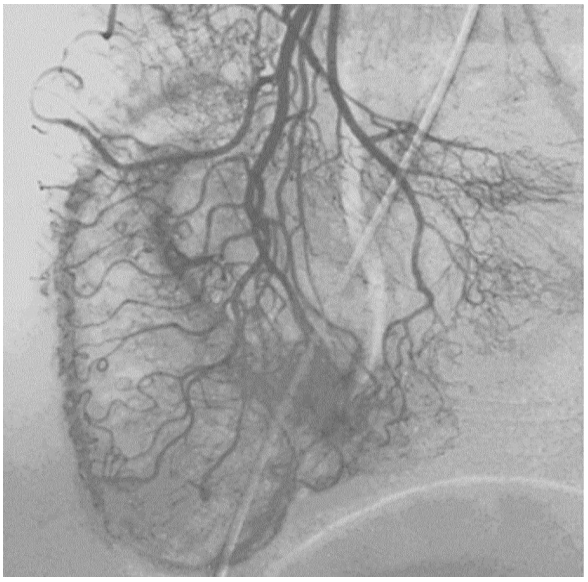

Figure 6.2: Mesenteric angiography used on a CD patient showing dilation of the vasa recta and tangled small blood vessels (Friedman & Tegtmeyer, 1979).

However, ionising radiation and the use of contrast agents limit the utility of CT and X-ray-based angiographic diagnostic tools for repeated assessment of hypervascularity in CD. Magnetic resonance angiographic imaging (MRA) techniques offer a safer and non-invasive alternative for visualising mesenteric vessels in CD.

6.3 Visualising Mesenteric Blood Flow Using MRA

Phase-Contrast angiography (PC-MRA) is used to study blood flow by applying bipolar magnetic field gradients, which cause a phase shift in moving spins. When stationary spins are subjected to bipolar gradients, they experience no net phase shift, but moving spins will gain a net phase shift proportionate to their flow rate. Spins flowing with the same speed but in opposite directions will have equal but opposite phase shifts. Blood flow velocity can be quantified by measuring phase changes. Although PC-MRA can provide quantitative measures, it typically requires a longer scanning time than other MRA methods. Its most common use is as a low-resolution sequence for identifying the location of the carotid arteries and distinguishing the degrees of stenosis in renal and carotid arteries (Wheaton & Miyazaki, 2012). Since PC-MRA requires a longer scanning time and cannot provide high-resolution images,

it is rarely used for simple angiography (without quantification) across large areas of the body, such as the abdomen.

Contrast-enhanced angiography uses contrast agents to shorten the *T1* of blood in vessels and hence provide contrast with respect to background tissue in a *T1* weighted image. This method can provide quantitative information about inflow when applied as a dynamic imaging approach. However, it does involve high costs, inconvenience, risk of using a contrast agent, and limited spatial resolution because of the need to image rapidly during the inflow.

Time of Flight (TOF) is one of the most widely used MRA imaging techniques, although it is not generally quantitative (it is closely related to Arterial Spin Labelling). TOF-MRA uses inflow-related enhancement to visualise the vessels. It obtains contrast between flowing blood and background tissues by altering the magnetization in the imaging slice, such that the magnitude of the magnetization from new spins moving into the slice is much larger than the magnitude of the magnetization from the stationary tissue spins (Ivancevic et al., 2009). This is achieved by applying multiple repetitive RF pulses, causing the stationary tissues in an image to be magnetically saturated with low steady-state magnetization levels. The new blood that flows into the slice has not experienced these pulses and thus possesses a higher initial magnetization. This causes the new blood to appear much brighter compared to background tissue as illustrated in Figure 6.3.

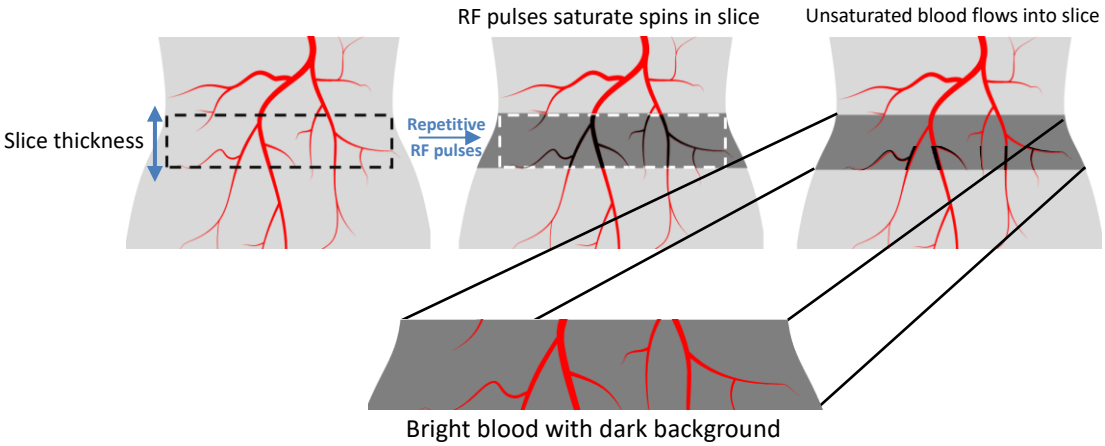

Figure 6.3: Illustration of TOF MRA flow-related enhancement, where fully magnetized blood flows into a slab of magnetically saturated tissue whose signal has been suppressed by repetitive RF pulses.

Figure 6.4 shows the difference between 2D TOF and Contrast-enhanced TOF imaging (Babiarz et al., 2009).

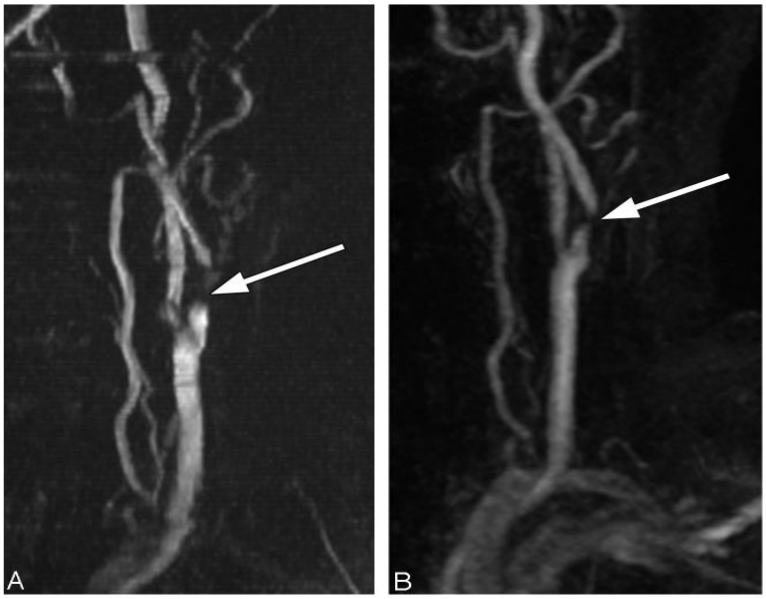

Figure 6.4: A sample carotid artery scanned using 2D TOF without Contrast enhancement (A) and contrast enhanced MRA (B) (Babiarz et al., 2009).

While there are other more advanced angiographic sequences, such as the quiescent interval single shot (QISS) and flow-sensitive dephasing (FSD) (Wheaton & Miyazaki, 2012), the simplicity of 2D TOF-MRA, along with its fast acquisition, makes it an ideal scanning sequence for quantifying mesenteric vessels across the whole abdominal region.

In order to use TOF-MRA to quantify mesenteric hypervascularity objectively, a fully automated image analysis algorithm is needed to characterise an increase in the volume of abdominal vessels robustly without relying on a visual assessment by radiologists. Most angiographic quantification methods take into account signal intensity, vessels' length, volume, and the number of branches (L. Chen et al., 2019) (Fedorov et al., 2012). Many algorithms developed for quantitatively characterising angiographic images operate in a semi-automated fashion, such as region growing techniques (Elena Martínez-Pérez et al., 1999) and active contouring (Nain et al., 2004). Fully automated methods have also been developed, such as Fuzzy-based Vascular Structure Enhancement (Forkert et al., 2011) and DeepVesselNet (Tetteh et al., 2020); however,

they are aimed at volumetric measurements or rely on machine learning which requires large training data.

A simpler quantification method can be obtained using a morphometric approach where a single line of pixels represents each vessel in a process known as skeletonization. This approach allows for easier vessel tracing and measurement of vessels' lengths and branching points (L. Chen et al., 2018) (L. Chen et al., 2019). This study focuses on measuring the number of vessels' branching points as a primary outcome. The low-resolution nature of contrast free TOF-MRA scans in the abdomen inhibits the ability of capturing the small vessels around the bowel that appear on CT images as the comb sign. Vessels arborization though are assumed to be good surrogates of vasodilation and increased blood flow typically observed in an inflamed segment of bowel. We hypothesise that arborization as measured through the arborization index is a sensitive measure of intestinal hyperaemia and intestinal inflammation.

6.4 Aims and Objectives

Aim: To develop an objective method to quantify mesenteric hyperaemia in vascularization of the bowel on TOF-MRA using a fully automated algorithm and test it in a small comparative study on a group of CD patients and HVs

Hypothesis: The detected vascularization on TOF images will be higher in CD than HVs.

Objectives:

- Develop and test a TOF-MRA sequence for imaging vessels across the whole abdominal area.
- Develop and test a MATLAB algorithm to automatically trace and quantify the extent of vessels breaching in the abdomen as a measure for the comb sign.
- Recruit and scan a cohort of HVs and CD patients for a comparison test.

- Validate the repeatability of the developed method by acquiring multiple scans of the same subjects, testing the coefficient of variance, biological variations and data distribution.
- Compare the results acquired from CD patients to HVs.
- Implement a sub-analysis across a selected group of CD patients and HVs matched for BMI to investigate the effect of visceral fat growth on vessels' breaching.
- Compare the measured volume of vessels breaching points to abdominal fat distribution measured using 2-point Dixon scans in both CD and HVs to investigate the relationship between vascularization and visceral fat as it has been suggested that fat is proinflammatory.

This chapter is split into three sections, first describing the optimisation of the MRI sequence, the second describing the development of the quantification algorithm and finally, the last detailing the study performed using this approach.

6.5 Methods

6.5.1 Optimisation of the MRI Sequence

TOF-MRA relies on flow-related perturbation of the saturation of the magnetization which occurs when stationary tissues are subjected to multiple RF pulses. These RF pulses repeatedly flip the longitudinal magnetisation towards the transverse plane. While increasing TR allows more time for *T1* relaxation between pulses, if the RF pulses are widely spaced, complete recovery occurs, and no saturation effect is observed. Hence, most TOF imaging sequences utilise shorter TR where the next RF pulse is applied before fully recovering longitudinal magnetisation. The longitudinal magnetisation evolves to a new lower steady state. The tissues within the imaged volume are partially saturated, lowering their MR signal. Fresh unsaturated blood flowing into the imaged area has not been subjected to these RF pulses and is therefore fully magnetised. When fresh blood enters a slice and is subjected to its first set of RF pulses, its signal is stronger than that from the tissues within the slab. A longer TE

increases the signal from vessels; however, this also causes signal loss due to spin-phase dispersion. A larger flip angle causes more background suppression but increases the power deposited in the subject and can thus limit the TR and scan time.

Maximum flow-related enhancement arises when inflowing blood completely replaces pre-existing blood in the slice. When blood flow is perpendicular to the slice, maximum enhancement occurs when:

$$v \geq \frac{SL}{TR}, \qquad (6.1)$$

where v is the velocity of blood flow and SL is the slice thickness. Hence, smaller slice thickness ensures that slower blood flow is included in the imaging.

All these parameters are limited by the maximum possible scanning time, especially when imaging the whole abdomen where each area of the scan is acquired during a breath hold to minimise motion artefacts.

An ideal abdominal angiographic sequence produces an image with high contrast between bright vessels and dark background tissue whilst allowing the data to be acquired in breath holds to minimise the effects of diaphragm motion during a reasonable scan time (total number of breath-holds required to cover the whole abdomen).

To investigate these trade-offs and identify an angiographic sequence that can be used for visualizing abdominal vessels, a total of 9 TOF-MRA scans were performed on a female HV (BMI=23) using a 3T Ingenia wide bore scanner (Philips, Best, The Netherlands). The scans were acquired under a Development Ethics Approval for scanning HVs. Each scan was performed with different parameters such as flip angle (FA), echo times (TE), repetition time (TR), slice thickness (ST) and slice orientation, as shown in Table 6.1.

Table 6.1: TOF test scans parameters

Orientation	TR (ms)	TE (ms)	FA (ms)	ST (mm)
Transverse	6	2.5	30	3
Transverse	6.8	1.88	50	3
Transverse	6.8	2.2	50	3
Transverse	6.8	2.2	60	3
Transverse	9.8	2.16	60	3
Sagittal	6	2.5	30	3
Sagittal	6	2.5	30	4
Sagittal	6.8	2.2	50	3
Coronal	6	2.5	30	3

TR, Repetition Time; TE, Echo Time; FA, Flip Angle; ST, Slice Thickness.

The TOF sequences' performance was evaluated by examining the histograms of the images and applying multiple grayscale thresholds on the images from each sequence, to determine a sequence that could offer the best separation between the dark background and the bright vessels. Figure 6.5 shows three images scanned using flip angles of 30º, 50º, and 60º. Applying different grayscale thresholds to each image indicates that a larger flip angle provides a darker background and a wider separation between the vessels and the rest of the body (including fat which has a short *T1* and hence shows brighter signals on these heavily *T1* weighted images).

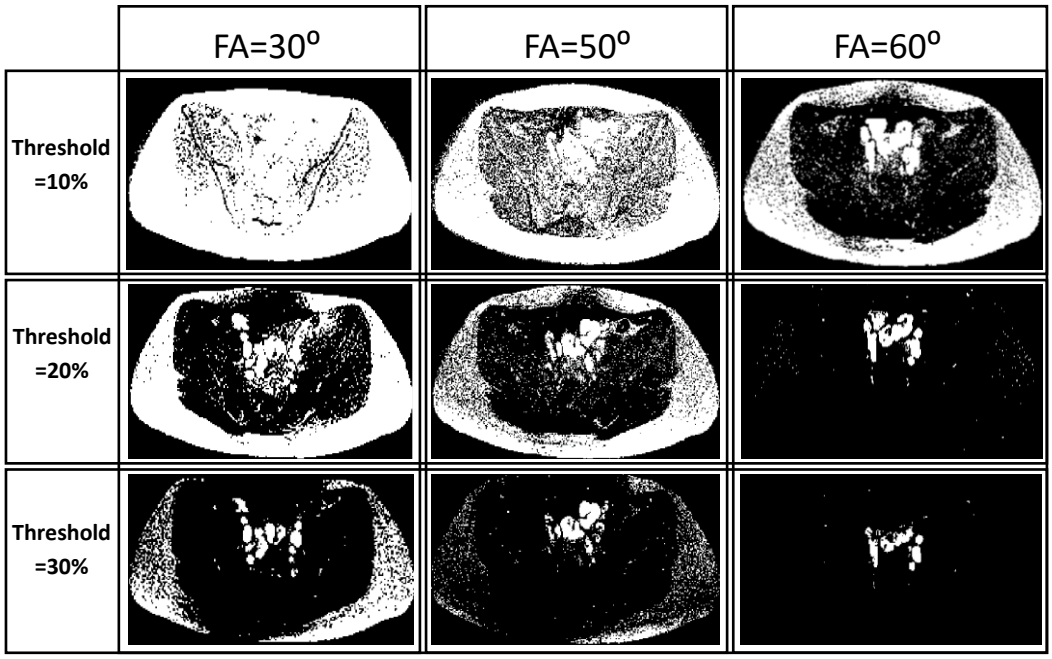

Figure 6.5: TOF images scanned with flip angles of 30º, 50 ºand 60º converted into binary images using thresholds of 10%, 20% and 30%.

These tests demonstrated that to visualise abdominal vessels, the ideal TOF scanning parameters are FA=60, TR=9.8, TE=2.16, ST=3 mm with a resolution of 0.9×1.2×3 mm. Visual examination showed that scans acquired in the transverse plane performed better than other orientations due to the direction of blood flow in the abdomen, despite taking longer to cover the whole abdomen. The scan was divided into five sets, each consisting of 16 slices. Each set was acquired during a breath-hold to avoid any motion artefacts in the images. Each breath-hold lasted 19 seconds with a short resting period between every breath-hold for the subject. The five sections were combined to form a data set of 80 slices covering the whole abdomen from the kidneys to the pelvic region.

6.5.2 TOF Quantification Algorithm

To objectively quantify the extent of vascular branching in the abdomen, a MATLAB algorithm was developed that tracks the vessels on a TOF-MRA data set using morphological operation, image filtering and maximum intensity projection. Figure 6.6 shows a brief outline of the subsequent algorithm.

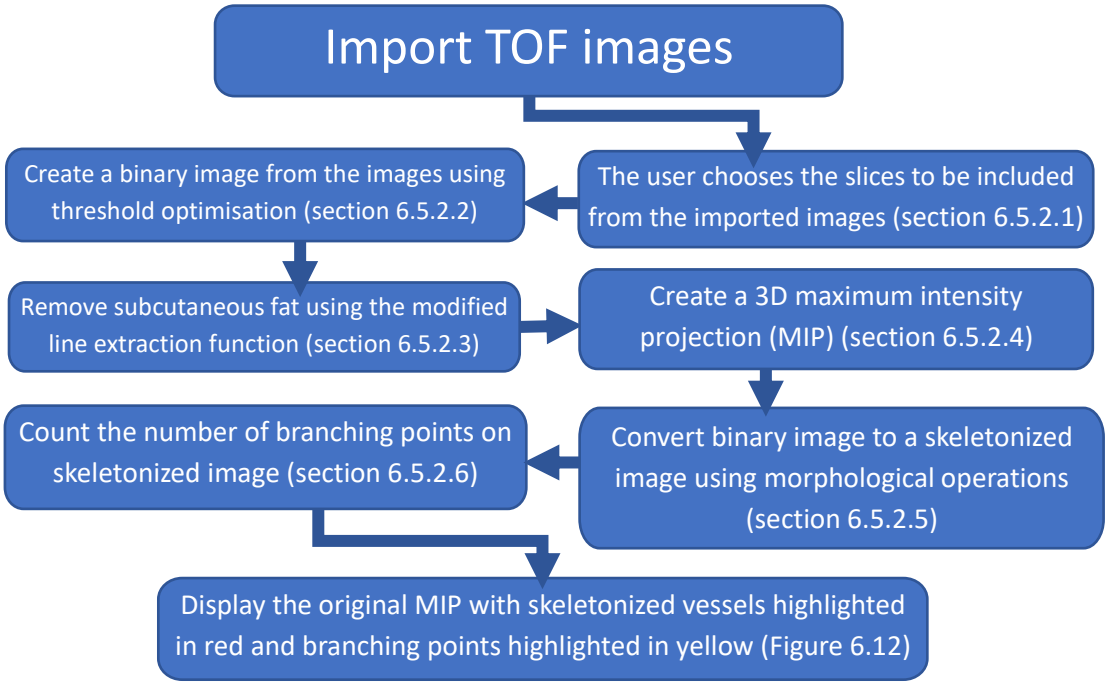

Figure 6.6: Flow chart showing a brief outline of the algorithm process

6.5.2.1 Selection of The Slices to be Used

When the user runs the code, an interactive pop-up window will appear, showing the images in multiple orientations to aid the user in identifying the axial slices included in the quantification. A second window then asks the user to input the start and ending axial slice numbers for the analysis. For this study, a region between the top of the hip joint and second lumbar vertebrae (L2) was selected for quantification across all subjects. Due to the height and position variations between each subject, this region's size and location can vary; hence, it was identified visually.

6.5.2.2 Threshold Optimisation

To apply morphological operations and shape filtering, a binary black and white image is required. To adequately convert the grayscale TOF images into a binary image, the threshold used to distinguish between the foreground and background needs to be chosen so that the binary image contains the highest possible volume of vessels while minimising background noise. Multiple grayscale thresholding methods have previously been developed to find the optimum threshold using the image's intensity histogram, such as Otsu's method, which chooses a threshold that minimises the intraclass variance of the converted image's black and white pixels. While these methods work very well for standard MRI images such as T2-weight images, the vessels on TOF images have very bright pixels compared to the background, and their volume constitutes a small percentage of the whole image. Hence, the intensity histogram of a TOF images looks more compact towards the lower pixel intensity values as shown in Figure 6.7. For this reason, typical thresholding methods cannot successfully identify the vessels and isolate them from the rest of the darker anatomical background.

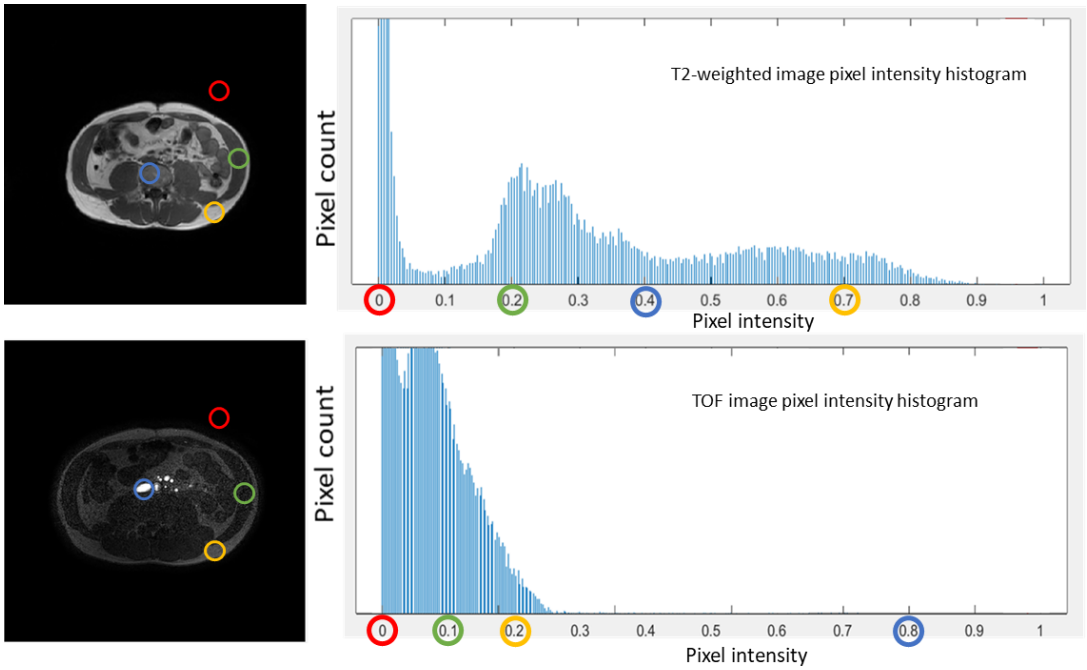

Figure 6.7: pixel intensity histogram of a TOF image compared with a T2-weighted image of the same subject.

Therefore, a specialised function was developed to find the ideal threshold for axial TOF images. This is done by an iterative thresholding method which finds the threshold value that offers the highest volume of pixels in the middle area of the image (largely visceral vessels and visceral fat) while having the lowest volume of pixels in the outer area of the image (largely SAT fat). The inner area is defined as a box in the centre of the image (as shown in Figure 6.8) that contains a third of the image's volume, whereas most of the background and noise and unwanted anatomical structures (particularly fat) are found outside this area.

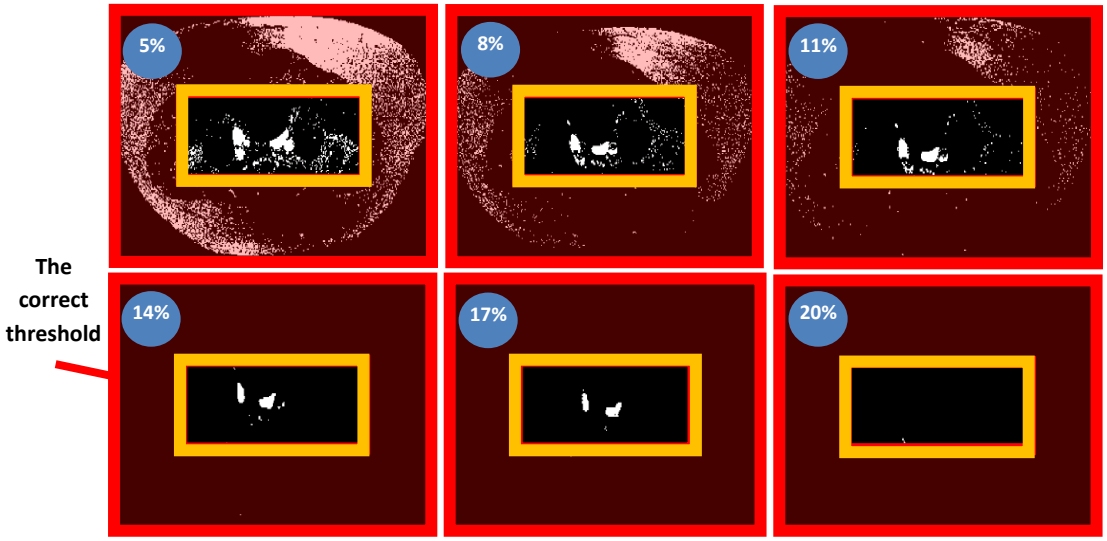

Figure 6.8: TOF iterative thresholding method where the algorithm generates multiple thresholds and finds the value which offers the maximum number of pixels in the yellow box and the lowest number of pixels in the red box.

6.5.2.3 Modified Line Extraction Function

The line extraction function described in Chapter 4.4.1.2 was adapted to work with different types of MRI sequences. By choosing a low threshold for the TOF sequence, VAT and SAT tissues become more pronounced , as shown in figure 6.8. The resulting binary image can then be used to segment the VAT area using the line extraction function. Vessels from the kidneys and liver which were included in the region of interest, were manually segmented out.

6.5.2.4 Maximum Intensity Projection

Almost all MRI methods for visualising vessels use maximum intensity projection (MIP) to display the results. The MIP is created by automatically selecting the maximum value of each voxel across multiple slices and showing the selected voxels in a single slice image. This technique allows for a 3D reconstruction of the vessels on a 2D plane, as shown in Figure 6.9. Generating multiple MIPs of a volumetric scan can provide depth information from the rotating perspective.

The algorithm generates a 3D MIP within the masked and thresholded TOF-MRA dataset. This is done by rotating the TOF image 360º in 20º increments and creating a MIP after each increment resulting in a total of 18 MIP images for each scan. While

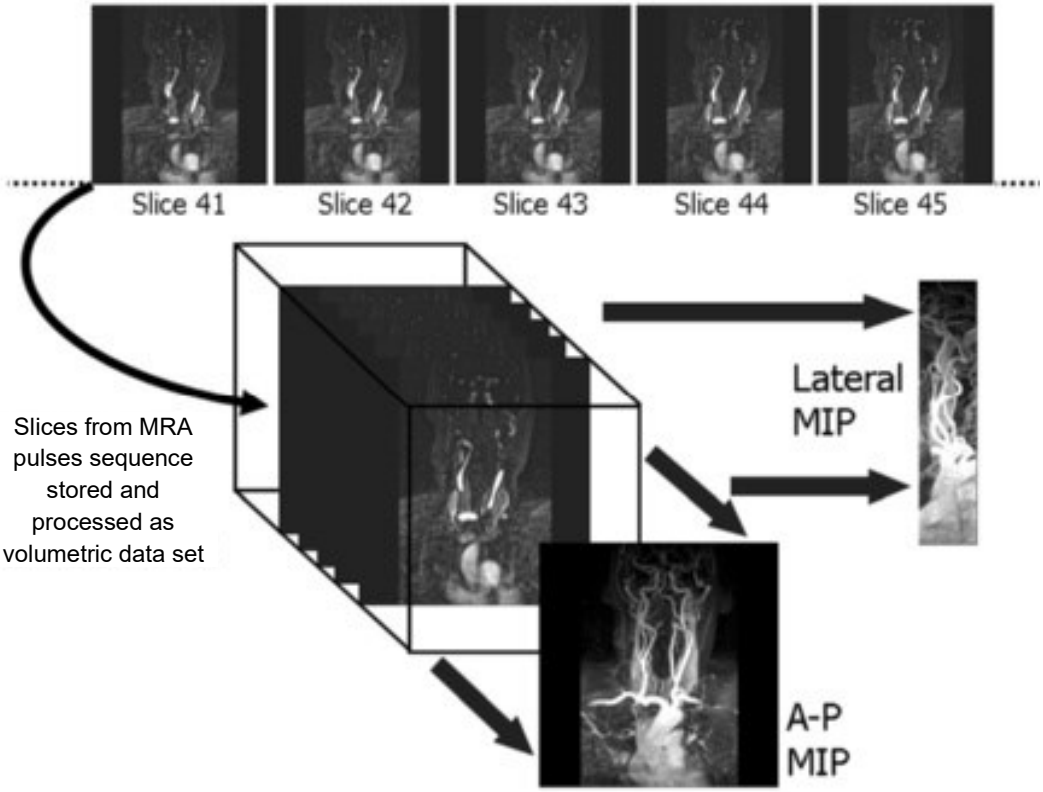

Figure 6.9: Maximum Intensity projection (MIP) diagram showing an overview of how projection images can be produced from a multi-slice MRA image data (Biglands et al., 2012).

measurements on a MIP image may be proportional to the true values, it does not reflect the exact measurements in mm due to the loss of depth information in the projection image.

6.5.2.5 Morphological Skeletonization and Branching Points

In order to analyse the vessels' length and branching points, each vessel is converted into a single line of pixels. This process is known as skeletonization. Similar to the erosion function described in Chapter 2.3.5, the function uses a combination of morphological operations and filters to achieve the desired structure (Kerschnitzki et al., 2013) (Lee et al., 1994). By using the right filters and structuring elements, each group of connected pixels can be eroded into a single pixel as shown in Figure 6.10.

As a result, each vessel in converted into a single line of pixels. This process is then repeated for each generated MIP.

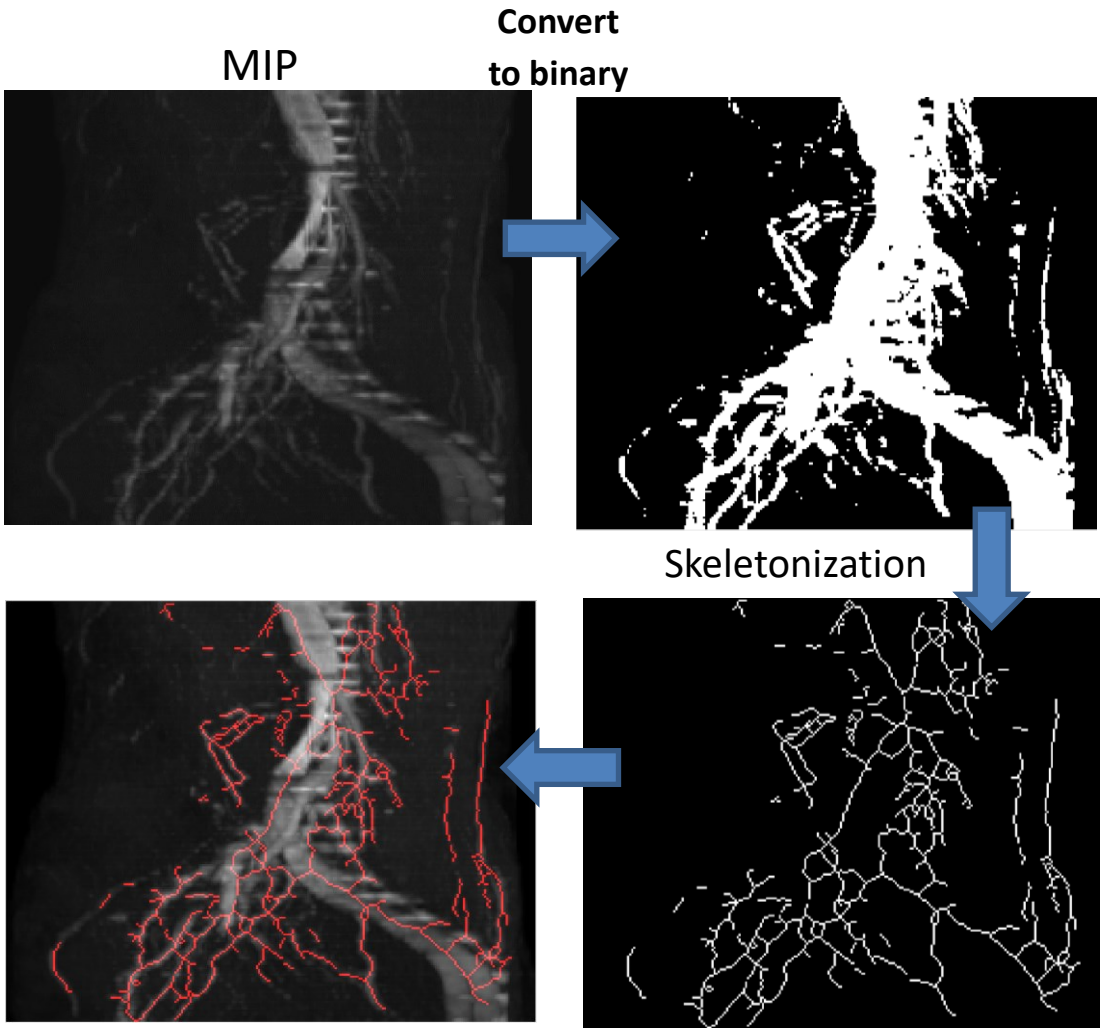

Figure 6.10: Vessels' tracing process in steps using skeletonization.

6.5.2.6 Vessels' Branching Points Detection

Once the binary image has been converted into a skeletonized version, branching points can be detected by using a structuring element that reflects the branching angle and shape. Figure 6.11 shows an example of using one structuring element to detect all branching points on an image by applying the AND operator on all orientations of the structuring element.

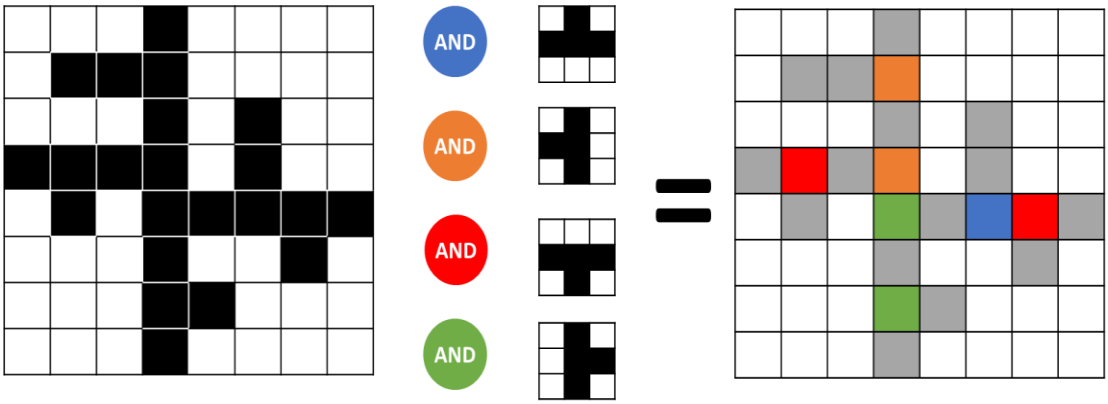

Figure 6.11: Vessels branching points detection process using AND operator on multiple orientations of the same structuring element.

After going through all these steps, the algorithm displays a 360 MIP of the TOF-MRA scan with vessels traced by the algorithm highlighted in red and branching points highlighted in yellow. Figure 6.12 shows the final result produced by the algorithm. The algorithm produces an arborization index - which is the total number of branching points seen on all MIP images of the TOF scan divided by 18 (number of MIPs for each scan). The algorithm also produces a secondary measurement that represents the total vessels length which is the sum of all the pixels in the traced vessels divided by the number of projections (18).

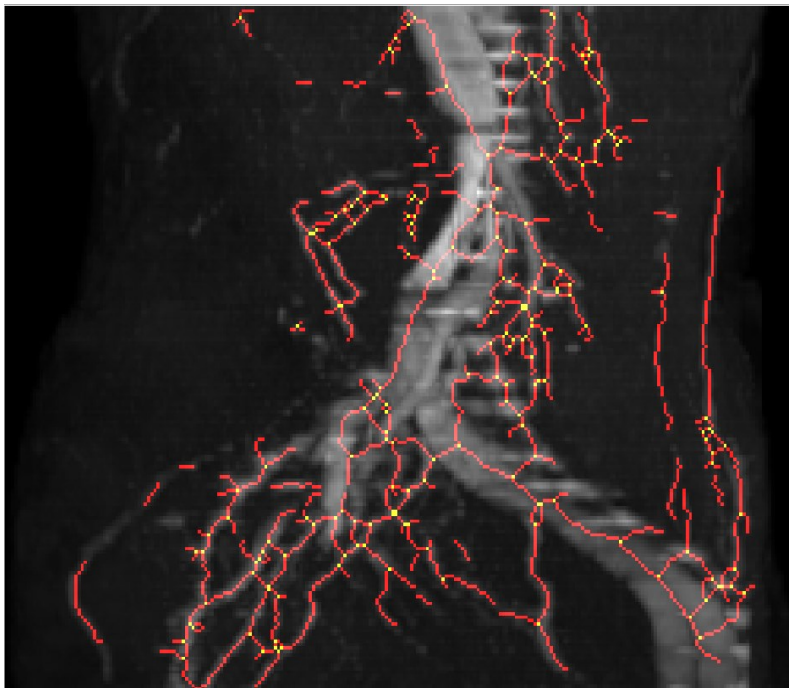

Figure 6.12: TOF MIP with the vessels traced denoted in red and vessels branching denoted in yellow

6.5.3 Study Scanning Parameters

The developed scanning sequence and quantification algorithm were tested out in a human study comparing CD patients with HVs. 2D TOF scans were acquired in the supine position between the top of the hip joint and L2 vertebra on a Philips 3T Ingenia wide bore scanner (Philips, Best, The Netherlands). Table 6.2 shows the full scanning parameters.

Table 6.2: TOF scanning parameters

Parameter	**2D TOF**
Plane	Axial
TR (ms)	9.8
TE (ms)	2.16
Flip angle	60
Turbo factor	1
FOV (mm)	300×240×400
Matrix size	336×336×80
ST	3 mm
Pixel spacing (x,y)(in mm)	1.19×1.19
Compression	SENSE2

TR, Repetition Time; TE, Echo Time; FA, Flip Angle; ST, Slice Thickness.

The study was approved by the University of Nottingham ethics committee (ref: 197-1901) for recruiting HVs and the NHS ethics committee (ref: 19-YH-0337) for recruiting CD patients. All subjects gave informed consent and were required to fast for a minimum of 6 hours prior to the scan. No contrast agents were used for the TOF-MRA scans.

6.5.4 Statistical Analysis

Second TOF scans were acquired for 6 HVs and 8 CD at the end of each scan to evaluate the variability of the quantification method.

To assess the accuracy of the measurement method, biological variations within each group and test-retest repeatability were evaluated using the coefficient of variation (CV):

$$\text{Biological variations CV} = \left[\frac{\text{SD(arborization index of all subjects within each group)}}{\text{mean(arborization index of all subjects within each group)}}\right] \times 100 \qquad (4.2)$$

$$\text{Test} - \text{retest variability CV} = \left[\frac{\text{SD(arborization index of all repeated scans of each volunteer)}}{\text{mean(arborization index of all repeated scans of each volunteer)}}\right] \times 100 \qquad (4.3)$$

Shapiro-Wilk normality test was conducted on both groups to test the null hypothesis that the data has an abnormal distribution.

A planned sub-analysis was implemented across CD patients and HVs matched for BMI to investigate the effect of visceral fat growth on the arborization index. Each patient was matched with a HV with the same BMI (±1 kg/m^2).

Statistical analysis with unpaired, two-tailed t-tests were conducted, and differences were considered significant when the p-value was ≤ 0.05. All absolute values are presented as mean ± SD. Effect sizes were measured in normally distributed data using Cohen's d test with effect sizes of ($d = 0.2$) considered as small, ($d = 0.5$) as medium, and ($d \geq 0.8$) as large based on benchmarks suggested by Cohen (Cohen, 1988).

Linear regression and Pearson's correlation coefficient (PCC) were calculated to evaluate the relations between BMI, abdominal fat ratios (VAT/TAT), abdominal VAT and the arborization index using SPSS software.

6.6 Results

15 patients with active CD and 17 HVs were recruited for this study (Table 6.3 shows the details of the cohort). The HVs were selected to have a widespread of BMIs to investigate the effect of visceral fat growth on vascularity (BMI ranging from 21 to 42 kg/m^2 with an average of 29±7 kg/m^2). CD patients had an average BMI of 25±3 kg/m^2.

Table 6.3: Participant's demographics

	CD	Control
n	15	17
Sex (%)		
Male	7 (54%)	8 (47%)
Female	6 (46%)	9 (53%)
Age (yr)		
Mean	46	28
Range	25-67	22-62
Mean BMI (±SD) (kg/m)	24(±3)	29(±7)
Mean CRP (±SD) (mg/L)	6.6±6.8	-----
FC (±SD) (µg/g)	538±938	___

Figure 6.13 shows the visual difference between a CD patient and a HV on the TOF MIPs. The Figure shows the vessels traced by the algorithm in red and the branching points highlighted in yellow.

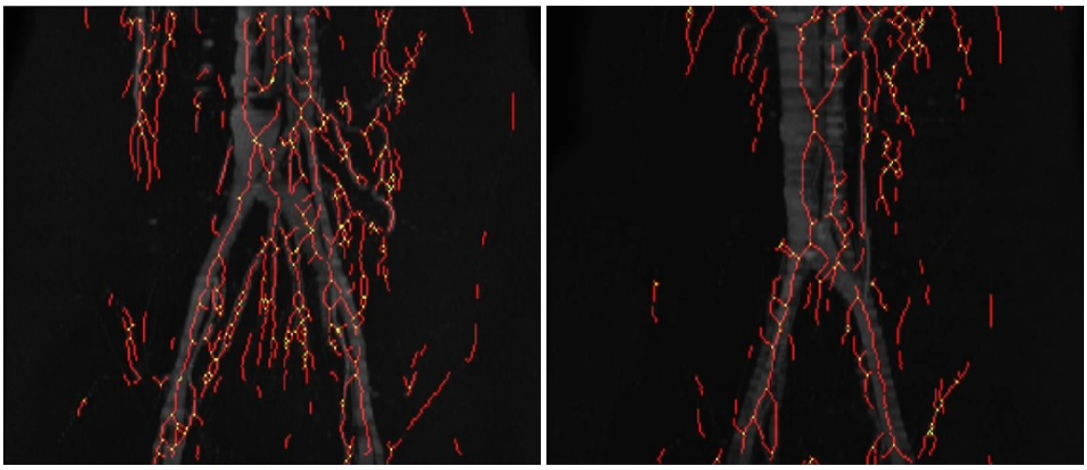

Figure 6.13: TOF MIP of CD patient (left) and a HV (right) with the vessels traced denoted in red and vessels branching denoted in yellow.

Figure 6.14 reveals that CD patients showed a significantly higher vessels arborization in the abdomen when compared with HVs (mean arborization in HVs= 98±34 and CD=137±34; p =0.001, d=1.3). Out of the 16 HVs, 10 with an average BMI of 23±3 kg/m^2 were selected to match 10 CD patients with an average BMI of 23±3 kg/m^2 for further comparison between the two groups. CD patients showed higher arborization values in the sub-analysis compared with a group of 10 HV with matched BMIs (mean arborization in matched HVs= 103±24 compared to 145±36 for CD; p=0.007, d=1.37). Figure 6.15 shows the arborization index of each HV paired with a CD patient with a matching BMI.

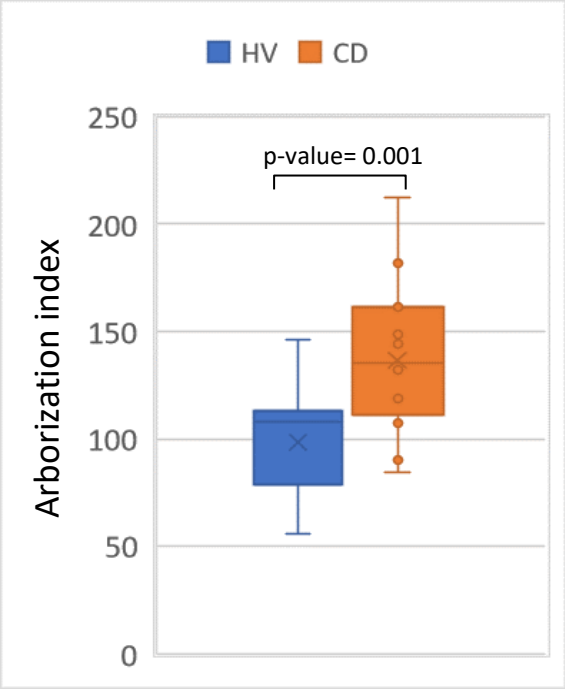

Figure 6.14: Box diagram showing the difference in arborization between HVs and CDs patients.

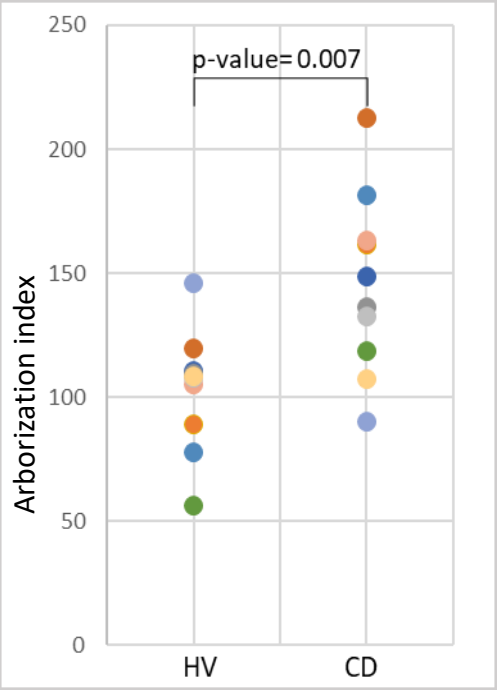

Figure 6.15: A dot plot showing arborization index of 10 HV compared with 10 CD patients with matching BMI.

CD patients also showed a significantly higher vessels length in the abdomen when compared with HV (mean vessels length in HV= 817±143 and CD=990±169; p-value =0.004, d=1.1) (Figure 6.16). CD patients showed higher vessels length values in the sub-analysis compared with a group of 10 HV with matched BMIs (mean vessels length in matched HVs= 836±124 compared to 1032±189 for CD; p=0.015, d=1.23). Figure 6.17 shows the vessels length index of each HV paired with a CD patient with a matching BMI.

The average algorithm processing time is 60 seconds on a machine with 2.6 GHz Intel i7-6700HQ CPU processor and 16.0 GB RAM.

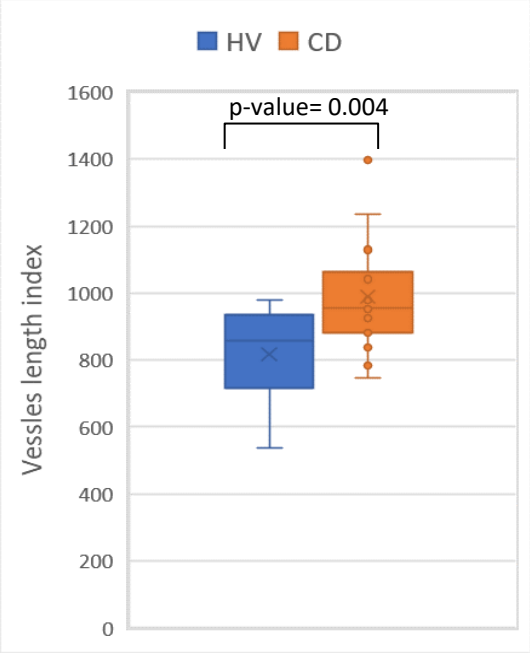

Figure 6.16: Box diagram showing the difference in vessels length between CD and HVs.

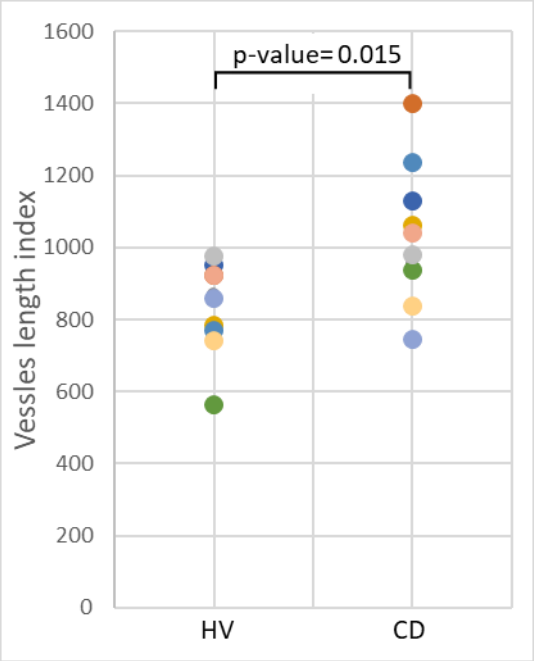

Figure 6.17: A dot plot showing total vessels' length of 10 HV compared with 10 CD patients with matching BMI.

6.6.1 Biomarker Technical Validation

The CVs for biological variations were 25% in the arborization index and 17% in the vessels' length index for both groups. Test and retest variability calculated from a total of 15 repeated TOF scans of the same subjects gave a mean CV of 9±6% for the arborization index and 5±4% for the vessels' length index for both groups combined.

A Shapiro-Wilk test was performed on both measurement methods CD and HV groups and did not show evidence of non-normality (CD; $W = 0.97$, $p = 0.98$) (HV; $W = 0.94$, $p = 0.34$) for the arborization index and (CD; $W = 0.93$, $p= 0.35$) (HV; $W = 0.9$, $p = 0.09$) for the vessels' length index.

Figure 6.18 shows a high correlation between the arborization index and the measured total vessels length with a correlation coefficient of $r= 0.926$; $p<0.001$ for both groups combined.

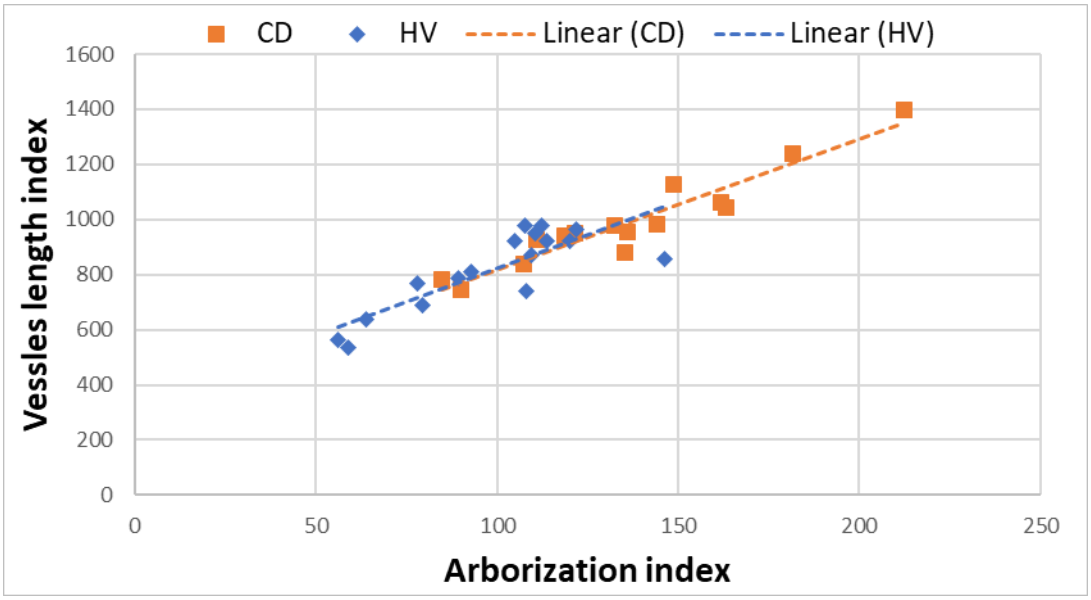

Figure 6.18: plot diagram showing arborization index of CD and HVs plotted against vessels length.

Figure 6.19 shows the arborization index for both groups plotted against BMI. The results show no significant correlation between the arborization index and BMIs (r= -0.2601; p=0.31 for HVs and r=-0.20; p=0.44), which indicates that the arborization index is not significantly affected by BMI for both CD patients and HVs.

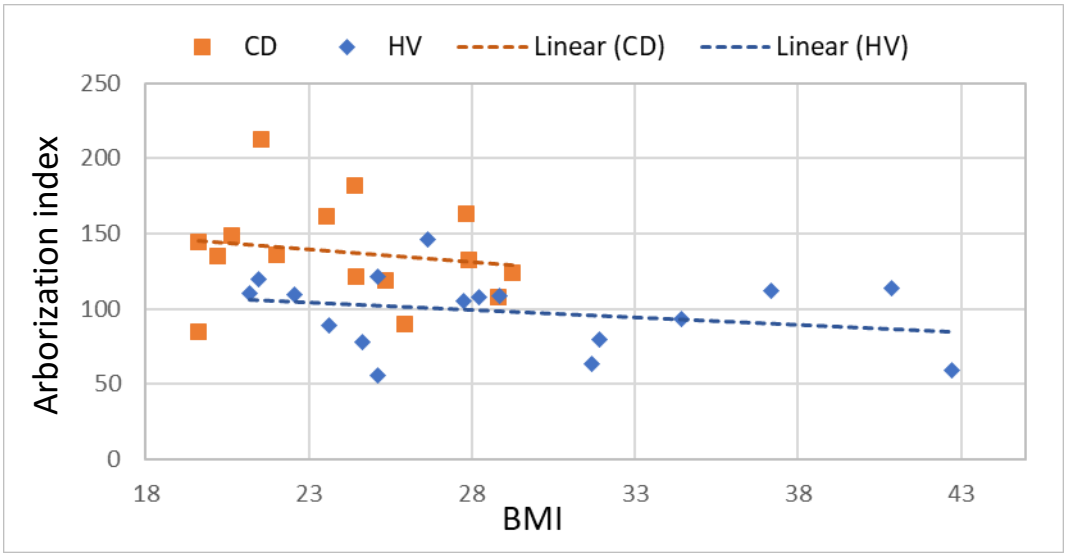

Figure 6.19: plot diagram showing arborization index of CD and HVs plotted against their BMI.

Figure 6.20 shows a diagram of CD and HVs' arborization index plotted against VAT fat volumes in ml calculated from 2-point Dixon scans which produced a Pearson correlation coefficient with an r=0.24; p=0.34 for HVs and r= 0.46; p=0.082 for CD

patients. This shows that the measured arborization index does not increase with higher fat volumes in both HVs and CD patients.

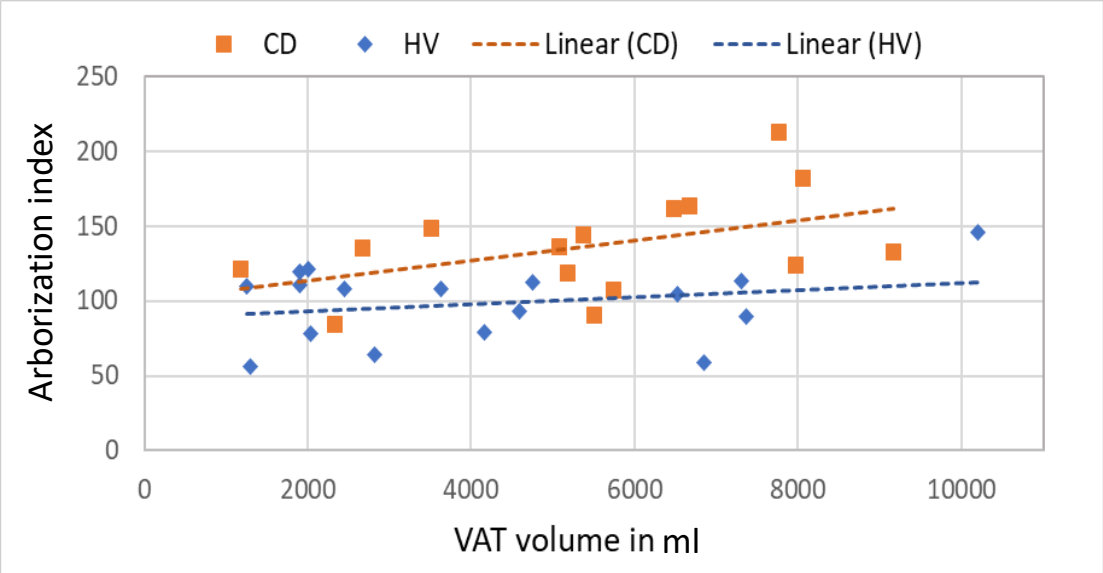

Figure 6.20: Plot diagram showing CD and HVs' arborization index plotted against VAT fat volumes in ml.

Figure 6.21 shows the arborization index of CD and HVs plotted against abdominal fat ratios (VAT/TAT) calculated from 2-point Dixon scans which gave correlation coefficient values of r=0.25, p=0.33 for HVs and r=0.52, p=0.045 for CD. Higher abdominal fat ratios suggest the existence of fat wrapping in CD patients.

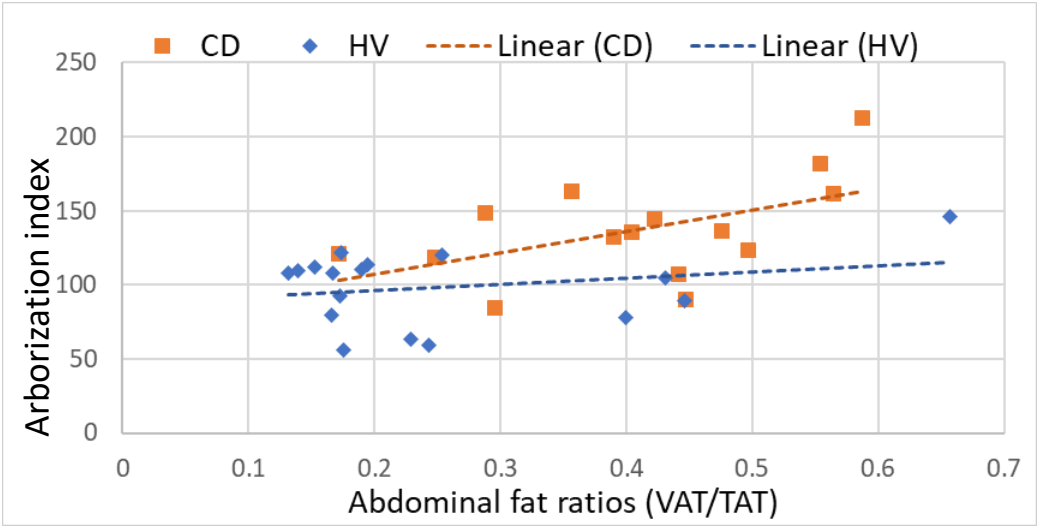

Figure 6.21: Plot diagram showing CD and HVs' arborization index plotted against abdominal fat ratios.

6.7 Discussion

The study showed that the arborization index measured from TOF-MRA scans using the automated quantification algorithm resulted in significant increase in vascularity of the visceral region in CD patients compared to HVs agreeing with prior hypothesis.

CD patients had significantly higher vessel arborization in the abdomen when compared with HVs (as show in Figure 6.14). To validate that the measured arborization index reflects hypervascularity caused by CD opposed to healthy fat tissue growth in the abdomen, we measured the regression of the arborization index with BMI, VAT volumes and abdominal fat ratios (as shown in Figure 6.19, Figure 6.20, and Figure 6.21). No significant correlation was found in between the arborization index and BMI or VAT volumes for both CD patients and HVs, indicating that healthy abdominal fat growth does not influence the measured arborization for this study's sample. Calculating the total length of all the vessels traced on TOF-MRA MIPs also resulted in significant differences between the CD patients and HV ($p = 0.004$, $d = 1.1$).

Sub-analysis of 10 CD patients and 10 HVs showed that the differences in measured arborization and total vessels length between CD and HVs persisted after controlling for BMI (as shown in Figure 6.15 and Figure 6.17).

While measuring vessels lengths is likely more prone to noise, resolution changes, and torso length, comparing the two acquired measurements showed a very high correlation between the arborization index and the total vessels length with $r = 0.926$; $p < 0.001$.

Figure 6.21 shows a high correlation in CD patients between the arborization index and VAT/TAT abdominal fat ratio measurements taken from 2 point-Dixon scans with an r-value of 0.52; $p = 0.045$ for CD patients compared to $r = 0.25$; $p = 0.33$ for HVs. This indicates that the measured hypervascularity correlates with increased VAT/TAT ratio in CD, which could relate to the effect of fat wrapping potentially causing an increased abdominal fat ratio (VAT/TAT).

Mesenteric Blood Flow

While TOF scans reflect the structure of abdominal vessels, they rely on blood flow through these vessels to generate the contrast seen in the images. In the case of increased disease activity and inflammation in a patient, it is suspected that more vessels will appear on these scans as there will be increased blood flow to these sites. On the other hand, in the case of decreased disease activity and inflammation in a patient, although the number of vessels may stay the same, fewer vessels will appear on these scans as there is less blood flow to these sites. This makes TOF an ideal biomarker for evaluating the performance of treatments and disease progression.

The association of mesenteric hypervascularity with CD has been established in the literature however, most research approaches have been done using visual assessment by radiologists on CTE images as a binary biomarker for CD activity where radiologists visually assess the images and confirm or deny the existence of the comb sign (M. Chen et al., 2017) (Colombel et al., 2006). Wu et al. implemented a retrospective quantification of the comb sign by drawing 20 regions of interest (ROIs) with an area of 1 cm^2 on CTE images. They were used to count the number of vessels manually by radiologists in each ROI and averaged across each subject. 72 CD patients and 42 HVs scans were used in this study. The patient group was further divided into active and inactive CD groups using Rutgeerts' score. They found that quantitative comb sign scores were significantly higher in the CD than in the control group and noticeably higher in active CD patients when compared to inactive CD patients. Erythrocyte sedimentation rate (ESR) levels were well correlated with quantitative comb sign scores at arterial and venous stages. This study found that an accurate quantification comb sign predicted CD activity with an accuracy rate of 78.4% at the arterial stage and 80% at the venous stage (Wu et al., 2012).

Vessel branching and length measurements have been used as a metric for vascular features extraction in TOF-MRA, primarily in brain imaging (L. Chen et al., 2018) (L. Chen et al., 2019). Most automated or semi-automated vascular measurements methods attempt to quantify anatomical features of arterial vasculature, such as size, symmetry, branching characteristics, and bifurcation angles (Wright et al., 2013). Y. C. Chen et al. demonstrated that the number of lenticulostriate arteries measured on TOF-MRA

scans could be used as a biomarker for hypertension (Y. C. Chen et al., 2011). However, a direct translation of these methods into imaging the abdomen is not trivial and often requires a specialized sequence development which most likely will generate further complications such as abdominal motion, fat structure complexity and, use of contrast agents. This level of detailed analysis could be achieved in the brain by using 3D TOF-MRA, which requires a long scanning time. This is not feasible for abdominal imaging, which requires the scan to be acquired during a breath hold. As a result, abdominal TOF-MRA has a lower resolution and larger slice thickness than what's traditionally used in the brain.

While MRI can be used to visualise the comb sign using different methods such as post-contrast T1-weighted MRI (Stanley et al., 2016) (Salerno et al., 2019), MRI based CD activity indices such as Clermont, and MaRIA scores do not take quantitative measurements of the comb sign into account when evaluating the severity of the disease. The difficulty of objectively quantifying hypervascularity in MRI caused it to be overlooked when formulating methods for disease activity assessment. TOF-MRA, along with the developed algorithm, offer a simple and reliable method to quantify hypervascularity without the need for contrast agents or any manual effort, which will facilitate the adoption of this measure as a biomarker of disease activity.

The simplicity of the TOF-MRA scanning sequence, which can be applied in many clinical MRI scanners without the need for a contrast agent, makes it an ideal addition to standard MRI scanning sequences used in clinical practice for the assessment of CD activity. The algorithm was designed to be light and easy to use on any computer by researchers or health care specialists without the need for high-performance computers or training data, such as is required for machine learning approaches.

Several filtering and noise correction steps were implemented in the algorithm structure to limit background noise and minimise misregistration of vessels' branching points. However, some misregistration occurs due to motion, water in the bowels, and Stair-Step artifacts. Scans need to be acquired during a 19-second breath hold, which some patients might find harder to manage. If a patient failed to hold their breath during a scan, tissue motion might cause bright areas to appear on the image masking vessels in

that area and in some cases bright vertical lines caused by abdominal motion might be characterized as vessels. The visibility of the vessels on the TOF images depends on the rate of flow through the vessels, which may affect the results. It may be likely that practical abdominal MRI scans will be unable to detect the most distal small vessels.

In interpreting the reported results of the arborization index analysis, it is important to consider potential confounding factors that may have influenced the observed differences between the groups. One notable confound is age, as the CD patients were older than the healthy volunteers (Table 6.3). Age could potentially impact mesenteric vessels morphology and may therefore affect the arborization index measurements. Similarly, other demographic factors such as height and BMI may also have influenced the results.

To ensure that the comparisons made reflect the true mesenteric vessels branching, it would have been beneficial to account for these confounds in the analysis. For instance, a covariate analysis could have been performed, where age, height, and BMI were included as covariates in the statistical model. This would allow for a more accurate assessment of mesenteric vessels arborization, while controlling for potential confounding factors.

Furthermore, other variables such as disease activity, medication, and duration of illness may also have influenced the results. Including these variables in the analysis would help to clarify their contributions to the observed differences in the arborization index.

For this study we did not look to optimise the sequence acquisition at 1.5 T, however lower SNR may not allow the same precision of the algorithm to detect the branching points. These factors have not been fully investigated yet but may prevent the adaption of the method to 1.5 T clinical scanners.

Further validation to standard disease activity measures is needed across larger cohorts to better investigate the utility and reversibility of this biomarker as a non-invasive

measure of disease activity. This is a small pilot study, but a larger group of CD patients is currently being recruited.

6.8 Conclusion

We have produced an automated and objective method of assessing the arborization of vessels in the abdomen using a simple sequence which can be implemented on widely accessible MRI scanners without the need for a contrast agent. We have used this to detect the expected increase in arborization in CD patients.

Our preliminary data suggest that the arborization index can detect hypervascularity which may be a result of intestinal inflammation in IBD. Further validation to standard disease activity measures is needed across larger cohorts to better investigate the utility of this potential biomarker as a non-invasive measure of disease activity and its reversibility to IBD therapies.

References

Babiarz, L. S., Romero, J. M., Murphy, E. K., Brobeck, B., Schaefer, P. W., González, R. G., & Lev, M. H. (2009). Contrast-enhanced MR angiography is not more accurate than unenhanced 2D time-of-flight MR angiography for determining ≤70% internal carotid artery stenosis. *American Journal of Neuroradiology*, *30*(4), 761–768. https://doi.org/10.3174/ajnr.A1464

Biglands, J. D., Radjenovic, A., & Ridgway, J. P. (2012). Cardiovascular magnetic resonance physics for clinicians: Part II. In *Journal of Cardiovascular Magnetic Resonance*. https://doi.org/10.1186/1532-429X-14-66

Chen, L., Mossa-Basha, M., Balu, N., Canton, G., Sun, J., Pimentel, K., Hatsukami, T. S., Hwang, J. N., & Yuan, C. (2018). Development of a quantitative intracranial vascular features extraction tool on 3D MRA using semiautomated open-curve active contour vessel tracing. *Magnetic Resonance in Medicine*, *79*(6), 3229–3238. https://doi.org/10.1002/mrm.26961

Chen, L., Mossa-Basha, M., Sun, J., Hippe, D. S., Balu, N., Yuan, Q., Pimentel, K., Hatsukami, T. S., Hwang, J. N., & Yuan, C. (2019). Quantification of morphometry and intensity features of intracranial arteries from 3D TOF MRA using the intracranial artery feature extraction (iCafe): A reproducibility study. *Magnetic Resonance Imaging*, *57*, 293–302. https://doi.org/10.1016/j.mri.2018.12.007

Chen, M., Remer, E. M., Liu, X., Lopez, R., & Shen, B. (2017). Identification of the distinguishing features of Crohn's disease and ischemic colitis using computed tomographic enterography. *Gastroenterology Report*. https://doi.org/10.1093/gastro/gow037

Chen, Y. C., Li, M. H., Li, Y. H., & Qiao, R. H. (2011). Analysis of Correlation between the Number of Lenticulostriate Arteries and Hypertension Based on High-Resolution MR Angiography Findings. *AJNR: American Journal of Neuroradiology*, *32*(10), 1899. https://doi.org/10.3174/AJNR.A2667

Cohen, J. (1988). Statistical Power Analysis for the Behavioral Sciences. In *Statistical Power Analysis for the Behavioral Sciences*. Routledge. https://doi.org/10.4324/9780203771587

Colombel, J. F., Solem, C. A., Sandborn, W. J., Booya, F., Loftus, E. V., Harmsen, W. S., Zinsmeister, A. R., Bodily, K. D., & Fletcher, J. G. (2006). Quantitative measurement and visual assessment of ileal Crohn's disease activity by computed tomography enterography: correlation with endoscopic severity and C reactive protein. *Gut*, *55*(11), 1561. https://doi.org/10.1136/GUT.2005.084301

Elena Martínez-Pérez, M., Hughes, A. D., Stanton, A. V., Thom, S. A., Bharath, A. A., & Parker, K. H. (1999). Retinal blood vessel segmentation by means of scale-space analysis and region growing. *Lecture Notes in Computer Science (Including Subseries Lecture Notes in Artificial Intelligence and Lecture Notes in*

Bioinformatics), *1679*, 90–97. https://doi.org/10.1007/10704282_10

Fedorov, A., Beichel, R., Kalpathy-Cramer, J., Finet, J., Fillion-Robin, J. C., Pujol, S., Bauer, C., Jennings, D., Fennessy, F., Sonka, M., Buatti, J., Aylward, S., Miller, J. V., Pieper, S., & Kikinis, R. (2012). 3D Slicer as an Image Computing Platform for the Quantitative Imaging Network. *Magnetic Resonance Imaging*, *30*(9), 1323. https://doi.org/10.1016/J.MRI.2012.05.001

Forkert, N. D., Schmidt-Richberg, A., Fiehler, J., Illies, T., Möller, D., Handels, H., & Säring, D. (2011). Fuzzy-based vascular structure enhancement in time-of-flight MRA images for improved segmentation. *Methods of Information in Medicine*, *50*(1), 74–83. https://doi.org/10.3414/ME10-02-0003

Friedman, C. J., & Tegtmeyer, C. J. (1979). Crohn's disease associated with Takayasu's arteritis. *Digestive Diseases and Sciences*, *24*(12), 954–958. https://doi.org/10.1007/BF01311953

Ivancevic, M. K., Geerts, L., Weadock, W. J., & Chenevert, T. L. (2009). Technical Principles of MR Angiography Methods. In *Magnetic Resonance Imaging Clinics of North America* (Vol. 17, Issue 1, pp. 1–11). https://doi.org/10.1016/j.mric.2009.01.012

Kerschnitzki, M., Kollmannsberger, P., Burghammer, M., Duda, G. N., Weinkamer, R., Wagermaier, W., & Fratzl, P. (2013). Architecture of the osteocyte network correlates with bone material quality. *Journal of Bone and Mineral Research*, *28*(8), 1837–1845. https://doi.org/10.1002/jbmr.1927

Lee, T. C., Kashyap, R. L., & Chu, C. N. (1994). Building Skeleton Models via 3-D Medial Surface Axis Thinning Algorithms. In *CVGIP: Graphical Models and Image Processing* (Vol. 56, Issue 6, pp. 462–478). https://doi.org/10.1006/cgip.1994.1042

Madureira, A. J. (2004). The Comb Sign. *Radiology*, *230*(3), 783–784. https://doi.org/10.1148/radiol.2303020645

Meyers, M. A., & McGuire, P. V. (1995). Spiral CT demonstration of hypervascularity in Crohn disease: "vascular jejunization of the ileum" or the "comb sign." *Abdominal Imaging*, *20*(4), 327–332. https://doi.org/10.1007/BF00203365

Nain, D., Yezzi, A., & Turk, G. (2004). Vessel segmentation using a shape driven flow. *Lecture Notes in Computer Science*, *3216*(PART 1), 51–59. https://doi.org/10.1007/978-3-540-30135-6_7

Sakurai, T., Katsuno, T., Saito, K., Yoshihama, S., Nakagawa, T., Koseki, H., Taida, T., Ishigami, H., Okimoto, K. ichiro, Maruoka, D., Matsumura, T., Arai, M., & Yokosuka, O. (2017). Mesenteric findings of CT enterography are well correlated with the endoscopic severity of Crohn's disease. *European Journal of Radiology*, *89*, 242–248. https://doi.org/10.1016/J.EJRAD.2016.10.022

Salerno, S., Terranova, M. C., Vernuccio, F., Picone, D., Tudisca, C., Lo Re, G., &

Lagalla, R. (2019). Imaging assessment of paediatric Crohn's disease: A literature review. *Hong Kong Journal of Radiology*, *22*(1), 4–15. https://doi.org/10.12809/hkjr1916912

Stallard, D. J., Tu, R. K., Gould, M. J., Pozniak, M. A., & Pettersen, J. C. (1994). Minor vascular anatomy of the abdomen and pelvis: a CT atlas. In *Radiographics : a review publication of the Radiological Society of North America, Inc* (Vol. 14, Issue 3, pp. 493–513). Radiographics. https://doi.org/10.1148/radiographics.14.3.8066265

Stanley, E., Moriarty, H. K., & Cronin, C. G. (2016). Advanced multimodality imaging of inflammatory bowel disease in 2015: An update. *World Journal of Radiology*, *8*(6), 571. https://doi.org/10.4329/wjr.v8.i6.571

Tetteh, G., Efremov, V., Forkert, N. D., Schneider, M., Kirschke, J., Weber, B., Zimmer, C., Piraud, M., & Menze, B. H. (2020). DeepVesselNet: Vessel Segmentation, Centerline Prediction, and Bifurcation Detection in 3-D Angiographic Volumes. *Frontiers in Neuroscience*, *14*, 1285. https://doi.org/10.3389/fnins.2020.592352

Wheaton, A. J., & Miyazaki, M. (2012). Non-contrast enhanced MR angiography: Physical principles. *Journal of Magnetic Resonance Imaging*, *36*(2), 286–304. https://doi.org/10.1002/jmri.23641

Wright, S. N., Kochunov, P., Mut, F., Bergamino, M., Brown, K. M., Mazziotta, J. C., Toga, A. W., Cebral, J. R., & Ascoli, G. A. (2013). Digital reconstruction and morphometric analysis of human brain arterial vasculature from magnetic resonance angiography. *NeuroImage*, *82*, 170. https://doi.org/10.1016/J.NEUROIMAGE.2013.05.089

Wu, Y. W., Tao, X. F., Tang, Y. H., Hao, N. X., & Miao, F. (2012). Quantitative measures of comb sign in Crohn's disease: Correlation with disease activity and laboratory indications. *Abdominal Imaging*, *37*(3), 350–358. https://doi.org/10.1007/s00261-011-9808-8

7 Conclusions and Future Work

The main objectives of this thesis have been to develop and evaluate non-invasive MRI-based methods for assessing disease activity in CD. Accurate and reliable methods for monitoring disease activity and assessing treatment response are essential for effective CD management, but traditional techniques, such as endoscopy are invasive, may be uncomfortable and unable to completely assess the small bowel.

The first part of this study investigated the potential use of abdominal fat measurements as a biomarker for fat wrapping, a characteristic feature of CD. Both retrospective and prospective comparative studies showed significant differences in the ratio of VAT to total abdominal fat (VAT/TAT) between CD patients and HVs, suggesting that this ratio could be used as a surrogate measure for fat wrapping in CD. These findings provide support for the inclusion of an accurate and objective assessment of fat wrapping in CD disease activity metrics and suggest that abdominal fat ratios may have potential as a non-invasive biomarker for CD. The development of an automated abdominal fat segmentation algorithm, which was used to measure abdominal fat volumes in this study, represents an important step towards more objective and quantitative assessments of fat wrapping in CD.

The second part of the study developed and validated an automated algorithm for tracing and analysing abdominal vessels on time-of-flight MRA scans to assess mesenteric vascularization in CD patients. The results showed an expected increase in vessel arborization in CD patients, which forms part of the pathophysiological process of intestinal inflammation. These findings suggest that the arborization index could be used as a potential biomarker for non-invasively assessing disease activity and evaluating the response to treatment in CD. The ability to automatically trace and quantify vessel arborization on MRI scans using this algorithm represents a significant advancement in the field, as it allows for more objective and quantitative assessments of mesenteric vascularization in CD patients.

Overall, the results of this study provide promising evidence for the utility of both abdominal fat ratios and vessel arborization as non-invasive measures of disease activity. These methods offer a valuable alternative to traditional invasive techniques, and have the potential to improve the accuracy and reliability of disease activity assessment in CD. However, it is important to note that these methods are still in the early stages of development and further validation across larger cohorts and comparison to standard disease activity metrics is needed to fully evaluate their potential as biomarkers and to understand their relevance to CD management.

In addition, there are several limitations and potential sources of bias that should be considered when interpreting the results of this study. The sample size of the CD patient group in both parts of the study was relatively small, and the results may not be generalizable to other populations. It is also possible that other factors, such as medications, diet, and lifestyle, may have influenced the results and should be taken into account in future studies.

Despite these limitations, the findings of this thesis contribute to the growing body of knowledge on the use of MRI-based methods for non-invasive assessment of disease activity in CD and highlight the potential of these methods as a valuable tool for CD management. Further research is needed to fully understand the clinical utility and relevance of these methods and to optimize their use in clinical practice.

7.1 Future Work

For this study, recruited patients had undergone clinical MRE scans close to the date of their study scan. Expert radiologists are currently evaluating the clinical scans to generate a MaRIA score disease activity index which will be used to further validate the results of this study.

The next step in this research will be to finish gathering data through the recruitment and evaluation of additional patients in order to expand the sample size and data diversity. Currently, a multi-centre study is being set up in which TOF scans are

collected from CD patients as part of their clinical scans. TOF scans may be useful for evaluating the effectiveness of treatments and disease progression in CD by examining the changes in blood flow to abdominal vessels due to changes in inflammation and disease activity. The results of this study could potentially provide insight into the usefulness of TOF scans as a biomarker for monitoring the effectiveness of treatments and disease progression in CD patients. Additionally, a scanning sequence is also being developed to work on clinical MRI scanners from a variety of manufacturers. This is important as most clinical scans are acquired using 1.5 T MRI scanners, and the ability to use the developed scanning sequence on these scanners would make it more widely applicable in clinical practice. By focusing on the development of a scanning sequences that are compatible with a range of clinical scanners, it will be possible to gather a larger and more diverse sample of data, enabling a more robust evaluation of the utility of the arborization index as a non-invasive measure of disease activity in CD and its reactivity to medical and surgical intervention.

Another area of focus for future work will be to investigate the potential applications of the automated segmentation algorithm developed in this study in other contexts, such as monitoring the response to weight loss and evaluating the impact of surgical interventions on abdominal fat. The segmentation algorithm is currently being used in multiple research projects, including studies on the effects of exercise training on liver fat composition and visceral fat volumes in individuals with type 2 diabetes. This demonstrates the potential utility the developed algorithm in a variety of settings and highlights the need for further research to explore their potential applications.

One extension of this research is the use of magnetic resonance spectroscopy (MRS) to examine the biochemical composition of VAT in CD patients. MRS is a non-invasive technique that can be used to measure the concentrations of various metabolites in tissues, including fat. By analyzing the MRS spectra of VAT in CD patients, it may be possible to identify specific biochemical changes that are associated with disease activity or treatment response. This could provide additional insights into the underlying mechanisms of fat wrapping and further evolve our understanding of the physiology behind its formation.

Another extension of this research is the use of multi-echo Dixon techniques which could be explored to study changes in visceral fat. These techniques involve the acquisition of multiple echoes at different echo times, which is used to separate fat and water signals and quantify their relative contributions to the signal intensity. This results in what is known as Proton Density Fat Fraction (PDFF). As fat hypertrophy consists of densely packed adipose cells, fat fraction could potentially reveal the exact location of fat hypertrophy in visceral fat.

Further efforts will also be made to improve the algorithms by incorporating additional imaging sequences and using more advanced image processing techniques in order to enhance their sensitivity, specificity and pave the way for their application in clinical practice.